Preparation and characterization of high entropy alloy nitride thin films

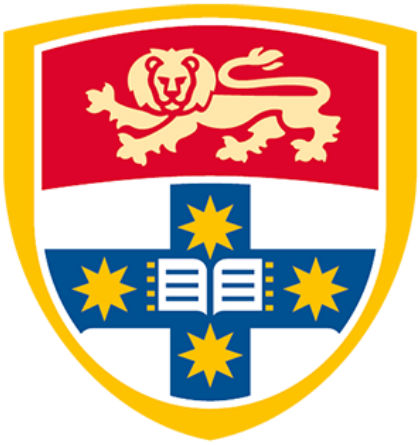

THE UNIVERSITY OF SYDNEY

Fanjun Xu

A thesis submitted to fulfilment of the requirements for the degree of Master of Philosophy

School of Chemical and Biomolecular Engineering

University of Sydney

2024

Table of content

Statement of Originality

I hereby declare that the content presented in this thesis is the result of my own original research and represents my independent work. This thesis has not been submitted, in whole or in part, for the award of any other degree or qualification.
I further affirm that all sources utilised in the preparation of this thesis have been duly acknowledged, and any assistance received during its development has been appropriately recognised.

Printed name: Fanjun Xu

Signature:

Date: 28 December 2023

Abstract

High-entropy alloy (HEA) thin films are new in the field of research for surface engineering, garnering great interest due to their unique properties. HEA is a material group consisting of five or more constituent elements with equal or nearly equal atomic ratios. High-entropy nitride (HEN) thin films represent a novel ceramic thin film pioneered upon the foundation of the HEA concepts, exhibiting a series of outstanding properties, such as exceptional strength, high thermal stability, and excellent electrochemical properties. $AlCrFeCoNiCu_{0.5}$ nitride thin films are one of the surface layer materials of interest, which was reported to be extraordinarily hard. However, limited work has been done to deposit $AlCrFeCoNiCu_{0.5}$ nitride thin films by physical vapour deposition (PVD). In this thesis, $AlCrFeCoNiCu_{0.5}$ nitride thin films were fabricated on Si (100) substrates using a filtered cathodic arc deposition (FCAD). The nitrogen concentration of the HEN thin films was adjusted by changing the nitrogen partial pressure ratio (R_N) from 5% to 100% in the FCAD system during the deposition. The arc discharge in different nitrogen partial pressure conditions was studied, and the variations in deposition rate were analysed based on the discharge energy. SEM-EDS revealed that the nitrogen composition increased from 0.5 ± 0.1 at.% to 18 ± 1.6 at.% for R_N increased from 5% to 100%. XPS confirmed the existence of CrN at the surface and AlN beneath the surface. No AlN signal was observed at low R_N, showing that a portion of nitrogen occupied the interstitial sites without forming nitrides. Moreover, XPS after etching showed that CrN tends to appear only on the surface due to chemical vapour deposition. XRD demonstrated a transition in HEN thin film's crystallinity from a single cubic FCC phase to an amorphous structure with increasing R_N. The XRD peak analysis of the FCC phase demonstrated a crystal lattice expansion and a grain size reduction. AFM revealed a reduction of surface roughness from 0.51 to 0.29 nm at maximum R_N. Based on the nanoindentation results, a 23% enhancement in hardness was achieved, reaching a maximum of 9.6 ± 0.1 GPa at an R_N of 50%. The hardness of HEN thin films is superior to the HEA thin films with similar compositions deposited by FCAD.

Acknowledgement

I would like to express my deepest gratitude to my esteemed supervisors, Professor Zongwen Liu and Professor Marcela Bilek, for their invaluable guidance and support throughout this research project. I extend my sincere appreciation to Dr Kostadinos Tsoutas for his equally dedicated supervision and valuable contributions to this research endeavour.

I would like to acknowledge the significant contributions of Dr Hong Zhao and Mr Tenghao Jiang for their insightful discussions, as well as the proof-reading and suggestions to my writing skills. Additionally, I am grateful to my colleagues, Dr. Ian Falconer, Mr. Julian Whichello, Mr. Joey Liang, for their collaborative efforts and support during this research project.

I would also like to extend my thanks to the staff of the University of Sydney Engineering Faculty, the University of Sydney HDR Group, Sydney Analytical (SA), Sydney Microscopy & Microanalysis (SMM), Research and Prototype Foundry (RPF), and Sydney Manufacturing Hub (SMH) for their support and assistance in providing the necessary resources and facilities for this research.

Furthermore, my heartfelt appreciation goes to my family, Ms Mei Wang and Mr Shuqing Xu and my aunt Ms Jing Wang for their unwavering financial and emotional support.

List of Figures

List of Tables

List of Acronyms

HEA – High Entropy Alloy

HEN – High Entropy Nitride

HEO-High Entrop Oxide

HEC-High Entropy Ceramic

FCAD – Filtered Cathodic Arc Deposition

XRD – X-ray Diffraction

XPS – X-ray Photoelectron Spectroscopy

SEM-Scanning Electron Microscopy

AFM – Atomic Force Microscopy

TEM – Transmission Electronic Microscopy

FCC – Face-centred Cubic

BCC – Body-centred Cubic

RF – Radio Frequency

STEM – Scanning Transmission Electron Microscopy

EDS – Energy Dispersive X-ray Spectroscopy

CVD-Chemical Vapour Deposition

PVD-Physical Vapour Deposition

FWHM-Full Width at Half Maximum

CA-Contact Angle

EDP-Electron diffraction pattern

VEC-Valence Electron Concentration

Chapter1

Introduction

1.1. Research motivation

Alloys were used in manufacturing, mechanical industries, and aeronautical industries for decades. The development of advanced alloys with tuneable properties was of interest in the field of novel material design for their applications in scientific research and real-world scenarios. The traditional concept of alloy manufacturing, based on one or two constituent elements, is reaching its bottleneck in meeting the demand for more complex and challenging engineering applications such as nuclear and aerospace industries. Yeh *et al.* [1]. promoted a new approach to alloy design in 2004, defined as high entropy alloys (HEAs) or multi-component principal element alloys. HEAs expand the field of alloy design by consisting of five or more principal elements with an equiatomic ratio, in which the concentration of each element could vary in a range of 5 to 35 at% [1]. The tuned microstructure and composition of the HEAs allow them to establish improved properties in previous research, including high yield strength [2, 3], exceptional stability and durability [4, 5], and promising electrochemical properties [6, 7]. HEAs have shown great potential in a wide range of applications, such as aerospace and aeronautical components [1], biomedical applications [8], and nuclear industries [9].

The recent studies of HEAs focus on bulk form, which has already promoted alloys with numerous compositions, and many have established superior properties [10]. However, HEAs in the form of thin films are a recently promoted scenario of alloy design that is of great interest to material science. In this phenomenon, HEAs thin films with desirable mechanical, thermal and electrochemical properties, are fabricated on surfaces in dimensions of micrometres or nanometers, which aims to protect surfaces under harsh environments [11]. Various physical or chemical techniques, including laser cladding, magnetron sputtering, and cathodic arc deposition, could be used to deposit the thin films. Therefore, it is worth investigating the variations in thin film composition and microstructure to optimise HEA thin film performance

by controlling the deposition parameters. The HEA thin films under investigation include both HEA-based composite thin films and HEA-based ceramic (HEC) thin films such as high entropy oxides (HEOs) and high entropy nitrides (HENs) [13].

1.2. Problem statement

HEAs have offered great potential in future industrial applications so far, but there is still a lack of investigation in HEA and HEC thin film deposition. For the system of $AlCrFeCoNiCu_{0.5}$, although the synthesis process of bulk HEA has been well-developed, there was a lack of research to fabricate HEA and HEC thin films with desired properties [10]. The deposition process and the effect of deposition parameters, such as arc current, working pressure, partial pressure of reactive gas, etc, are worth studying.

Moreover, exploring the numerous combinations of compositions and microstructures that the HEAs could offer is challenging, as the properties depend on these features [12]. Changing the composition and microstructure of HEAs could offer possible improvements in performance, such as enhanced mechanical properties [13], thermal stability [14], and electrochemical properties [15]. There is still a minor understanding of the HEC thin films compared to HEA thin films [16]. Characterising and analysing the nanoscale features could give an insight into when and how these thin films might promote superior properties. In this thesis, HEN thin films with various nitrogen partial pressures are deposited by FCAD. The surface morphology, composition, surface chemistry, crystal structure and hardness of the deposited thin films are investigated. Therefore, the thesis aims to explore how the deposition conditions, such as nitrogen partial pressure and deposition rates and so on, affect the mechanical properties, surface chemistry and microstructure of $AlCrFeCoNiCu_{0.5}$ nitride thin films.

1.3. Research objectives

In this thesis, HEN films based on the $AlCrFeCoNiCu_{0.5}$ system were chosen to be fabricated due to the benefits that the system has been well investigated in the form of both bulk alloy and alloy thin films, which have already established excellent mechanical properties,

superior thermal properties, and outstanding oxidation resistance [17-19]. In addition, the constituent elements are relatively abundant and low-cost. Filtered cathodic arc deposition (FCAD) is used to fabricate thin films on silicon wafers due to its advantages, such as high deposition rate, convenient control of composition and microstructure, and capability to provide dense and smooth thin films [20]. The nitrogen atoms are incorporated into the thin films by introducing N_2 gas into the system during deposition.

The main objective of this thesis is to study the effects of nitrogen partial pressure during the film deposition on the composition, surface chemistry, and microstructure of $AlCrFeCoNiCu_{0.5}$ nitride thin films. To conduct this research, a bulk form of $AlCrFeCoNiCu_{0.5}$, a high-entropy alloy that has been well-studied, is used as a source for the thin film preparation by FCAD. The specific objective of this thesis includes:

I. Study the influence on the deposition process and film growth through variation of the partial pressure of the nitrogen by introducing a binary gas mixture.
II. Study the effect of incorporating various nitrogen concentrations at different nitrogen partial pressure ratios (R_N) on the evolutions of microstructure and surface chemistry of the $AlCrFeCoNiCu_{0.5}$ nitride thin films.
III. Investigate how the changes in microstructure and chemistry of HEN thin films with various nitrogen concentrations could impact the thin film's properties.

Literature Review

1.4.High entropy alloy (HEA)

Metals and alloys have been used by human civilization as materials for different tools since ancient times. The use of alloys in developing more capable heat engines, aerospace equipment, and biomedical materials is essential. Alloys with higher strength, higher wear resistance, optimum heat resistance, and electrochemical properties are of interest. The traditional alloy design is based on a 'base element" approach, by choosing one or two principal elements to meet specific property requirements and one miner element or a few alloying components to enhance the alloy performance [21]. This traditional principle is approaching a bottleneck in that most possible recipes have been investigated, and the optimized properties have been obtained. To further improve the alloying material, one of the major approaches is increasing the number of principal elements.

High entropy alloys (HEAs) represent a relatively new concept proposed by Yeh *et al.* 14 years ago [1]. HEA, also referred to as multicomponent alloys and concentrated solid solutions, usually contain more than five principal elements in an equimolar ratio. The concentration of each element is generally in a range of 5 - 35%, but this is not always the case. They could be considered as "dissolved" in an ideal solution in which solvent and solute are both metals. Atoms of each element are randomly distributed in the lattice, forming a fully disordered solid solution phase, as illustrated in *Figure 1*. Therefore, the configurational entropy of mixing of the system is enhanced, potentially providing more stable and durable materials than the conventional binary and ternary alloys.

The HEAs generally form solid solutions with the crystalline structure of body-centred cubic (BCC) and/or face-centred cubic (FCC) phases [21]. It was reported that FCC-type HEAs usually establish high plasticity but lower strength [22]. In comparison, the BCC-type solid solutions were reported to have superior strength and reduced plastic deformation at room temperature. To achieve desirable HEA performance, BCC structure is one of the dominant factors to be introduced for higher hardness and toughness [23]. Intermetallic phases might also form for a lower level of disorder at a lower temperature, as the high entropy effect might

not be sufficient to overcome the enthalpy barrier of the Gibbs free energy. Intermetallic phases would cause instability and deformation in uses, weakening the applicability of the material, which has to be limited in alloy design.

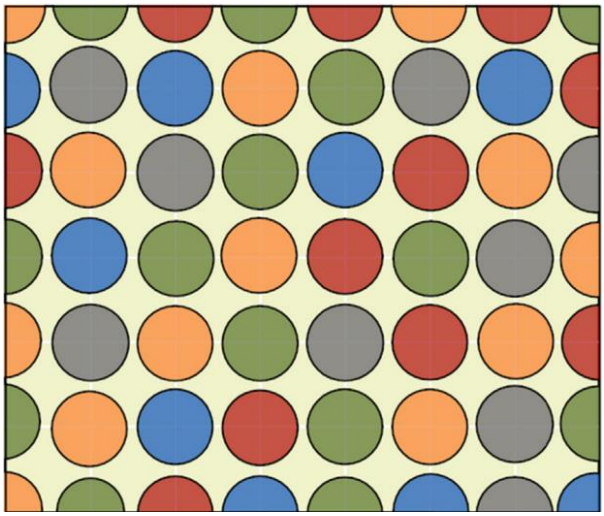

Figure 1 Atoms are randomly mixed in the lattice of a multicomponent alloy, each element presented by different colours. Equal atomic size and loose packing are assumed [21].

The major potential of HEAs is the enormous combinations of alloy recipes, most of which are rarely investigated. *Figure 2* represents the relationship between the number of equatomic compositions and the number of principle elements in multicomponent alloys. The insert reveals the location of HEAs in a ternary phase diagram. Researchers usually focus on the edges of a phase diagram for conventional alloy design, and the base element would be dominated. The HEAs should be at least a quinary system. It only included a small percentage of the design space. By introducing the concept of HEA, the investigated region starts to shift to the centre of the diagram. From the 'base element' principle, only N alloys could be obtained by N base elements. However, for any combination of elements to form an equiatomic alloy selected from the total of n elements, the total possible alloys N increase from n to $n = 2^n - n - 1$. It doesn't make much difference for $N < 3$, but the number N would grow exponentially and go beyond 100 when $n \geq 6$. Since there are 118 elements in the periodic table classified as metal, it would be a great challenge to study HEAs both theoretically and experimentally, to find out the recipes that present valuable properties for real-world applications.

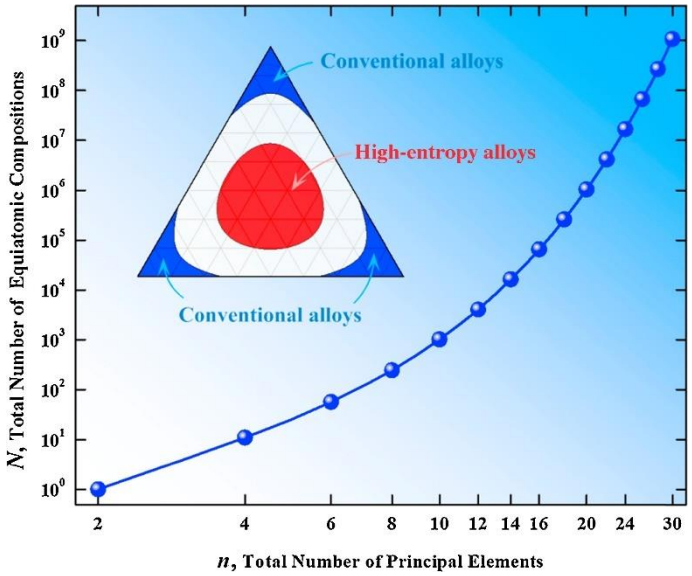

Figure 2 Schematic diagram of the variation in the total equiatomic compositions with the total number of principle elements. The insert shows the location of conventional alloys and high-entropy alloys in a ternary diagram [21].

Based on current research, HEAs and their ceramics have presented some desirable properties. They showed superior mechanical properties, excellent thermal and chemical stability, and outstanding corrosion resistance [24]. For example, HEAs consisting of FCC phases have comparable yield strength and similar microstructures to those Ni-based superalloys. An increase in yield stress with increasing temperature has also been observed [25]. It is reported that at 1100 ℃, refractory HEA VNbMoTaW is able to maintain a yield strength of 400 MPa, which is superior to the conventional Inconel 718 Bi-based alloy, which the yield strength reduces to 200 MPa at 1000 ℃. Another reason to study HEAs is that they might be able to simultaneously obtain reasonable strength and good ductility [1]. The traditional materials could only choose to optimize one of those properties. Meanwhile, the current trend of high entropy material has allowed the development of an ultimate material with high performance in both fields [25, 26]. *Figure 3* shows the current trend of HEAs in obtaining mechanical properties. It shows that the groups of conventional alloys reveal relatively smaller yield strength than the metallic glasses, while the metallic glasses obtain less ductility than the conventional alloys. The HEAs tend to sit close to the middle of the diagram, which balances the two distinct properties.

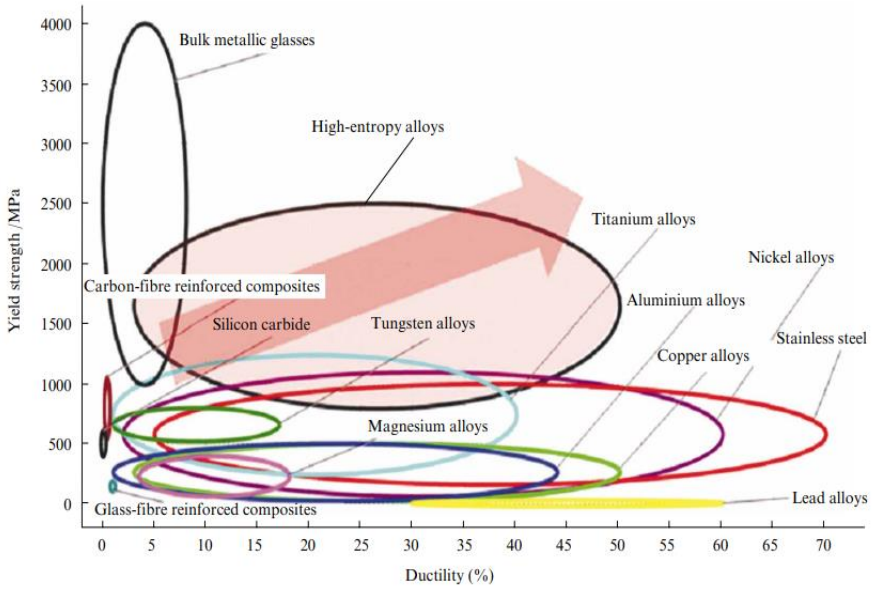

Figure 3 Current trend of high-entropy alloys in a Yield-strength VS Ductility diagram compared with other materials [21].

1.5.Four core effects of HEAs

1.5.1. High entropy effect

High entropy alloy tends to obey the Gibbes phase rule (P = C + 1 - F, where P is the number of phases, C is the number of elements, and F is the maximum degrees of freedom) that predicts the phases of a given alloy in an equilibrium state [12]. For example, it is expected that a maximum of 7 equilibrium phases could form in the case of a 6-element system [1]. However, a single-phase solid solution is observed for an HEA system instead of intermetallic phases, with the components chosen that satisfy the HEA-formation critical. The main concept of HEAs formation is the increased configurational entropy (S_{config}) of a single-phase crystal structure.

The S_{config} could be enhanced by raising the number of elements in the system, as well as having each element randomly distributed in the lattice with equiatomic fractions. For example, for a schematic ternary alloy system, the entropy of mixing at the centre of the contour plot will reach a maximum of 9.15 J/molK [1]. In most cases, the total energy gain will be sufficient to stabilise the single-phase solid solution. The entropy of mixing is highly related to the Gibbs free energy of mixing, which is a factor that contributes to the stability of a crystal structure.

Gibbs free energy amounts to the maximum amount of work that could be performed by a thermodynamically closed system, which in this case is the ability of the crystal to transform from one phase to another. The free energy of mixing is also dependent on the entropy of mixing and melting point, expressed as follows:

$$\Delta G = \Delta H - T_m \Delta S_{mix} \quad (1)$$

Where ΔG is the change in Gibbs free energy; ΔH is the change in enthalpy; T_m is the melting point; ΔS_{mix} is the entropy of mixing. The entropy of mixing per mole for an equiatomic HEA is expressed as follows:

$$\Delta S_{mix} = Rln(n) \quad (2)$$

Where R is a global constant; n is the number of elements.

As the number of principal elements increases in a multi-component alloy, the Gibbs free energy reduces dramatically due to the logarithmic relationship, which allows the $T_m \Delta S_{mix}$ term to overcome ΔH. For example, $1.61R$ is the maximum entropy that could be obtained theoretically in a five-element equiatomic system. Any system with a $\Delta Smix \geq 1.5R$ was usually considered "high entropy". Based on the equations, it can be predicted that elevated temperature will favour single-phase alloy formation. The alloys formed at a relatively lower temperature might favour an intermetallic phase instead of a single-phase solid solution. HEA system might shift to metastable phases like intermetallic compounds at room temperature. These criteria do not guarantee the formation of a single-phase solid solution. Several other factors, such as the atomic size difference (δ), valence electron concentration (VEC) and the enthalpy of mixing (ΔH_m), would have a substantial impact. δ accounts for both the component composition and the radii difference of atoms. The VEC indicates the crystalline structure and ΔH_m determines the minimum energy gain for the solid solution to be thermodynamically stable [21]. There is a stabilization factor Ω usually used to predict the solid solution, which gives the ratio between $T_m \Delta S_{mix}$ and ΔH. Overall, the higher entropy of mixing does expand the solubility limit of the solid solution [21].

1.5.2. Severe distortion

The severe distortion effect of HEAs is based on the comparison with the crystalline

structure of the conventional alloys with one or two based elements [27]. Since each element in HEAs has a relatively close molar ratio, they have a roughly equal chance to occupy the lattice sites. Due to the mixture of atoms of different sizes in a concentrated solid solution, the formation atoms in HEAs are displaced away from the ideal lattice sites so that the crystal lattice can be distorted on an atomic scale. Another result is elastic residual stress passed from one atom to another. The distortion effect will enhance the energy barrier between atoms, preventing the dislocation movement. Therefore, it partially explains the strengthening effect obtained by the current research on HEAs, especially BCC-structured solid solutions. The effect also explains how the atomic size difference is able to affect the formation of solid solution and crystal structure, which is proportional to the lattice strain and the hardness [27]. It indicates that ideally, the atomic size difference between constituent elements should be identical in HEA design. Due to the oversized lattice distortion, significant size differences could lead to the formation of an amorphous structure or metallic glass as a metastable phase.

The severe distortion in HEAs has been confirmed by applying X-ray diffraction (XRD) from Yeh *et al* [1]. They studied the reduction of XRD peak intensity of a series of alloys from binary to multicomponent alloys by systematically adding elements [24]. The aim is to conform the effect of lattice distortion to the Braggs diffraction and compare it with the thermal effect. The result has shown that with the addition of the constituent elements, the intensity of the peak refers to the crystal lattice, has further decreased beyond the reduction of the thermal effect. *Figure 4* compares a perfect crystal lattice and a lattice with severe distortion, and their impact on the x-ray diffraction. The work has indicated the presence of the distorted lattice in the solid solution, where difference-size atoms are expected to be randomly distributed in the lattice according to the equal probability of occupancy.

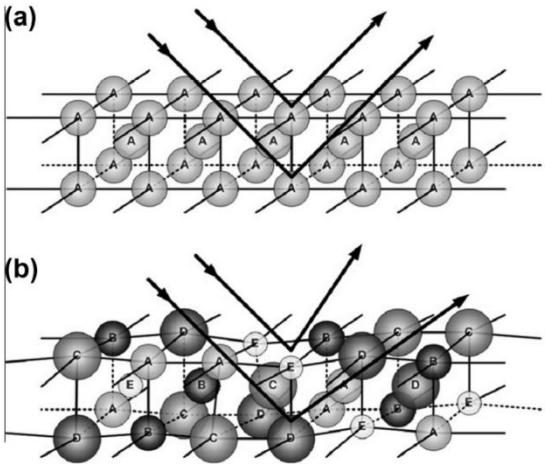

Figure 4 Schematic representation of (a) a perfect crystal lattice, and (b) a crystal with severe lattice distortion [24].

1.5.3. Sluggish diffusion

The atomic diffusion of HEAs is usually slower than in conventional alloys, due to the large diffusion barrier caused by mixing different atomic sizes and the fluctuation of bonds between atoms to atoms [28]. The atoms in a high entropy system tend to occupy positions according to the minimum free energy. Therefore, the electro-potential energy varies from one lattice to another, resulting in a higher energy barrier for diffusion. This feature contributes to the superior properties of HEAs in thermal stability and corrosion resistance. Several studies have shown that the diffusion coefficient of atoms could be impacted by the randomly distributed crystalline structure created by HEA at a higher temperature. For example, Dabrowa *et al.* studied the interdiffusion in a group of AlCoCrFeNi alloys with an FCC structure in the temperature range of 1273-1373 K [28]. The experiment has shown that the crystallographic structure has more significantly impacted the atom diffusion than the chemistry condition created by the nearby atoms. The sluggish diffusion also favours the single-phase solid solution, as it creates an energy barrier for atoms to displace from their lattice sites, avoiding the formation of metastable intermetallic phases with a higher degree of order. The sluggish diffusion also explains the appearance of nanoprecipitation in the solid solution [26].

1.5.4. Cocktail effect

The cocktail effect describes the fact that HEAs are able to obtain unexpected properties

and variations in phases that any individual metal could not provide. It indicates that the property could be improved by adjusting the amount of each constituent element, like increasing the composition of one particular element. For example, the hardness of the alloy could be dramatically enhanced by adjusting the Al composition in the CuCoNiCrALFe HEA, as demonstrated by Zhang *et al.* [24]. The increase in Al composition would favour the phase transformation of crystalline structure from FCC to BCC. Due to the lattice distortion effect mentioned before, the BCC structure further prevents the dislocation of atoms, increasing the hardness and plastic deformation resistance, as shown in Figure 5.

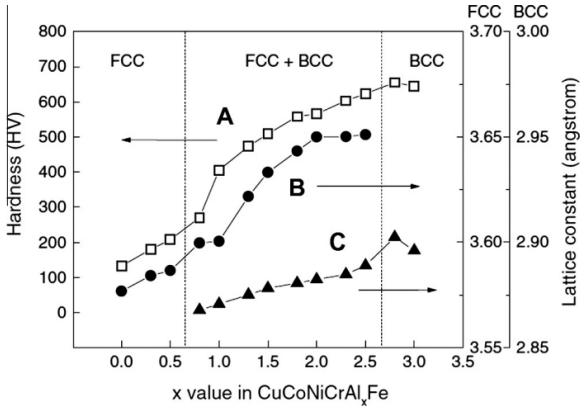

Figure 5 Schematic diagram of hardness and lattice parameters of FCC and BCC phases for different Al composition in a series of CuCoNiCrALFe alloy, A represents hardness, B represents lattice parameter for the FCC phase, C represents lattice parameter for the BCC phase [24].

1.5.5. HEA thin films

The current research and application of HEAs are usually bulk alloys prepared by traditional methods like casting and arc melting. However, several problems are stopping bulk HEAs from being widely used. Elements in the HEAs are rare on earth and hence expensive, so the cost of bulk HEAs could be much higher than the conventionally used alloys, and the size of the bulk alloy prepared by arc melting is limited [21]. In addition, it is difficult to obtain both uniform and dense bulk HEAs with a perfect single-phase solid solution structure using traditional techniques. Metastable phases like intermetallic phases could form during arc melting, reducing the material's mechanical performance, thermal resistance, and corrosion resistance [12].

Therefore, investigations of HEA thin films have recently been garnering attention. The alloy thin films have a broad conventional application, such as a protective shell for aerospace and aeronautical vehicles, depositing thin films on the components' surface to increase surface strength and minimise thermal corrosion. The thickness of the HEA films usually ranges from nanometres to micrometres, depending on the deposition method and requirement [27]. The object whose surface is to be coated by the thin films is generally referred to as the substrate.

One of the major advantages of thin film over bulk alloy is the “rapid quenching” effect, which occurs during the preparation stage [29]. Due to the small thickness, HEA thin films cool rapidly compared with the bulk alloy, which is beneficial to the phase transformation of HEA. The rapid quenching effect also favours the thin film's atomic mobility and residual stress release. Therefore, the HEA thin films are worth investigating due to their potentially optimized properties and lower cost.

HEA thin films with an AlCoCrFeNi system have recently been studied by adding elements such as Cu, Ti, Mn, Mo, and W to alter the microstructure and promote better properties based on the lattice distortion and the cocktail effect. Simple FCC or BCC structure, or dual-phase structure have been established depending on the constituent elements, and properties like hardness and thermal stability were superior to their bulk counterpart. Table 1 lists some HEA thin films and their physical properties in the current literature.

Table 1 HEA thin films deposited by various techniques and their physical properties in the literature.

Composition	Deposition techniques	Crystal structure	Physical properties	Reference
$Al_xCrFeCoNiCu$	Magnetron sputtering	FCC + BCC	Maximum hardness of 11.2 GPa	[30]
AlCrFeCoNiCu	Magnetron sputtering	FCC + BCC	Good thermal stability until 510 ℃	[31]
FeCoNiAlMnW	Magnetron sputtering	Single BCC	Maximum hardness of 8.08 GPa	[32]
AlCrMoSiTi	Magnetron sputtering	Single FCC	Maximum hardness of 11.5 GPa	[33]
$AlCrFeCoNiCu_{0.5}$	Magnetron sputtering	FCC + BCC	Maximum hardness of 13 GPa	[34]
FeNiCoAlCu	Laser cladding	FCC + BCC	Good thermal stability and wear resistance below 780 ℃	[35]
$FeCoNiCrAl_2Si$	Laser cladding	Single BCC	Maximum hardness of 8.83 GPa	[36]
$Al_xCoCrFeNiSi$ (x = 0.1 and 0.3)	Laser cladding	Single BCC	Maximum hardness of 6.97 GPa	[37]
$AlCrFeCoNiCu_{0.5}$	Cathodic arc deposition	FCC + BCC	Maximum hardness of 6.8 GPa	[19]
$AlCoCrCu_{0.5}FeNi$	Cathodic arc deposition	Single FCC	Maximum hardness of 8.4 GPa via 700 ℃ annealing	[38]

1.6.High entropy nitrides (HEN)

1.6.1. Fundamentals of HEN

HENs, or multicomponent nitrides, are ceramic materials developed by adding nitrogen into HEAs. Unlike the metallic HEA, the nitrides have a mix of metallic, covalent, and ionic bondings. They have also shown interesting properties, such as high hardness, excellent

electrical and outstanding thermal resistance [39]. The ability of a transitional metal to form a stable nitride compound changes along the periodic table. The bonding strength of nitrogen with a transition metal, and thus the ability of a transitional metal to form a stable nitride, decreases from the left to the right of the periodic table. *Figure 6* shows the capability of transition metals to form thermodynamically stable multicomponent nitrides with simple crystal structures. It shows that the elements in groups 3–5 form strong ionic bonding with nitrogen, while groups 6–11 show relatively weaker bonding. Since the multicomponent nitrides usually contain elements varying across the table, the difference in nitride forming capacity could cause numerous combinations of microstructures, leading to different properties that may apply to different applications [40].

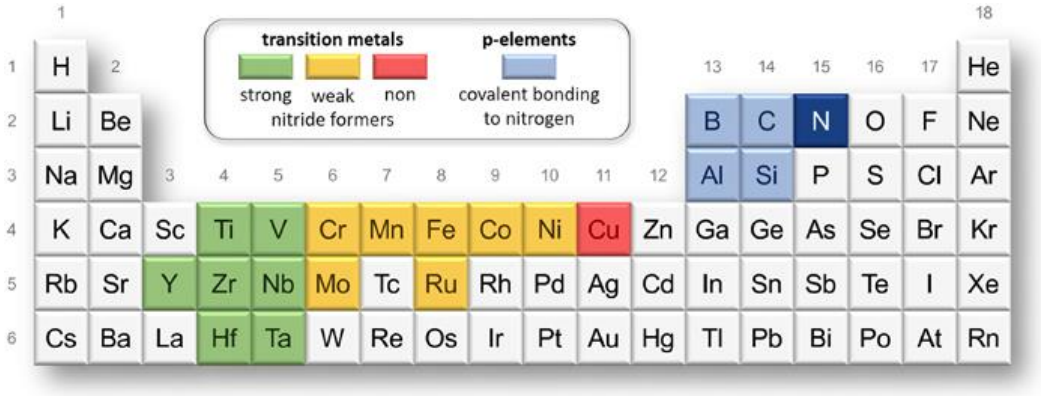

Figure 6 A periodic table shows the elements generally used to synthesise HENs with simple crystal structures and their nitride-forming characteristics [16].

High-stable transition metal nitrides, typically so-called interstitial components, could form during the synthesis of HENs, in which the nitrides occupy voids in the close-packing structure of the metal [16]. There is a variation in the bonding and phase structure of these compounds compared to the metals, so they are distinctly different to the solid solution of non-metals such as N or C in the metallic phases. The solubility of nitrogen in the HEAs is relatively low in the metallic phases, but in the form of components, about half of the atoms are nitrogen. Interstitial nitrides typically form a NaCl-type (B1) structure, with an octahedral orientation surrounding both elements. These compounds promote a mixture of covalent, metallic and ionic bondings with the metals, enabling them to achieve properties such as high hardness, good electrical and thermal conductivity, and outstanding corrosion resistance, a typical sample is TiN. It is worth noting that the NaCl-structure nitrides with group 3 elements are semi-conductors compared to those formed with group 4 or 5 [41].

The standard enthapy of formation of the NaCl-type nitrides increases as the strength of nitride bonding with transition metals decreases among the periodic table. The increase in valence electron concentration of elements in higher groups fills the anti or non-bonding electronic states, resulting in other more complex structures and alternative stoichiometries [42]. For instance, FeN (ΔH_f = -47 kJ/mol) is significantly less stable than CrN (ΔH_f = -117.15 kJ/mol) or TiN (ΔH_f = -338 kJ/mol) [43]. Therefore, various metastable Fe_xN_x compounds with different structure and stoichiometries could co-exist, such as Fe_4N (ΔH_f = -10.46 kJ/mol) [43]. In addition, the enthalpy of formation of nitrides becomes positive for the metals sitting further to the right of the periodic table, such as Cu_3N (ΔH_f = 71 kJ/mol), which are usually metastable.

Moreover, the Al and Si, together with other p-elements from 13–15 groups, form covalent bonds with nitrogen, as indicated by the blue section in *Figure 6*. They could form very stable nitrides with hexagonal (B4) or Si_3N_4 structures, such as AlN (ΔH_f = -318 kJ/mol) and Si_3N_4 (ΔH_f = -743 kJ/mol) [44]. The nitrogen atoms surround the metal by a tetragonal orientation in both structures. However, Al and Si do not establish extra solubility in the transition metal nitrides due to the difference in bonding and structure. Adding Si to transition metal nitrides such as TiN would result in a dual-phase structure of nanocrystalline TiN and an amorphous silicon nitride tissue phase [45]. In addition, metastable solid solution phases such as cubic $(Ti_{1-X}A_X)N$ can be formed when working with kinetically constrained techniques such as physical vapour deposition [46].

Based on the current information, it can be predicted that the HENs constructed by the transition metals would form solid solutions with NaCl-type structures. HENs constructed by the intermediate or later transition metals would form more complex metastable nitrides or remain in the metallic phase due to weaker bondings. For vapour deposition methods to produce thin films, the limited adatom mobility during film growth will not favour the formation of such a complex system. Therefore, it is expected that vapour deposition of thin films composited of later-stage transition metals in a nitrogen environment is more likely to form an amorphous phase [47]. However, there is still a lack of insight into microstructure formation and increment of configurational entropy due to the different combinations of strong, weak, and non-nitride-forming metals in the multicomponent nitride aspect.

1.6.2. HEN thin films

Transitional metal nitride thin films, including both binary and ternary nitrides, have been widely used as a protective coating for cutting, milling, and drilling tools, which require high performance in their mechanical properties. For example, transition metal nitride coatings, such as TiAlN and CrAlNd, have higher hardness than the binary nitrides usually used for protective applications [16]. Aluminium is typically substituted to form a single-phase cubic sodium chloride structure. For a similar reason, multicomponent nitride thin films are worth investigating to determine how the high entropy effect could improve the microstructure and the mechanical properties for future applications.

To fabricate HEN thin films, it is important to combine both strong nitride-forming elements such as Al, Cr, Si and Ti and non-nitride-forming elements like Fe, Co, Ni and Cu to study how these affect structural stability and to explore properties suitable for real-world applications. Most HEN coatings were recently fabricated by reactive magnetron sputtering or vacuum arc deposition by introducing pure nitrogen gas or a binary gas mixture of nitrogen and argon during the deposition. Table 2 lists some of the HEN thin films reported in the literature that contain nitride-forming species like Al and Cr. It could be seen that the HEN thin films tend to promote either a single NaCl-type FCC orientation with binary nitrides, or an amorphous phase due to the severe lattice distortion. Most of them have demonstrated hardness greater than that of the corresponding metallic HEAs due to solid solution strengthening, grain boundary strengthening and nitride precipitation strengthening. A lack of fundamental understanding exists to enable successful material design, and experimental work can only represent a small part of possible compositional space.

Table 2 Microstructure and mechanical properties of HEN thin films reported in the literature.

Composition	Deposition technique	Crystal structure	Maximum hardness (GPa)	Reference
$(FeCoNiCrCuAl_{0.5})N$	Magnetron Sputtering	Amorphous	10.4	[48]
(AlCrMnMoNiZr)N	Magnetron Sputtering	FCC	18.0	[49]
(AlCrMnMoNiZr)N	Magnetron Sputtering	FCC	11.9	[50]
(FeCoNiCuVZrAl)N	Magnetron Sputtering	Amorphous	12.0	[51]
$(AlCrMoSiTi)N_x$	Cathodic Arc Deposition	Amorphous	19.8	[52]
$(AlCrMoTiV)N_x$	Cathodic Arc Deposition	Amorphous	34.1	[53]
$(FeCoCrNiAl_{0.1})N$	Cathodic Arc Deposition	FCC	32.9	[54]
(TiZrNbAlYCr)N	Cathodic Arc Deposition	BCC + FCC	47.0	[55]

1.7.HEA fabrication

1.7.1. Synthesis of Bulk HEAs

Most bulk HEAs in the report are prepared by melting and casting processes, including two types, induction melting and vacuum arc melting, which are liquid-state methods. Arc melting is more commonly used than induction in this case because it is more efficient in melting constituent metals with a temperature above 3000 ℃ [56], which is above the melting point of most conventional metals. *Figure 7* shows the schematic diagram of the vacuum arc melting process, in which the melting temperature is adjusted by changing the current supplied to the electrodes. This process is more feasible for synthesizing HEAs containing elements with high melting points, such as Ti. However, the negative side is that the process could cause evaporation for metals with lower melting temperatures, such as Mg and Al. Induction heating or resistance heating is usually used instead to produce HEAs consisting of these metals. They would be able to achieve better control of the HEA composition. After melting, The HEAs are cast into shapes for various applications such as robs and cathodes. For example, the HEA bulk targets of $AlCrFeCoNiCu_{0.5}$ used in this project are made using arc melting and casting.

Composition is controlled by adjusting one element at a time. The alloy obtains a single solid solution with FCC and BCC orientation. Co, Cu, and Ni tend to favour the FCC phase formation, while Al and Cr are BCC-favouring elements. The addition of the BCC phase was reported to enhance the solid solution strengthening and improve the mechanical performance of $AlCrFeCoNiCu_{0.5}$ alloy [57].

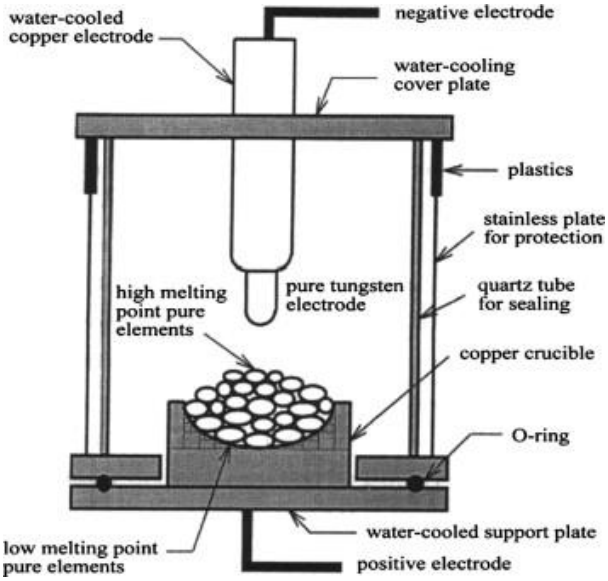

Figure 7 Schematic representation of the vacuum arc melting [24].

1.7.2. Synthesis of HEA thin films

1.7.2.1.Laser cladding

Laser cladding is a surface coating technology that combines a material feeding process and a laser beam. It is used to fabricate film thicknesses of 1 to 5 μm, larger than magnetron sputtering and cathodic arc deposition. [58]. The thickness it obtains is larger than magnetron sputtering and cathodic arc deposition. *Figure 7* shows a schematic representation of the laser cladding process. The deposited material in powder form is first introduced into the cladding heads carried by Argon gas, then sprayed by the nozzle on the substrate. A high-energy laser beam is applied to the surface to melt the powder instantly to form a liquid metal layer. The material is then solidified to form homogenous coatings with good adhesion to the substrate as the laser beam moves across the surface. The composition of the thin films could be precisely controlled by adjusting the powder recipe. The disadvantages of this method include the difficulty of avoiding defects on the surface as it is not always flat and the possible

incorporation of substrate material into the coating for substrates with a low melting point [59].

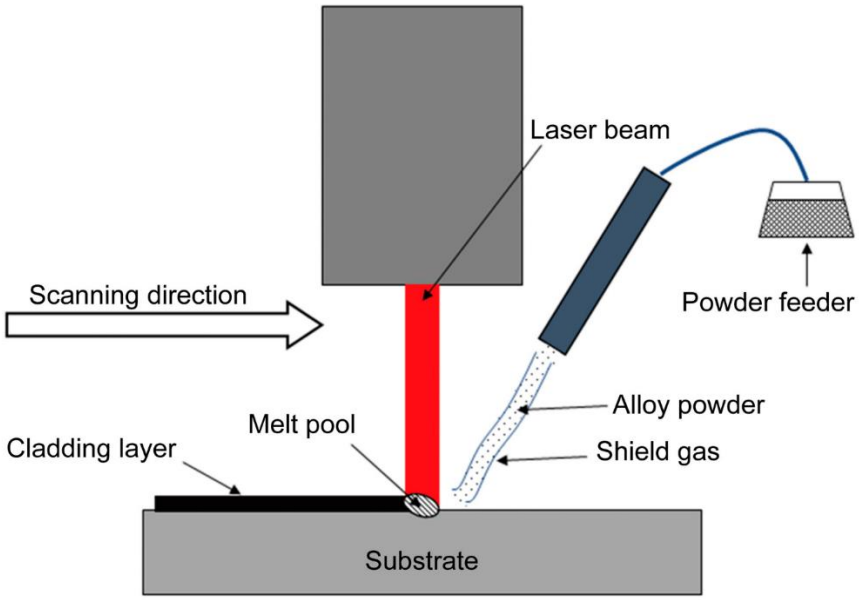

Figure 8 Schematic diagram of the laser cladding technique [60].

Laser cladding was used by Yue *et al.* to fabricate the AlCrFeCoNiCu system on magnesium substrates in 2014, which achieved a dual solid solution with FCC and BCC phases as measured by XRD [61]. The interface of the HEA coating and the Mg substrate was observed to be metallurgically bonded due to Partial Mg melting. In addition, Zhang *et al.* deposited CoCrCuFeNi HEA thin films by laser cladding in 2014 onto Q235 steel substrates [62]. The thin films were tested by annealing with various temperatures up to 1000 ℃. FCC phase was observed with no phase transition after annealing. The hardness and elastic modulus were barely reduced after 750 ℃, indicating outstanding thermal properties.

1.7.2.2.Magnetron sputtering

Magnetron sputtering is a physical vapour deposition technique frequently used to fabricate HEA thin films, in which the material is vapourised onto the substrate by high-energy ion bombardment. HEC thin films could also be deposited by introducing reactive gas like oxygen or nitrogen into the chamber, referred to as reactive sputtering [12]. The base material used to deposit thin films in a sputtering system is known as the target, which is bulk form alloy fabricated by vacuum arc and casting [24]. *Figure 9* shows a schematic representation of the magnetron sputtering system. The target and an adjacent electrode are the cathode and anode of a magnetically enhanced low-pressure glow discharge. A strong magnetic field at the

cathode enables a thin cathode fall region to form at low pressures so that ions generated at the top of the cathode fall can be accelerated to the cathode with few collisions to eject material from the cathode surface. Magnetron sputtering provides benefits including precise adjustment of deposition parameters, low-temperature deposition and good control of film stoichiometry [63]. The disadvantage of this process is that different atoms in HEAs have different sputtering yields, so the equiatomic composition of the thin films is challenging to achieve. The film growth rate is relatively slow, so thicker films in the five to ten micrometres range are hard to synthesise.

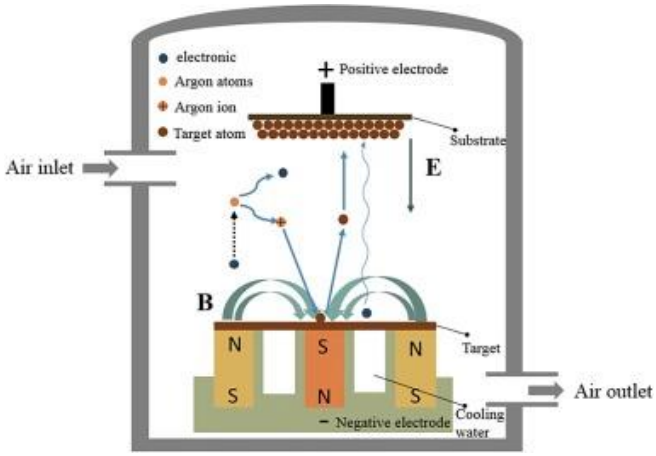

Figure 9 Schematic diagram of the magnetron sputtering technique [62].

For instance, Cheng *et al.* deposited (AlCrMoTaTiZr)N_x thin films in 2011 using reactive magnetron sputtering by introducing an argon/nitrogen binary gas mixture in the chamber [64]. The thin films were deposited at various nitrogen partial pressure ratios $R_{N,}$ which is the percentage of nitrogen partial pressure over the working pressure. A phase transformation from amorphous to FCC orientation through increasing R_N was observed by revealing XRD and TEM. A superior hardness of 40.2 GPa was exhibited at R_N = 40%, and it showed excellent thermal stability without decomposition after annealing at 1000 ℃ for 10 h. $AlCrFeCoNiCu_{0.5}$ nitride thin films were also successfully deposited by Khan *et al.* in 2020 for various RN values. Binary nitrides, including AlN and CrN, were observed via XPS spectra, and the phase transition from FCC to amorphous was obtained at high R_N due to the severe lattice distortion by nitrogen doping. The study achieved a hardness of 9.8 GPa at the highest gas fraction of 25%, which was superior to the hardness of $AlCrFeCoNiCu_{0.5}$ HEA thin films in a range of 6 - 8 GPa [7, 19, 65]. The annealing test and water contact angle exhibited excellent oxidation resistance and high hydrophobicity, respectively.

1.7.2.3.Pulsed laser deposition

Pulsed laser deposition is a high-energy physical vapour technique frequently used in thin film fabrication. *Figure 10* gives the schematic representation of the pulsed laser deposition process, showing that a lens focuses the high-power pulsed laser beam on a HEA target. The surface material of the target is vapourised by the high energy beam, which emits a plasma plume that flows onto the substrate surface. The HEA target used in pulsed laser deposition is generally produced by sintering a HEA powder. It has several benefits for HEA thin film deposition. The characteristics of the laser beam could be precisely adjusted to control the deposition rate and thin film thickness. Moreover, the plasma plume induced by the laser erosion allows the composition and stoichiometry of deposited thin films to be very similar to the original HEA if the deposition takes place in a vacuum environment [59]. The fact that the process could be conducted in a vacuum also allows the formation of ceramic materials by introducing a reactive gas such as oxygen or nitrogen in the chamber.

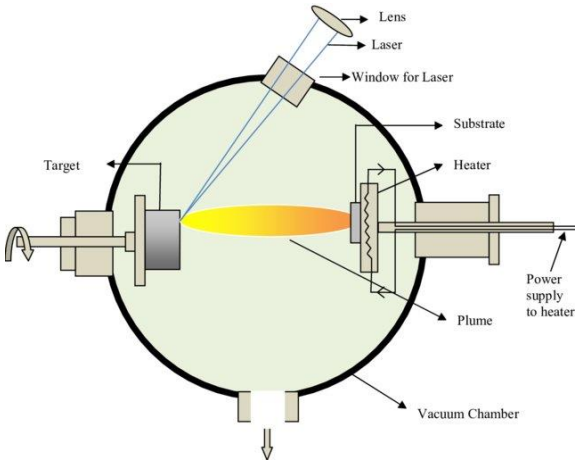

Figure 10 Schematic diagram of the pulsed laser deposition [66].

$CrCoFeNiAl_{0.3}$ HEA thin films were deposited by Lu *et al.* onto silicon substrates using pulsed laser deposition [67]. A single FCC crystal structure has been achieved, similar to the bulk form HEA. The hardness and elastic modulus by nanoindentation increased initially but eventually decreased with increasing deposition time. The maximum hardness of the thin film after two-hour deposition is more than twice as large as the bulk form HEA.

1.7.2.4.Filtered cathodic arc deposition (FCAD)

Cathodic arc deposition is a high-current electrical discharge. It aims to improve the density, adhesion strength, composition and stoichiometry of the deposited film. FCAD consists of a vacuum chamber with an anode adjacent to a cathode and a curved solenoid to guide the plasma ejected from the arc to a substrate at the far end of the coil. [20, 68]. *Figure 11* provides the schematic representation of the FCAD, demonstrating the motion of ejected particles and ions from the cathode towards the substrate. The general principle of an FCAD is that a high current arc discharge of material takes place in a vacuum comprising the cathode through the arc current input, forming a plasma plume. Extremely high energy needs to be input to transform the material to the plasma state. The electrons are pulled away from their shells around atoms and freely move, leaving over the positive charge ions [27]. During discharge, a highly energetic emitting area called a cathode spot is formed, which emits small blobs of very dense plasma. Highly ionized ions of cathode material are ejected from the cathode spot with very high energy, travelling through a magnetic filter towards the substrate. Small blobs of molten cathode material named macroparticles could be ejected simultaneously as the arc discharge due to the high current heating the cathode surface.

FCAD provides multiple advantages over competing techniques. For example, the thin film deposition rate is greater than those achieved with magnetron sputtering [69]. The thin films generated by the FCAD give outstanding adhesion force at the substrate interface due to the highly energetic ion bombardment of the substrate [70]. The FCAD also achieve high density and smoothness of the thin films because the energetic plasma plume gives relatively larger atomic mobility. Moreover, the vacuum environment of the FCAD enables the synthesis of high-entropy ceramic thin films by introducing a background reactive gas during the deposition, a so-called reactive cathodic arc.

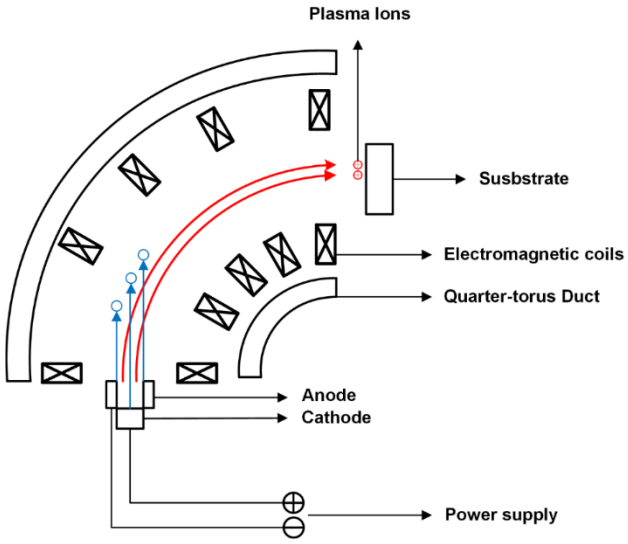

Figure 11 Schematic diagram of an FCAD system.

Some of the HEA and HEN thin films recently reported in the literature have been deposited by vacuum arc deposition. (TiHfZrVNb)N thin films were synthesized by Pogrebnjak *et al.* in 2014 using reactive vacuum arc deposition [71]. The coatings have shown an FCC phase with grain size in a range of 40-60 nm. It established better wear resistance than Steel 45 and achieved a maximum hardness of 44 GPa at a nitrogen composition of 51 at%. Chen *et al.* fabricated AlCrNiTiSi HEA thin films by a multi-arc magnetic-filtered cathodic arc system in 2021 [72]. They altered the substrate bias from 0 V to 200 V and achieved an enhanced hardness of 15.63 GPa at 200 V. FCAD could also synthesise multi-layered alloy coatings. In 2022, Chang *et al.* managed to synthesise AlTiSiM/CrVN/ZrN multilayer coatings by a multi-arc cathodic vacuum arc system on Si (100) and Tungsten carbide substrates [73]. Three phases, including AlTi FCC, CrV BCC and Zr HCP, were observed in the multilayer coatings, forming a hierarchical gradient. The coating obtained a maximum hardness of 31.5 GPa. Zhao *et al*., using an FCAD, investigated the effect of changing substrate bias on the properties of $AlCrFeCoNiCu_{0.5}$ HEA thin films deposited on 304 stainless steel [29]. A transition of the coating-substrate interface from an incoherent to semi-coherent was observed for bias change from 0 V to 50 V. High-strength HEA coating of 8 GPa with a semi-coherent interface was obtained with a substrate bias of 50 V.

The production of plasma in a cathodic arc is generally provided by high current density input. Applying thermal energy and a magnetic field to the cathode could enhance the ion

emission. The emission is an explosive process, so it could not continuously generate plasma. Instead, the emission concentrates on one centre once at a time. The emission centre is called the cathode spot. The next spot usually developed at a random edge of the previous spot. The cathode spot size is in a range of 1 - 10 μm, and the current density is in a range of 1×10^6 to 1×10^8 A per cm. The lifetime of a cathode spot is 10 nanoseconds to one millisecond [20]. The plasma emission, magnetic filtering and film growth mechanisms are introduced briefly in the following sections.

Plasma emission mechanism

For the plasma emission to proceed, a potential barrier between the cathode and the vacuum must be overcome. It is the potential difference between the fermi level inside the metal and the potential in a vacuum. The height of the barrier is called the "work function". Energy is required to overcome the work function by some mechanisms. The diagram plots a negative potential to account for the negative charge. The barrier appears as a hill, and the electron potential gradient goes downhill. The anode could also have a work function [74]. Usually, the electrons could simply fall into the fermi level of the anode, and it explains why the anode gets hot. But if there are excess electrons or the anode is very large, the anode work function could also be significant.

One of the mechanisms to overcome the barrier is thermal emission. The electrons in a metal follow the fermi energy distribution function. At sufficiently high temperatures, the electron may have enough kinetic energy to overcome the work function. The electron emission density could be determined by integrating the distribution in three directions. The result is called the Richardson-Dushman equation :

$$\Delta j_{thermionic} = AT^2 e^{(-\frac{\emptyset}{KT})} \quad (3)$$

Where $A = 1.202 \times 10^{-6}\ A/m^2K^2$ is the universal Richardson constant; ϕ is the work function of the cathode material; T is the temperature.

For the cathodic arc, the effect of the electric field near the cathode surface should also be considered. The strong electric field may narrow the potential barrier, so the electrons have a chance to go through a quantum-mechanical tunnel instead of the classic pathway. In a cathodic arc, both high temperature and field are present, which leads to a nonlinear amplification of the

emission process. The above mechanisms didn't take the time factor into account. In reality, heating and cooling play an important role, and generally, they do not balance, making the temperature a time-dependent variable. A positive feedback loop could form if the field and emission are already highly intense. The Joule heating becomes significant, further enhancing the emission and heating. The location of this occurs to end up in an explosive manner, emitting electrons and plasma.

Cathode spot formation

The explosive emission ends up with the formation of a cathode spot. The spot lifecycle involves four stages: the pre-explosion stage, the explosive emission stage, the immediate post-explosive stage, and the final cool-down stage. Initially, some locations favour spot formation more than others. They usually satisfy features like dielectric contamination or protrusions, which lower the work function [20]. Suppose these features are combined with high field strength and intensity of ion bombardment. In that case, it leads to thermal runaway, which is the positive feedback mentioned before, and the explosive emission starts [20].

The thermal runaway rapidly heats up the cathode spot, eventually evaporating the material and transforming it into plasma. The minimum amount of energy and explosion delay time satisfy this relationship. H is a specific factor dependent on the cathode material but independent of the arc current or any other quantities. Explosions cause the destruction of the macroscopic crater on the surface [75]. In the immediate post-explosion stage, the surface is still hot and molten, with dense plasma near the spot. The thermal-field emission could not be maintained, but the thermal emission remains as the work function barrier is still reduced. Metal vapour starts to form, which "chokes" the emission. The plasma pressure acting on the molten metal causes the formation of microparticles. In the final stage, the emission would reduce exponentially as the temperature decreases, as the Richardson equation suggests. The lower plasma density and neutral vapour further "choke" the emission to a complete stop. The next spot will start forming at a random edge, with a lower barrier and resistance.

The emission could not be maintained for four reasons. Firstly, heat conduction expands the emission area, reducing power density over time. Secondly, the current would choose a more conductive pathway around the spot, as the resistance is the largest at the bulk directly under the spot [74]. In addition, the emission spot itself forms the highest resistive barrier due

to the phase change that chokes the emission, further reducing the current transfer ability. Finally, a new spot comes into play, which takes over the current. The motion of the apparent cathode spot is random without the presence of a magnetic field. A new spot could be formed in any direction of the existing emission centre with equal probability. However, random motion only appears if no disruptions exist, such as external magnetic fields, scratches, contaminations, or interfaces between different materials on the cathode surface [74].

Macroparticle filtering

Metal droplets called macroparticles are formed during the emission process, which flow toward the substrate with the plasma. These are liquid metals initially and cool down on their way toward the substrate. The collision between the macroparticles and substrate causes roughness and defects on the surface. It will impact the film's strength and mechanical properties in most cases. There are two ways to remove the macroparticles. The first thing is to reduce them in the first place, which means during the emission process, the second is to separate them from the plasma field using a filter [74].

Reducing the lifespan of apparent spots is an essential way to limit macroparticles. It could be done by manually increasing the resistance, increasing the arc current, and using a pulse arc instead of a DC arc. *Figure 12* compares the copper macroparticle distribution for DC arcs and high current pulse arcs, which shows that pulse arc generates fewer macroparticles in most cases. High currents could also bring drawbacks, such as breaking down the anode and chamber wall.

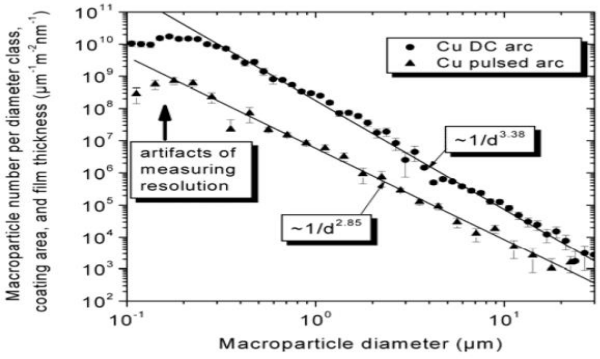

Figure 12 Comparing the copper macroparticle distribution for DC and pulsed high current arc [68].

The fundamental concept of a macroparticle filter is to guide the plasma flow along the magnetic field line. The field hardly affects Macroparticles with larger mass, even with some

charges. They will move in a relatively straight line. The classic filter design is a part of the vacuum chamber with the guiding field coils. There is still a chance for the macroparticles to reach the substrate with the presence of a filter. They could bounce the chamber wall several times. They could also be carried by the plasma field, which fast plasma past momentum to the particles. Another drawback is that there will always be plasma loss during the filtering. Therefore, the filter quality is determined by the ratio between the ion current of the filtered ions and the arc discharge current, usually in the range of 1% to 4% [74].

Film growth factors

For the cathodic arc, most film-forming ions exceed the displacement energy, so they will penetrate the surface and rest under it. The penetration makes the film rigid and shows high intrinsic stress. The defect of the film may also be higher [76]. If the stress is too excessive, it might result in catastrophic failure. If the kinetic energy is reduced so that ions cannot penetrate, the film defect could be lower, and adatom mobility could be enhanced. Therefore, the arrival energy of ions should be an important feature to be considered in film deposition.

The ion arrival energy could be written as the sum of the kinetic energy, ionization energy, and cohesive energy. Ion kinetic energy includes the natural kinetic energy gained from the cathode spot and the kinetic energy due to the negative substrate bias. The ionization energy takes up a major part of the potential energy of the arriving plasma. There are multiple charge ions, so the cumulative ionization energy is used. Moreover, the energy of a bound electron at the excited state, the presence of molecules in the plasma field, and the cohesive energy released should also be considered in the arrival energy. The substrate is usually applied with a negative potential referred to as substrate bias. It aims to control kinetic energy to utilise the film property. Macroparticles could be further removed since particles with different charges and masses would experience different accelerations. If the bias is too high, it could result in sputtering on the surface or bouncing back from the surface, slowing down the deposition [74]. Another parameter is the substrate temperature. The ion bombardment could cause a temperature rise comparable to conventional heating. The heating effect helps to form dense film, higher adatom mobility, and enhanced surface reactions. However, if the substrate temperature is too high, it might cause the melting and reevaporating of material [76].

Chapter 2

Material and Methodology

2.1.$AlCrFeCoNiCu_{0.5}$ nitride thin film deposition

2.1.1. $AlCrCoFeNiCu_{0.5}$ HEA cathode

The cathode used in this thesis to fabricate HEN thin films was a vacuum arc melted stoichiometric $AlCrFeCoNiCu_{0.5}$ target, see details in chapter 4, Table 5 Composition of the $AlCrFeCoNiCu_{0.5}$ HEA cathode used for FCAD. The cathode was selected because the composition of the thin films could be altered precisely by varying the FCAD parameters to achieve a wide range of possible microstructures. For example, changing the composition of Al would determine the crystal phase of the fabricated thin films in between the BCC and FCC. The composition of Cu in the cathode was half of the rest of the elements so that the phase segregation could be avoided. Fe, Cr, Co, and Ni were included in the cathode due to their excellent mechanical properties and exceptional oxidation and corrosion resistance that has been well demonstrated. The elements used were also relatively ambient and cheap, and the process of target formation was industrially optimized. Therefore, the film could be fabricated commercially in many scenarios. The HEA target used in this thesis was made by ACI Alloy Inc. using vacuum arc melting and casting techniques. It obtained a purity of 99.95%, and the impurities detected were carbon and oxygen. The cathode was an alloy cylinder with a diameter of 44 mm and a height of 36 mm.

2.1.2. Substrate preparation and cleaning

The silicon wafers used as the substrate for the thin films were washed and cleaned before being loaded to the substrate sites of FCAD. In this experiment, commercially used single-crystal silicon wafers with an orientation of (100) were applied to deposit the high entropy nitride thin films. The wafers were 800 μm thick and polished on one side where the thin films

were deposited. The wafers were cut into 50 mm × 25 mm pieces with a diamond pan to fit the substrate holder.

Surface contamination of the substrate, such as dust, organic material, and silicon particles, could affect the roughness of deposited thin films, as well as cause surface delamination and segregation. To remove the surface contamination, the cleaning followed a process of acetone-ethanol-deionized water washed in an ultrasonic water bath in a flame hood. Substrates were washed in each solution for 15 min, dried in compressed nitrogen for 30 s to ensure no residual liquid, and then rested in the air for 10 min before loading into the substrate holder.

2.1.3. Thin film deposition

$AlCrFeCoNiCu_{0.5}$ nitride thin films were deposited by an FCAD at various nitrogen partial pressures using a magnetic-filtered high-voltage arc system. It comprises an electrode with a pulsed trigger and a quarter-torus magnetic filter. The detailed configuration of the FCAD system was shown by Marcela *et al.* [77]. The thin films were deposited via plasma bombardment created by the cathode material from applying a high-voltage current pulse at the centre of the cathode. The potential difference between the cathode and anode causes an explosive process that evaporates the cathode material. HEA cathode was mounted in the centre of a hollow copper anode with an inner diameter of 44 mm, an outer diameter of 33 mm and a length of 42 mm. The outlet of the anode pointed towards the duct. A half semicircle torus current-carrying coil (duct) with 22.5 turns, 440 mm in radius, and 140 mm in cross-sectional diameter was used to filter the neutrally charged particles from the plasma by creating a magnetic field [65]. The substrate was held by a stainless-steel holder at the exit of the magnetic filter.

In this thesis, the HEN thin films were deposited in a reactive FCAD, in which a binary gas mixture of nitrogen and argon was introduced into the vacuum chamber. Therefore, two gas pipelines of nitrogen and argon were connected to the chamber at the substrate side, in which the flow rate was controlled by the flow meter installed in the pipeline. The nitrogen partial pressure was controlled by adjusting the flow ratio between the two gases.

2.2.Characteristic techniques

To study the effect of nitrogen addition in-depth, several characteristic techniques were applied to evaluate surface geometry, topography, surface chemistry, microstructure, and mechanical properties. The film's thickness contributing to the deposition rate was measured by profilometry. Scanning electron microscope and atomic force microscopy were used to determine the surface morphology of the films, such as the density of macroparticles and the columnar structure of the metal nitrides. Energy dispersive spectroscopy was applied to map the constituent element composition over the deposited film. X-ray photoelectron spectroscopy monitored the binding energy and investigated the film chemistry at various nitrogen concentrations. The crystallography of thin films was evaluated by X-ray diffraction. The hardness and elastic modulus were measured by nanoindentation testing.

2.2.1. Profilometry

A stylus profilometer is a physical scanning probe that is used to detect the surface topography and roughness of an object. *Figure 13* gives a representation of a profilometer in which a diamond tip measures the film thickness through step height monitored by a computer. The measurement takes place by contacting and moving a needle-like diamond stylus vertically across the selected surface of the sample. By recording the position of the stylus, it aims to measure small variations in a vertical direction, which produces a pattern with a change in position over the scanned distance. The profilometer does this by monitoring the force that the sample is pushing up onto the stylus and creating a feedback loop as the response to the change. A computer controls the x-y stage of the tip at the surface of the sample. The scan length, duration time, stylus force and vertical scan range, which determine the resolution, could be manually set in the software. The film thickness (d) was measured by the height difference between the film and substrate surface, which was created by covering up a part of the substrate with a mask during deposition.

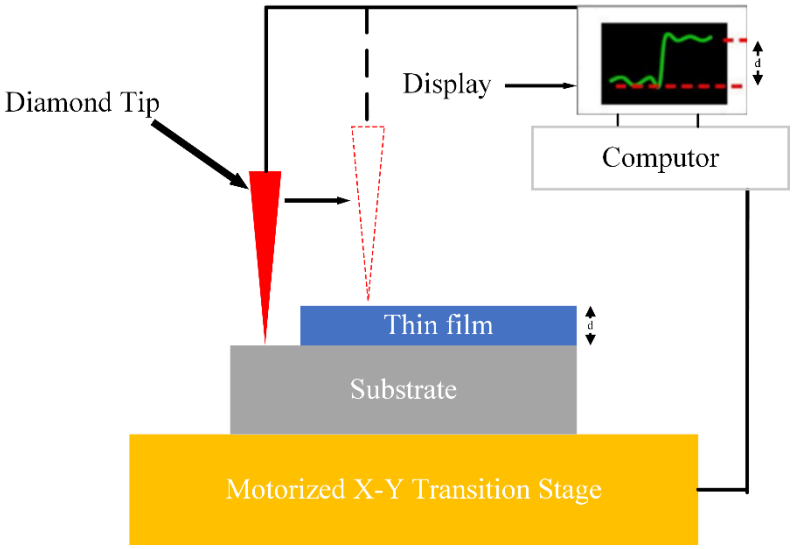

Figure 13 Schematic features and working principles of a stylus profilometer.

A DektakXT stylus profilometer (Bruker, USA) was used to measure the thickness of HEN thin films. Sharp steps were created between the thin film surface and substrate using a physical mask during the deposition. The average thickness was taken at 20 distinct positions evenly distributed on the sharp steps for each sample using a standard stylus. A scan length of 1 mm and a scanning speed of 30 μm/s were used.

2.2.2. Scanning electron microscopy (SEM)

SEM is applied to obtain the surface morphology of thin films. Other features such as chemical composition could also be investigated by incorporating additional detectors. The primary function of a scanning electron microscope, just like the optical microscope, is to enlarge an object's surface feature and topography. The major difference is that SEM generates an electron beam to scan the surface instead of the visible light used in an optical light microscope. The SEM obtains higher resolution and finer detail of a feature, due to the much smaller wavelength of the electron beam. In addition, by hitting the specimen with an electron beam, an x-ray could be emitted due to the excitement of core-shell electrons, which is detected to measure the element composition referred to as energy dispersive spectrometry (EDS).

The SEM scans the specimen by moving the electron beam side to side of the object and gradually moving down to create a whole image. *Figure 14* provides a visual representation of an SEM. Electrons emit from an electron gun, pass through an anode and magnetic lenses in a high vacuum column chamber and reach the sample surface. Electron detectors are installed to

receive the scattered electrons from the sample. In most SEM systems, the electrons are accelerated to a voltage of 30 kV. The scattered electrons emitted from the specimens generate a wide range of signals, including secondary electrons, back-scattered electrons, transmitted electrons, Auger electrons, and X-rays [78].

The secondary electrons are the electrons emitted due to the inelastic scattering between the primary incident electrons and the atoms within the specimen. The number of electrons is counted so that the intensity of the signal is dependent on the surface features. The SEs have relatively lower energy, around 50 eV, which lowers their depth of pentation in a matter [79]. This concept allows the SEM to take images with a resolution below 1 nm since the SEs are highly concentrated at the point of intersection between the electron beam and the surface [79].

Backscattered electrons are the electrons emitted due to elastic scattering, which causes electrons to change their direction without changing the wavelength so that they do not lose much energy. In comparison, the SEs undergo an inelastic scattering process in which the primary incident electrons lose energy. They have larger energy than SE, emitting from a deeper layer within the specimen. Therefore, the resolution of BSE is smaller than SE mode. However, the benefit of the BSE is that it could provide information about the atomic number of the sample, which could help to determine the distribution of components within the specimen in analytical SEM.

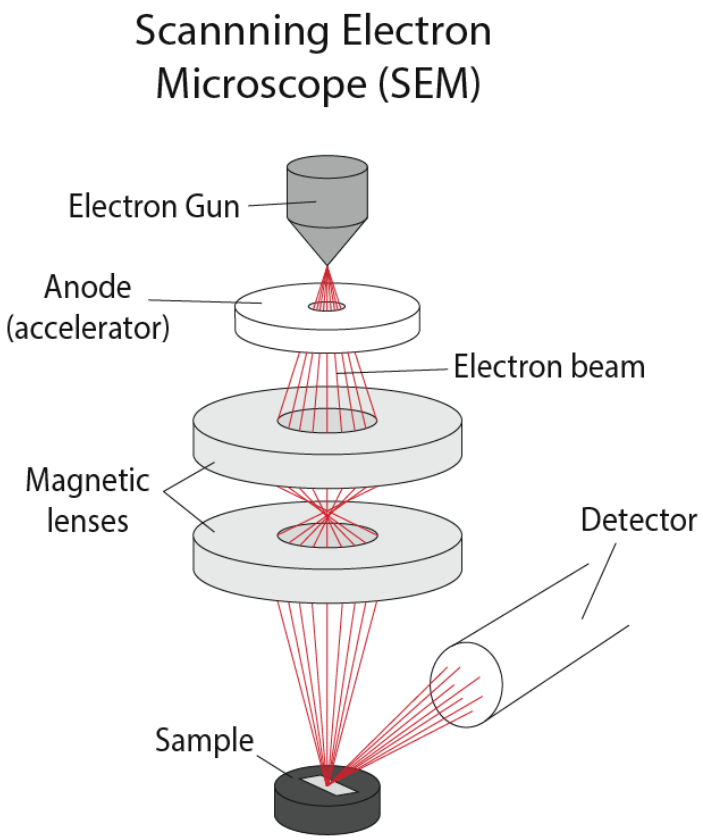

Figure 14 Schematic representation of SEM features with a secondary electron detector [80].

In this thesis, the HEN thin films were investigated by a SEM to study the surface morphology, grain size and roughness. The thin film samples were cut into smaller 10 mm × 10 mm pieces and loaded onto the specimen tub. A Zeiss Sigma HD SEM operated at an Inlens mode (SE detector), and a low accelerating voltage of 5 kV was applied to scan the surface of the thin films. The aperture size was 30 µm, and a working distance of 5 mm was maintained.

2.2.3. Electron dispersive spectroscopy (EDS)

EDS is used to determine the surface chemical composition of the HEN thin films in terms of atomic % by measuring the characteristic X-ray signal generated by the electron interaction in SEM. The EDS detector is installed in the SEM vacuum chamber. As mentioned above, the electron beam generates a wide range of signals at the specimen surface, and the type of signal detected depends on the interaction volume and the depth of the specimen. *Figure 15* gives a visual representation of the interaction volume in which various signals were emitted from the

specimen. The characteristic X-ray signals are generated by the inelastic scattering of electrons with sample atoms. The electrons of atoms are excited to higher orbitals by collision with the incoming electron beam, which then lose their energy to produce an X-ray and drop down to lower orbitals. The wavelength of the generated X-ray from an atom specifically characterizes the element, and the intensity of the signals determines the composition. The X-ray signals are more likely to escape than scattered electrons, even from the deep inside of the specimen, so a higher accelerating voltage is needed to obtain reliable EDS X-ray signals. The depth of beam penetration and interaction volume could be controlled by altering the accelerating voltage of the SEM.

In addition to composition analysis, EDS maps, with coloured representations of individual elements, could also be obtained from the acquired EDS data. It aims to study the homogeneity of the sample surface. The maps are generated by acquiring X-ray signals from the regions on the sample scanned by the electron beam over a set period depending on the resolution and dead time. A layered image of the acquired region is produced by combining the EDS maps of individual elements represented by various colours, which shows the spatial distribution of all the elements at the surface in one image. The analytical software installed on the computer linked with the instrument is used to analyse the EDS spectra and maps.

In this thesis, an Oxford instrument EDS was used to measure the element composition of the thin film of $AlCrFeCoNiCu_{0.5}$ nitride deposited at different nitrogen fractions. The EDS data was collected immediately after the SEM morphology images were acquired so that the vacuum of the chamber was not broken, and the same sample surface was applied for EDS analysis. EDS mappings were also performed to show the element distribution and homogeneity. Each image has been taken within a scale of 100 nm, with a secondary electron mode to ensure a maximum analyzing depth of 200 nm. The operating voltage was 20 KV, with a working distance of 17 mm, an aperture size of 30 μm, and a standard mode. The EDS detector was fully inserted in the SEM chamber mentioned above. The compositions and EDS mapping were processed by Aztec Analysis software.

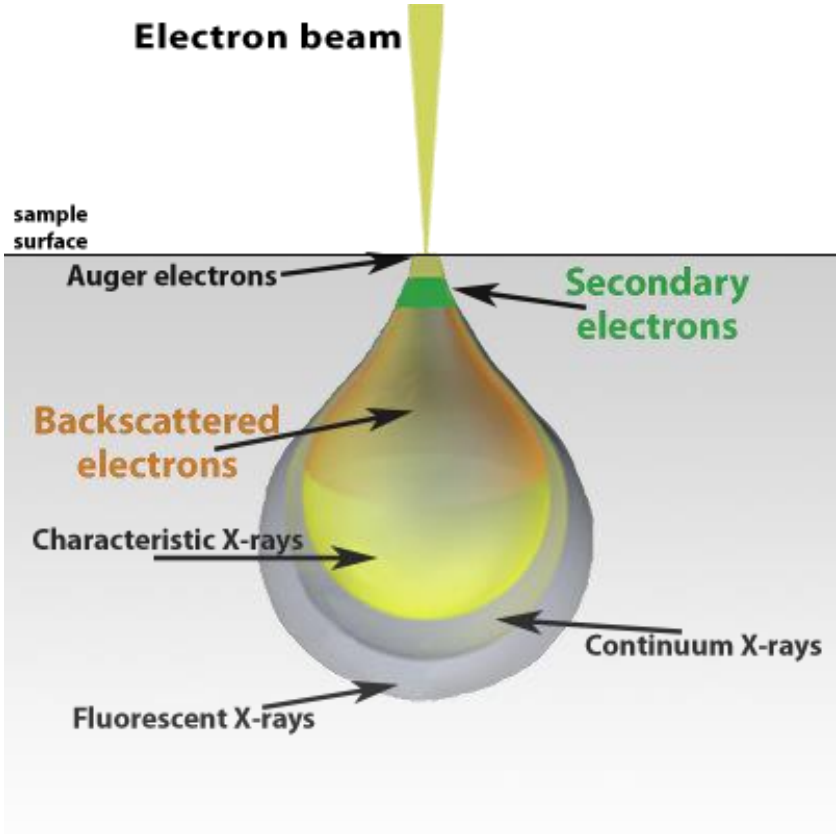

Figure 15 Schematic representation of the various signals generated at different interaction depths and volumes by the SEM scanning electron beam [81].

2.2.4. X-ray photoelectron spectroscopy (XPS)

XPS is a surface analytical method using a high-energy X-ray, which determines the chemical composition and surface chemistry of the samples. The photoelectrons generated from the samples carry information about the bonding energy of elements such as metallic bonds, ionic bonds, covalent bonds, etc, as X-ray irradiates the sample surface. A schematic representation of an XPS system in which X-rays are produced by a metal anode excited by an electron gun is shown in *Figure 16*. Since the photoelectrons have a short free mean path, XPS is more surface sensitive, providing quantitative information from a depth of about 10 mm of the samples [56]. The incident X-rays are positioned onto the sample by focusing optics. The absorption of X-ray energy exceeds the binding energy of core-shell electrons, resulting in an ejection of electrons. The kinetic energy of the emitted electrons is measured by a hemispherical detector. The binding energy could be determined as follows:

$$E_{binding} = h\nu - (E_{kinetic} + \phi) \quad (4)$$

Where $E_{binding}$ is the binding energy of a particular atom orbital; hν is the X-ray energy of

incident specified by the instrument; $E_{kinetic}$ is the kinetic energy of the detected electrons; and ϕ is the work function of the detector.

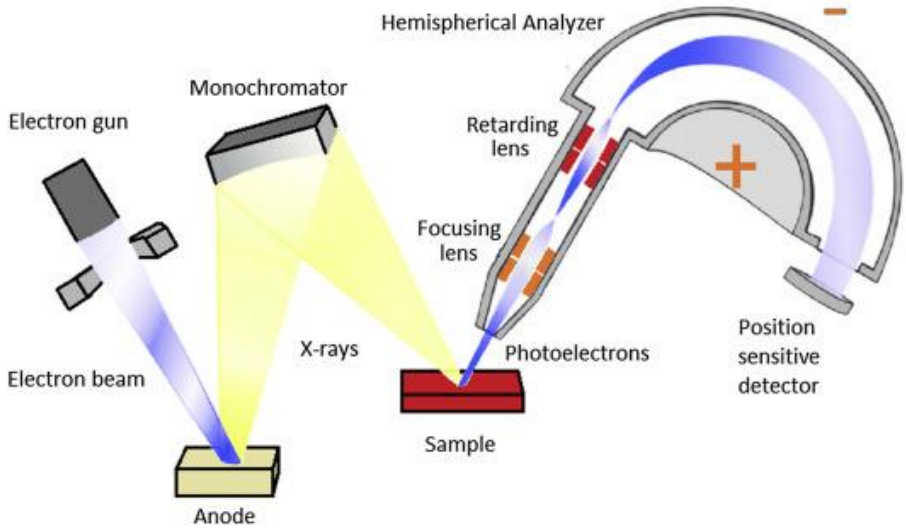

Figure 16 Schematic representation of the XPS system and working principle [56].

This thesis performed an XPS to determine the surface chemistry and binding energy of the HEN thin films using a Thermo K-Alpha+ instrument. Measurements were carried out with monochromatic Al Kα radiation. The wavelength was 0.834 nm, and the probe size was 400 μm. Ar^+ etching was performed to remove the surface contamination at 300 eV for 240 s. The X-ray source was operated at 12 KV and 6 mA. The XPS survey spectra were obtained with a step size of 1 eV, and high-resolution spectra for each element were obtained with a step size of 0.1 eV. XPS data analysis was performed using ORIGIN analysis.

2.2.5. X-ray diffraction (XRD)

X-ray diffraction (XRD) is a commonly used analytical technique in material science, which aims to identify a material's phases and crystal structure and provide information on the unit cell parameters. The principle of XRD is generally the constructive interference between the crystal sample and the X-ray. In an XRD analysis, X-rays are produced from a cathode rate tube by bombarding a target material with electrons generated from a filament and accelerating them by voltage [82]. Like in SEM-EDS, the primary electrons have sufficient energy to eject the inner shell electrons. Character X-rays will be produced when the outer shell electron fills the electron hole. The specific wavelength of the X-rays depends on the target (Fe, Cu, Mo, Cr, etc), commonly referred to as Kα.

The X-ray will be focused and directed to the sample, which scatters the crystal atoms, excites the atom electrons through an elastic scattering process. The excited electrons then produce regular sets of X-ray waves [83]. Two types of interference might occur. In most directions, the waves cancel each other out, known as destructive interference. In a few specific directions, however, the amplitude of each wave will be added up to reach a maximum, referred to as constructive interference [84]. The output X-ray due to the constructive interference will be collected and courted by an X-ray detector placed on the other side of the X-ray resource. Normally, both the source and the detector will move simultaneously from various angles over the sample surface to collect signals from every possible direction and produce a spectrum. The relationship between the incident wavelength and the position of peaks satisfies Bragg's law [83]:

$$n\lambda = 2dsin(\theta) \tag{5}$$

Where n is an integer that represents the diffraction order; λ is the wavelength of the incident X-ray; d is the spacing of crystal layers; and θ is the angle between the incident wave and the scattering plane. From a common XRD spectrum, the signal positions are given in two-theta. Therefore, the signal positions need to be halved for calculation.

There are normally three factors that are determined by the XRD. First is the lattice parameter, which is the distance between two points on the edge of a unit cell and aids in evaluating the symmetry of the crystal. D spacing in Bragg's law is highly related to the unit cell configuration, which could then be used to determine the lattice parameter once the crystalline phase has been identified [84]. The second is the crystalline phases, which could be determined by matching the spectrum with an existing database. For example, the common way to identify an FCC structure is to fit the spectrum with the data of pure copper [40]. The intensity of the peak measures the quality of the crystalline phases. Another factor that XRD could demonstrate is the grain size (L), through the Scherrer equation [83]:

$$L = \frac{K\lambda}{\beta} * \cos(\theta) \tag{6}$$

Where K is the shape factor, usually taken as 0.89; β is the full width at half maximum of the peak. This equation gives the relationship between the position of the peak, the width of the peak, and the grain size.

In this thesis, the crystal structure investigation of HEN thin films was performed by an X'Pert Power XRD. The instrument was equipped with a copper X-ray source and a Bragg-Brentano configuration, with an operating voltage of 45 V and a current of 40 mA. Each scan analysis was taken in a range from 20° to 90°, with a step size of 0.0131°, and a counting time of 219.045 s. The XRD spectra was processed by Origin software, and peak fittings were carried out using a database installed in PDF4+ software.

2.2.6. Atomic force microscopy (AFM)

An AFM is like a stylus profilometer but with a higher sensitivity, which scans the sample surface with a probe and measures the force between the sample and the probe. Due to the larger sensitivity, it is primarily used to measure the surface roughness and build a 2d&3d map representing the surface morphology. The schematic representation of the AFM system and the working principle is provided in *Figure 17*. The samples are placed on a controlled piezo platform, which can move in the horizontal x-y plane and vertical z-plane. The repulsive force acting onto the tip is measured by the displacement of a reflected laser beam irradiating the surface of the cantilever. A photodiode records the height movement in the z direction. A feedback controller processes the laser signal and generates a topographic image of the area of interest with computer software.

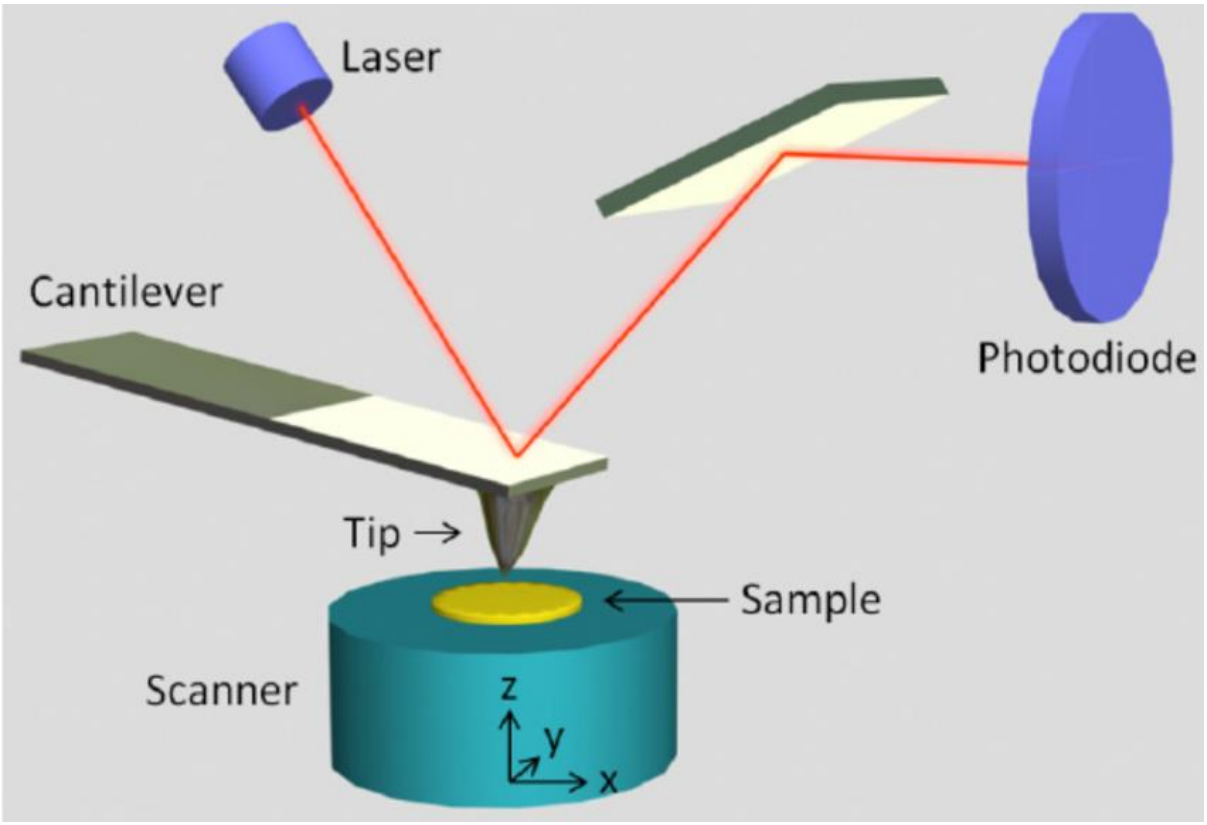

Figure 17 Schematic diagram of the AFM system [85].

In this thesis, HEN thin film surface morphology and roughness measurements were carried out using an AFM (Bruker, USA). The scanning area on the surface was set at 1 μm × 1 μm and a scan rate of 1 Hz was used. The contact mode was used, and its amplitude setpoint voltage was 250 mV. Surface roughness and three-dimensional images were determined by NanoScope analysis software from AFM.

2.2.7. Nanoindentation

Indentation is a traditional probe to test a material's hardness and other mechanical properties. The basic principle is pressing a well-known and hard material into the surface of the unknown sample. The hard material is usually diamond and referred to as the indenter tip. As the tip is pushed into the surface, the force referred to as the load on the tip builds up, until the tip reaches a depth defined by the operator [86]. The hardness of sample H could be quantified by recording and taking the ratio between the maximum load experienced by the tip P_{max} and the area of residual indentation, A_r. The hardness of the material could be calculated by the following equation:

$$H = P_{Max}/A_r \tag{7}$$

The elastic modulus is another important factor that contributes to the deformation resistance of the thin film, as a part of its mechanical properties. It is a measurement of how much the object can resist being elastically deformed from a force applied to it. It is defined by the elastic deformation slope in a stress-strain curve and expressed as the ratio between the stress, which, in this case, is referred to as hardness and strain [86]. Strain is a unitless factor that accounts for some shape parameters that have been changed during the application of stress. Young's modulus *E*, which could be used interchangeably with elastic modulus in nanoindentation, could be calculated by the following equation:

$$\frac{1}{E_e} = \frac{1-\nu^2}{E} + \frac{1-\nu_i^2}{E_i} \tag{8}$$

Where ν is the Poisson's ratio of the sample; the corner mark i represents the property of the indenter; E_e is the effective elastic modulus, which could be calculated by the equation below:

$$S = \beta \frac{2}{\sqrt{\pi}} E_e \sqrt{A_r} \tag{9}$$

Where $S = dF/dh$ is the measured strain; β is a geographical constant. A representation of the relationship between load F, indention depth h and strain S, is shown in *Figure 18*.

The traditionally used macro & micro scale indentation has a relatively large tip, which does not provide a good resolution for a nanoscale thin film. Nanoindentation improves the measurement by using a nanoscale tip with a precise shape, obtaining better resolution in positioning the indent and general real-time data on load displacement. It usually includes the following components: a tip attached to a suspend shift, two transducers for the load and a displacement measurement [87]. The measurement of hardness in nanoindentation is different from the traditional method. The area of residual plastic indentation is replaced by the contact area at maximum load. Therefore, the hardness could cover the resistance of the object to any type of deformation, including elastic and plastic.

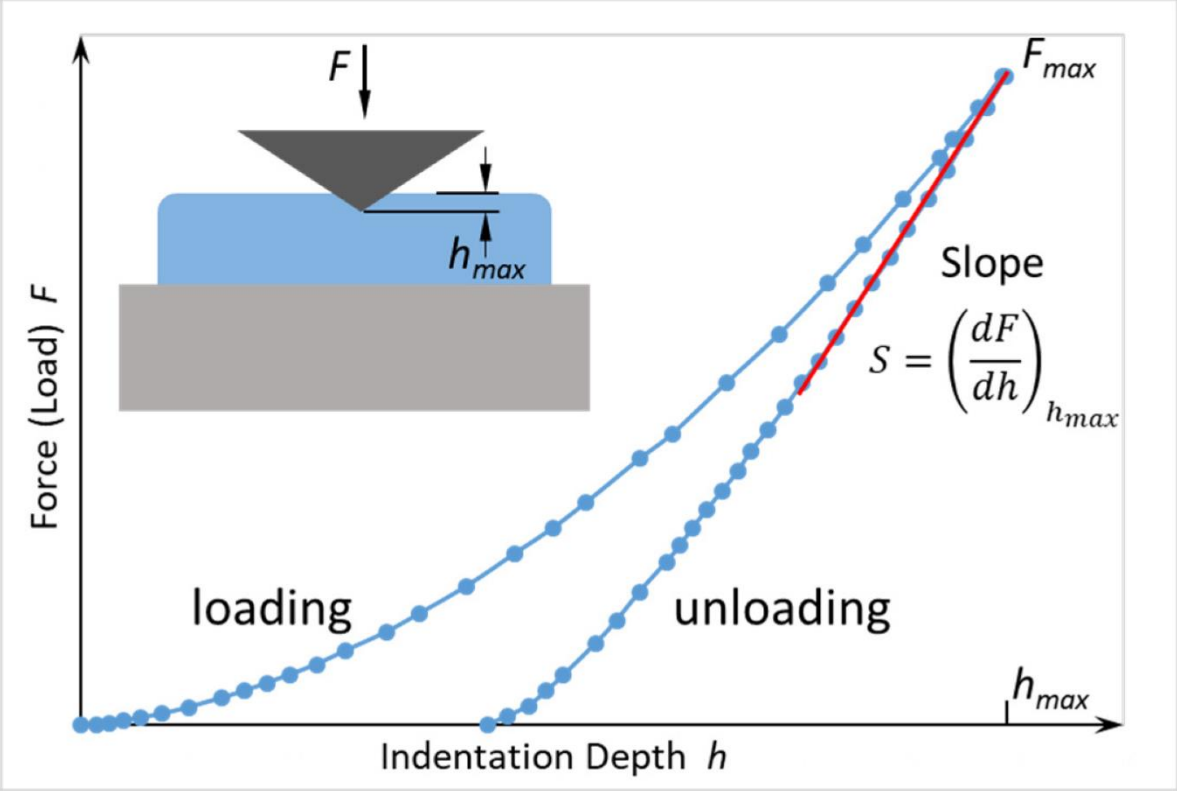

Figure 18 Schematic representation diagram of loading and unloading curves in indentation tests [88].

In this thesis, the mechanical properties of HEN thin films were determined by carrying out nanoindentation with a Hysitron TI 850 Tribo Indenter. Tests were performed by applying a maximum load of 4000 μN on the film surface using a conical tip indenter with a radius of 0.15 μm. The maximum depth of contact was controlled below 10% of the film thickness to avoid the artifacts of the substrate on the measurements by a so-called thumb rule [89]. Sixteen indents were made at different positions on the surface of each sample, and 10 μm was applied to prevent interactions between indents. A load-control feedback setting was used for each measurement after trials. The hardness and reduced elastic modulus were obtained from each indent and averaged.

Chapter 3

Selections of Arc Discharge and Deposition Rate for $AlCrFeCoNiCu_{0.5}$ HEN Thin Films

A major factor that determines the deposition rate and thin film microstructure is the kinetic energy of the plasma discharge delivered by the discharge current. The arc discharge also greatly impacts the composition and stoichiometry of the as-deposited thin films. The discharge current normally depends on multiple factors, including the arc capacitor bank voltage (V_c), the cathode material, the pulse frequency, the pulse length and the pulse shape. For an reactive cathodic vacuum arc deposition, the reactive gas could influence the stoichiometry of the cathode surface throughout the deposition by forming a ceramic layer [16]. The variations in the arc discharge were studied prior to the characterization of the as-deposited thin films. The pulse shape selection, the arc current and the deposition rate are discussed in this chapter.

3.1.Deposition preparation and parameters

The silicon wafers used as the substrate were pre-treated by the steps described in section 2.1.2. Step heights for the profilometry measurements were provided by a physical mask covering the substrates, made by drawing lines across the substrate at a distance interval of 15 mm with a marker pen. During depositions, the arc current, working pressure and duct current were kept constant to avoid their effect on the ion energy. The arc current was obtained from the oscilloscope measurement by wrapping a Rogowski coil around the cathode. The arc current and duct current data of each pulse were recorded by the oscilloscope during the depositions and processed by MATLAB software in a computer. Each pulse's electric charge in Coulomb was calculated by integrating the current proportional to the total number of ions ejected from the cathode. The arc current was 1100 ± 100 A on average by applying a V_c of 150 V. The arc current and duct current were chosen based on the system testing via experiment. The chosen parameters ensure a sufficient, stable, and intense plasma flow, delivering a reasonable deposition rate of 1.5 nm/min under a working pressure of 5×10^{-4} Pa. The substrate

bias was grounded to reduce the impact of re-sputtering on the substrate surface.

HEN thin films of $AlCrFeCoNiCu_{0.5}$ were deposited at various nitrogen partial pressures. The vacuum chamber was first pumped down to a background pressure of 4.5×10^{-4} Pa prior to the deposition to limit the effect of residual air. A nitrogen and argon binary gas mixture flowed through the chamber during the deposition. The nitrogen partial pressure ratio $R_N = P(N_2) / (P(Ar) + P(N_2))$ was changed to adjust the nitrogen concentration in each thin film. The nitrogen and argon flow rate was controlled by mass flow controllers installed in the pipeline connected to the vacuum chamber. The total flow rate of the two gases was also controlled for all depositions to ensure a constant working pressure of 4.5×10^{-2} Pa in the chamber. The as-deposited samples were treated again with the Acetone-Ethanol-Deionized water process to remove the marker pen lines and thus generate profilometer steps. The nitrogen partial pressure ratio, nitrogen and argon flow and the base pressure are given in Table 3.

Table 3 Deposition parameters for each deposition of $AlCrFeCoNiCu_{0.5}$ HEN thin films

Nitrogen partial pressure ratio R_N (%)	Nitrogen flow rate (SCCM)	Argon flow rate (SCCM)	Nitrogen partial pressure (Pa)
5	0.178	3.382	2.25×10^{-3}
10	0.365	3.285	4.50×10^{-3}
20	0.765	3.060	9.00×10^{-3}
50	2.385	2.385	2.25×10^{-2}
100	7.350	0.000	4.50×10^{-2}

The remaining deposition variables that are not adjusted are listed in Table 4. These parameters were chosen based on the previous works on FCAD deposition completed by Zhen *et al.* [38] and Zhao *et al.* [90].

Table 4 The list of deposition variables of CAD chosen for HEN synthesis.

Variables	Selected value
Arc capacitor bank voltage V_C	150 V
Duct capacitor bank voltage V_D	50 V
Base pressure	4.5×10^{-4} Pa
Pulse length	600 μs
Pulse frequency	2 Hz
Substrate bias V_B	0.0 V (grounded)

3.2.Result and discussion

3.2.1. Pulse selection

A speed-up capacitor was connected to the cathode to ensure a constant and smooth release of energy from the powder bank for each pulse. Prior to the actual deposition, test pulses were taken, and the arc current was measured to evaluate the change in pulse shape by connecting the speed-up capacitor in a reactive FCAD. *Figure 19* compares the pulse shape with and without the speed-up capacitor connected, using a nitrogen concentration of 100%. The pulse without the speed-up capacitor connected showed a shark-fin shape, in which the current reached its maximum of 1880 A at 600 μs. The current dropped rapidly after the crowbar was fired at 600 μs.

The pulse with the speed-up capacitor connected shows a more square-like shape, and the current reaches its first peak in 50 μs as the capacitor is charged up. Then the current forms a valley at 190 μs as the capacitor gradually releases energy. It forms a second high-end of 2327 A at 600 μs. The total charge in Coulomb (C) transferred by the pulse is determined by integrating current over time, which in this case is represented by the area under the pulse curve, calculated as follows:

$$q = \int_{t_i}^{t_f} I dt \tag{10}$$

Where q is the electric charge in coulomb; t_i is the initial time; t_f is the final time; I is the net

outward current; and *dt* is the change in time. By MATLAB integration, the average electric charge of the shark-fin pulse and the square pulse given by 1000 pulses are 978 C and 1163 C, respectively.

It indicates that the installation of a speed-up capacitor provides a significant increment of the arc discharge without increasing energy stored in the cathode initial capacitor. The increment in the discharge of each pulse could provide several advantages. In addition, more electric discharge means a greater quantity of plasma generated in one single pulse, which benefits the nucleation rate in thin films forming larger grains [91].

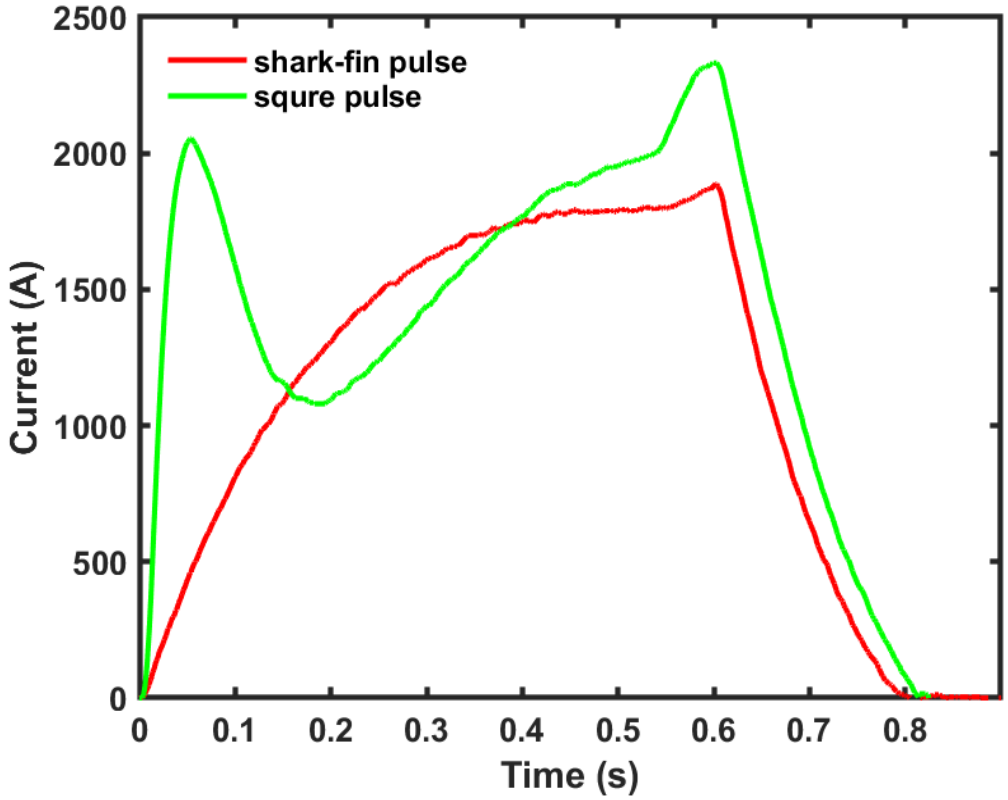

Figure 19 Measured pulse shape with and without connecting the cathode to the speed-up capacitor.

3.2.2. Arc discharge with controlled nitrogen partial pressure

To understand the deposition process in a reactive environment, the effect of nitrogen partial ratio toward the discharge was studied. *Figure 20* shows the pulse shapes at 200, 4000, and 8000 pulses in a 100% nitrogen environment. The first pulse is given at 200 to minimise the impact of the unstable stage of the deposition caused by the oxygen-enriching layer formed on the cathode surface in the ambient air before being pumped down [75]. The electric charge

at 200, 4000 and 8000 pulses are 1103, 1099 and 1112 C, respectively. Only small pulse shape variations are observed throughout the deposition, indicating a stable and uniform discharge for 8000 pulses. The results suggest that the reactive environment of FCAD in a pure nitrogen atmosphere causes a minor effect on the pulse shape at the cathode in a continuous process.

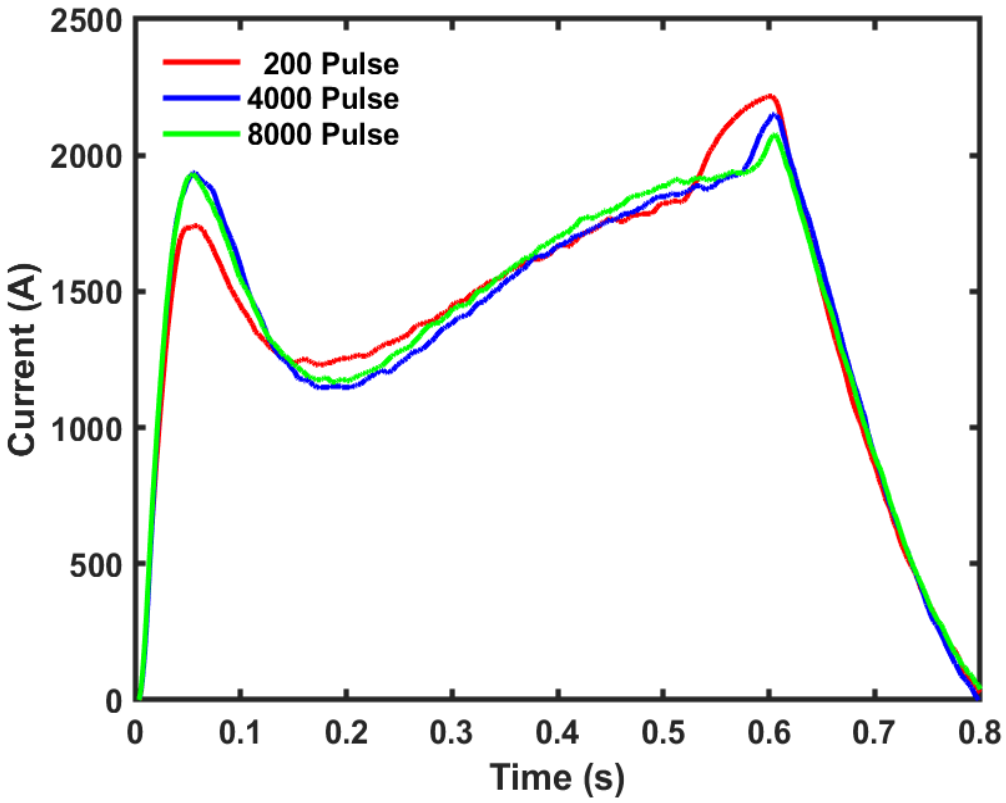

Figure 20 The Discharge current of the FCAD at pulse numbers 200, 4000, and 8000 at R_N = 100%.

Figure 21 gives the change in electric change in a set of depositions with 8000 pulses. The data has been modified with a moving-average filter installed in MATLAB to smooth the noise. It slides *windowSize* in length along the data, computing the average of the data contained in each window. The difference equation defines the moving-average filter of a vector as follows:

$$y(n) = \frac{1}{windowSize} \times (x(n) + x(n-1) + \cdots + x\big(n - (windowSize - 1)\big)) \quad (11)$$

Where y represents the filtered vector; *windowSize* represents the window of length; and x represents the input vector. For our analysis *windowSize* was chosen to be 100. It is observed that the electric charge first dropped to a minimum of 1091 C at a 1063 pulse, which is suspected to be the energy degradation due to the removal of dielectric erosion on the cathode surface [92]. The electric charge increased until the end after the arc discharge removed the

oxidation layer. The increment of the discharge after 1063 pulses could be explained by the reduction in the working pressure over time from 4.5×10^{-4} Pa to 3.8×10^{-4} Pa, as the material sputtered on the vacuum chamber walls would tend to absorb a certain amount of reactive gas during the deposition. The plasma ions either react with the nitrogen gas or simply incorporate the nitrogen atoms into the thin films [16]. The smaller pressure would allow a greater discharge since the energy barrier between the cathode and anode caused by the reactive gas was reduced. Therefore, less energy is consumed in the plasma emission process given in 1.7.2.4, which agrees with the prediction from previous work on reactive FCAD [93]. By the way, the overall change between the minimum and maximum data points is 23 C, above the standard error of 2.0 C. Therefore, the discharge increment effect over time is a reasonable factor to consider in reactive FCAD. However, the change is within 2% of the total discharge (~1100 C), which does not cause a significant effect on the deposition.

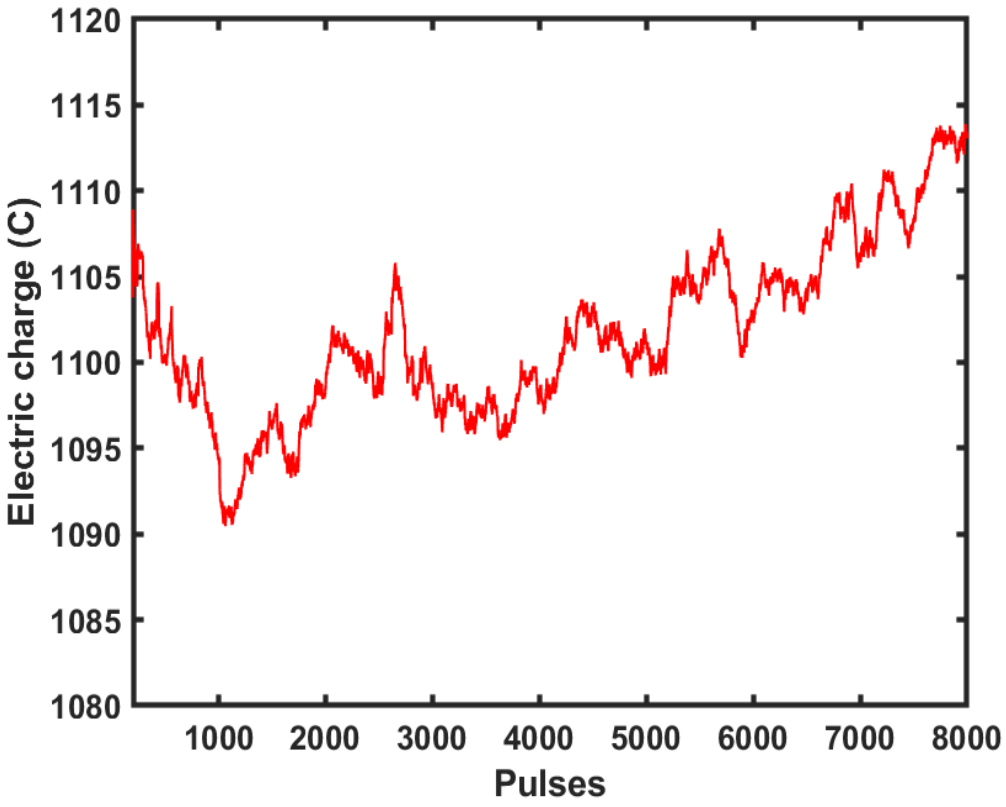

Figure 21 The variation of electric charge of the FCAD at R_N = 100%.

To further investigate the FCAD in a reactive gaseous environment, the average electric charge per pulse was obtained based on the oscilloscope recording. The average was taken for 8000 pulses for depositions at R_N of 5%, 10%, 20%, 50% and 100%. *Figure 22* shows the

average electric charge with the standard error at various R_N. The electric charge experienced a reduction of 4.5% from 1156 ± 5.6 C to 1106 ± 2.0 C as the nitrogen partial pressure increased, showing a smaller discharge at higher nitrogen concentrations. The result could be explained by the cathode poisoning caused by the dielectric nitridation layer formed on the surface. Cathode poisoning was known to have a significant impact on cathode spot ignition, especially in reactive FCAD [92]. The explosive process of cathode spot and ion bombardment heats up and melts the cathode surface, in which the nitrogen ions tend to form nitrides, particularly with the Al in our material. It consumes extra energy from the system to remove the dielectric cathode erosion by causing an electric breakdown for every cathode spot ignition. Therefore, it is expected to have a reduced discharge at high R_N. However, considering the overall change in electric charge is 50 C, which is less than 5% of the total charge, the effect on the deposition rate and thin film properties would be tiny.

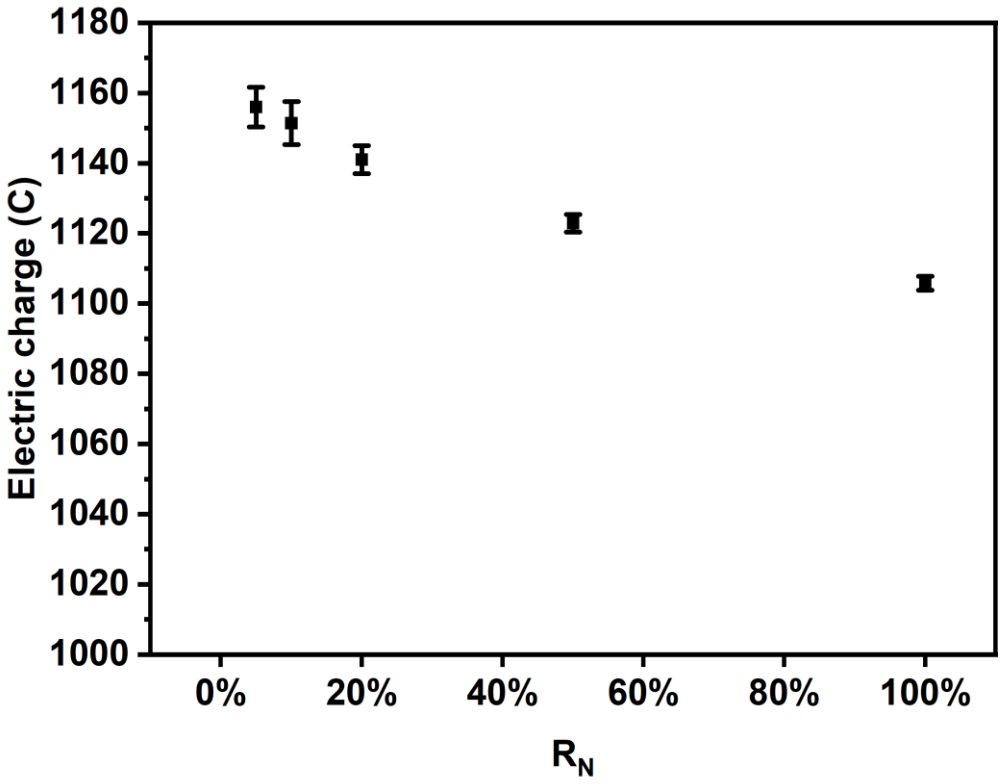

Figure 22 The average electric charge of FCAD pulses at various R_N.

3.2.3. Deposition rate

The deposition rates of the HEN thin films using the FCAD were calculated by the fraction

of the film thickness over the deposition time, in which the thickness was measured by the profilometer, as mentioned in 2.2.1. *Figure 23* shows the change in deposition rate in the five different nitrogen concentrations from 5% to 100% by averaging and calculating the step heights for 20 distinct points on the substrate. The error was caused by the uneven thickness of the surface at different locations since the plasma flow would be more concentrated at the centre of the substrate. The average deposition rate varied between 15.6 nm/min and 19.2 nm/min. Since the error bars of the data points all overlap, it is suspected that the variation of the deposition speed is negligible for different nitrogen environments. An independent two-sample T-test was conducted between R_N of 5% and 100% to confirm the observation using the thickness measurement of 20 distinct points at the step height for a two-tailed distribution and a two-sample unequal variance. The possibility that the two underlying populations have the same mean is 87%, which is unlikely to be a reduction.

The deposition rate of FCAD is mainly determined by the discharge current, the kinetic energy of ion flux, and the ion bombardment at the substrate [20]. The previous section shows that the discharge current is reduced slightly with increasing nitrogen concentration, so this effect is suspected to be limited. A loss in kinetic energy of ion flux in FCAD could be caused by the emission of charge-neutral particles and the ion collision with reactive gas [75]. In our case, the cathode material and initial capacitor voltage remained constant so that the amount of charge-neutral particles is suspected to be uniform. The chance of ion collision in a reactive FCAD depends on the quantity of reactive gas proportional to the working pressure [91]. Although the nitrogen partial pressure was changed, the overall working pressure was kept constant by the binary gas mixture. Therefore, the chance of ion collision with gas molecules during the deposition was maintained uniform. For comparison, the FCAD of $AlCrFeCoNiCu_{0.5}$ HEN thin films by Jiang *et al.* have obtained deposition rates that were reduced rapidly by applying pure nitrogen due to the large difference in the system pressure they have controlled throughout their depositions [94].

The ion bombardment at the substrate could influence the film thickness through backscattering and re-sputtering. Backscattering is defined as highly energetic ions reflecting from the substrate surface, and the self-sputtering effect is the ejection of the surface atoms from the film surface by the ion bombardment. An increment in ion flux or applying a negative

substrate bias tends to enlarge these effects and decrease the deposition rate, such as the HEA thin film deposited by Zhao *et al.* with multiple arc currents [19] and multiple substrate biases [65]. However, our experiment did not apply such a control, limiting the impact. The current result did not suggest that a disparity in nitrogen partial pressure in the FCAD of HEN thin films will significantly affect the deposition rate.

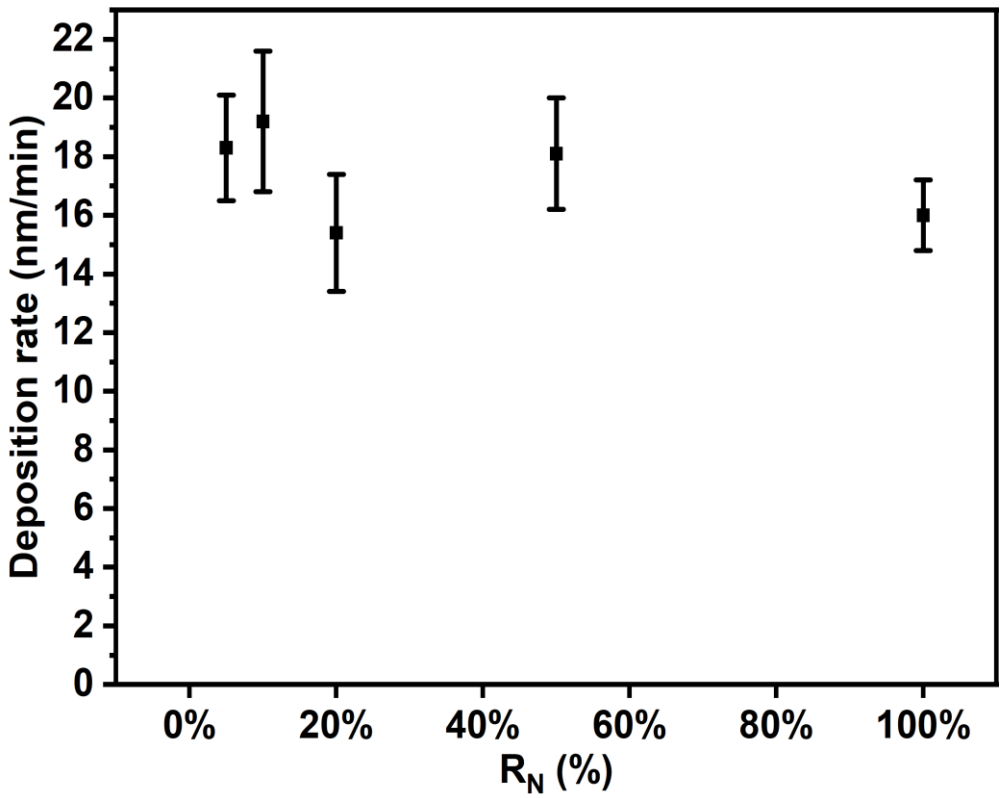

Figure 23 Deposition rate of $AlCrFeCoNiCu_{0.5}$ HEN Thin films deposited at various R_N.

3.3.Conclusion

In this chapter, HEN thin films were deposited by FCAD at various nitrogen partial pressure ratios. The deposition factors, including the pulse shape, the arc current and the deposition rate, are studied to provide a fundamental understanding of the reactive FCAD. The findings are given below:

i. Deposition pulses were selected between the shark-fin and the square shape. The average electric charge of the two pulse shapes is 978 C and 1162 C, respectively, which suggests an increase in charge per pulse by installing a speed-up capacitor in a reactive FCAD.

ii. Arc current per pulse shows no change at different stages in a deposition run of FCAD with pure nitrogen showing a stable deposition environment.

iii. The average electric charge was plotted against various R_N, which exhibited a smaller discharge at a higher nitrogen concentration. This result is explained by the nitrogen poisoning effect frequently occurring in a vacuum arc deposition with a gaseous environment. The reduction in charge was tiny compared to the total charge, so the effect on the deposition rate is expected to be weak.

iv. The deposition rate shows a small decline at R_N of 20% and 100%. By performing the Student T-test to the thickness measurement at R_N of 5% and 100%, the possibility of the two groups sharing the same mean is 87%, so the variation is insignificant. Although the R_N was changed at each deposition, the system pressure was kept constant. Therefore, the kinetic energy loss of ions due to particle collision was likely to be small. In conclusion, controlling the nitrogen concentration without changing the total pressure in a reactive FCAD does not cause a severe impact on the deposition rate.

Chapter 4

High entropy nitride thin films of $AlCrCoFeNiCu_{0.5}$ with controllable chemical composition and microstructure by regulating the nitrogen partial pressure

This chapter shows how the microstructure, composition, chemistry and hardness of the $AlCrFeCoNiCu_{0.5}$ HEN thin films deposited by filtered cathodic arc deposition (FCAD) were controlled by regulating the nitrogen partial pressure ratio R_N. The measurements were taken using the samples described in Chapter 3, deposited at various R_N from 5% to 100%. The details of the characterization techniques are described in 2.2.

4.1.Results and discussion

4.1.1. Thin film composition and chemistry

The chemical composition of $AlCrFeCoNiCu_{0.5}$ HEN thin films was obtained by scanning electron microscope and electron dispersive spectroscopy. The EDS mapping of each element at various R_N is shown in *Figure 24*. The EDS mappings show that the elements were well distributed on the film surface. Visual inspection shows no significant phase segregation at the surface of thin films at various R_N, demonstrating good adatom mobility at the surface during the deposition. The good mobility could be explained by both the energetic ion bombardment on the surface and the rapid cooling rate of the thin films due to the small thickness, known as the rapid quenching effect, which restricts the diffusion of the elements and prevents the formation of the intermetallic phases [12]. The surface oxygen-enriching layer caused the oxygen observed at the surface due to the post-deposition atmospheric reaction.

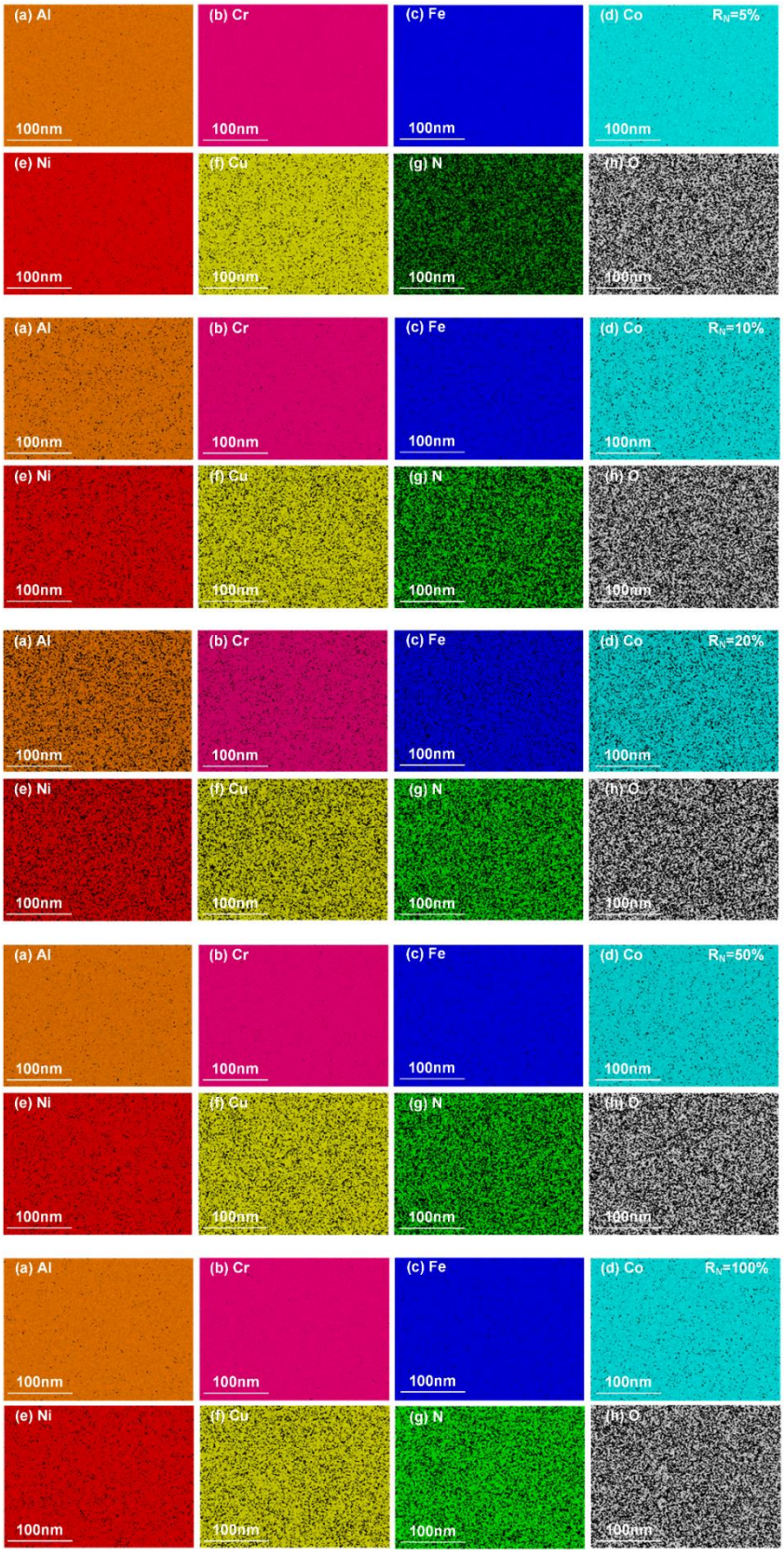

Figure 24 SEM-EDS mappings for (a) Al, (b) Cr, (c) Fe, (d) Co, (e) Ni, (f) Cu, (g) N, (h) O of thin film deposited at various R_N.

Table 5 reveals the atomic composition of the principal elements in the cathode for reference. The elemental composition of HEN thin films at R_N of 5%, 10%, 20%, 50%, and 100% is given in *Figure 25***.** The nitrogen concentration increased from 0.5 ± 0.1 at.% to 18.0 ± 1.6 at.%, at which R_N increased from 5% to 100%. [16]. The oxygen concentration was below 1% for all the HEN thin films. The atomic composition of Cr, Fe, Co, Ni, and Cu in the HEN thin films at various R_N was relatively close to the concentration in the cathode, while Al concentrations in all thin films were lower than that of the HEA cathode. By introducing gases, the working pressure was greater than general FCAD, leading to more ion collisions with gas molecules during the deposition. The lighter atoms, such as Al, were more likely to be filtered out in the duct due to their smaller mass, so the number of Al atoms arriving at the substrate was reduced. However, the reduction in ion kinetic energy due to the scattering in the duct also reduced the chance of preferential re-sputtering of Al at the substrate surface [95]. Therefore, the average Al concentration (13.2 at.%) in the HEN thin films was higher than the Al concentration (6 at.%) in $AlCrFeCoNiCu_{0.5}$ HEA thin films deposited by Zhao *et al.* [19]. The small reduction (5 at.% on average) of the metal composition was an outcome of the increasing nitrogen concentration as the nitrogen pressure increased.

Table 5 Composition of the $AlCrFeCoNiCu_{0.5}$ HEA cathode used for FCAD.

Elements	Al	Cr	Fe	Co	Ni	Cu
Atomic ratio (%)	18.2	18.2	18.2	18.2	18.2	9.1

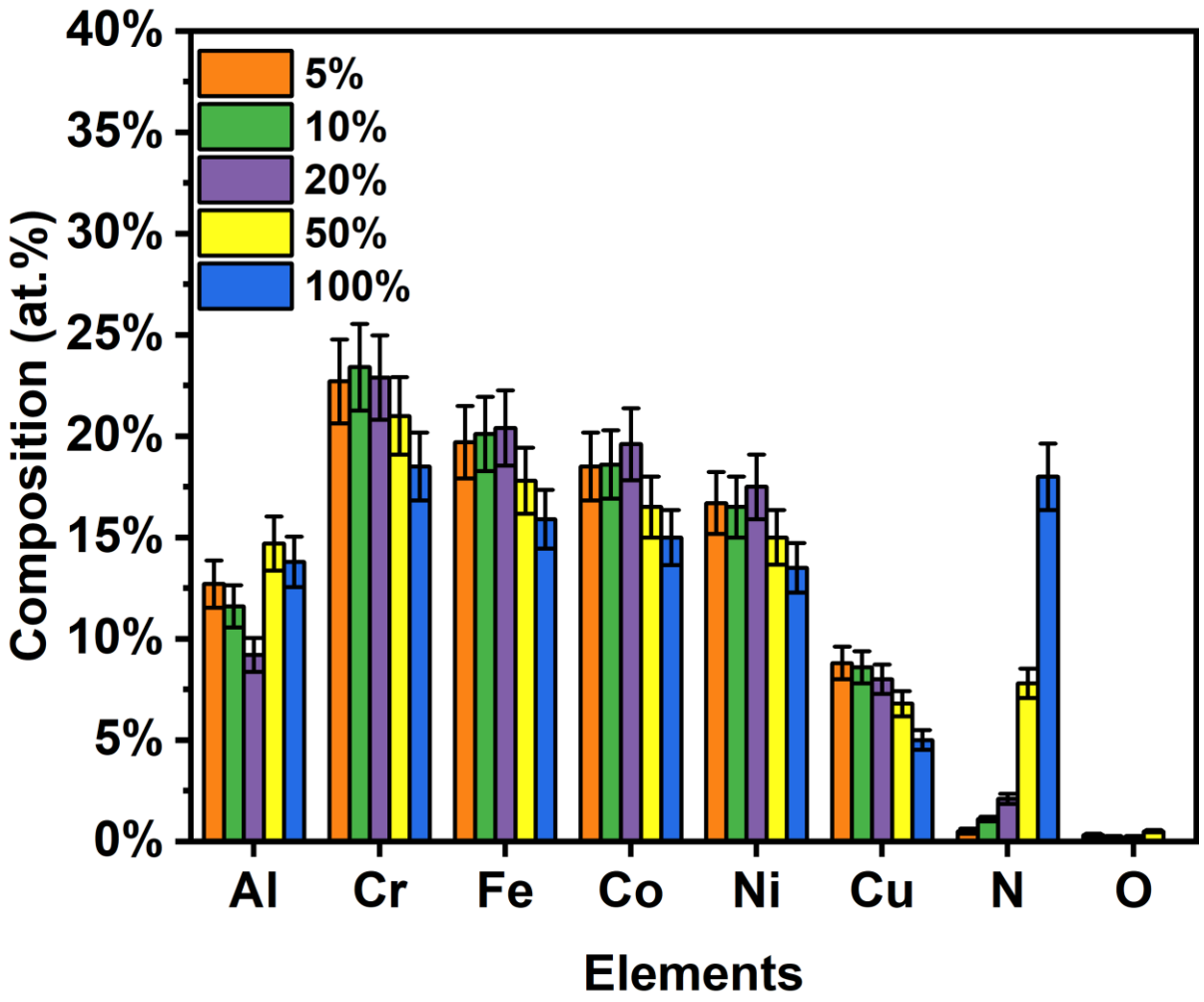

Figure 25 Elemental compositions of thin films in the atomic percentage of AlCr Fe CoNiCu$_{0.5}$ HEN thin films deposited at various R_N measured by SEM-EDS.

XPS was used to investigate the surface chemistry of AlCrFeCoNiCu$_{0.5}$ HEN thin films made by FCAD at various R_N. XPS survey spectra are displayed in *Figure 26*. High-resolution XPS spectra around the binding energy of the constituent metals at the surface of AlCrFeCoNiCu$_{0.5}$ HEN thin films are shown in *Figure 27*. The peaks around the metallic binding energy could show the binding state of each metal with the non-metal elements (e.g. N and O). The signal of Al_2O_3 and Cr_2O_3 was detected due to the oxide-enriching layer at the surface, as illustrated by EDS. The AlN and CrN signal was also detected at the surface, indicating the formation of the nitride precipitation at R_N above 50%. However, there is a chance that CrN at the surface was formed by the chemical vapour deposition (CVD) caused by the residual heat at the end of FCAD [96, 97]. Therefore, etching was performed to remove the surface layer and study the change in chemistry beneath the surface. Figure 28 shows the high-resolution XPS spectra of the present metals in AlCrFeCoNiCu$_{0.5}$ HEN thin films

deposited at various R_N after the 240 s etching. Metallic peaks for Al, Cr, Fe, Co, Ni and Cu were detected in HEN Thin films at various R_N. The small peaks at 711.5 eV and 712.6 eV in Fe_{2p} spectra contributed to the Cu/Co LM5 and Ni LM5, respectively [65]. No Al_2O_3, Cr_2O_3, and CrN peaks were detected after 240 S etching, implying that the oxide-enriching and the CrN layers formed at the surface have been removed.

Al_{2s} instead of the Al_{2p} pattern was used to avoid the potential impact of Cu_{3p} that might overlap with the Al/Al_2O_3 peak [98, 99]. The Al_{2s} spectra exhibited a peak due to the AlN at a binding energy of 118.6 eV. The pattern showed minor variation as the R_N increased from 5% to 20%. AlN peak was detected at R_N of 50% and overlapped with the metallic peak. At R_N of 100%, the AlN signal dominated, suggesting a full transition from the metallic bonds to the metal-nitrogen bonds. There was still nitrogen concentration measured in HEN thin films at R_N below 50% by the SEM-EDS (*Figure 25*), but since no AlN signal was observed at R_N under 50%, nitrogen atoms are suspected to be stored in the thin films without forming chemical bonds with Al. The detection of AlN also explains the uneven variation of Al concentration, which increased from 92 ± 0.8 at% to 15 ± 0.13 at% at R_N from 20% to 50%, given in *Figure 25*. Less preferential sputtering of Al atoms would occur at the substrate surface as more Al atoms were bonded to the nitrogen. The stronger interatomic force tends to hold the atoms more tightly to the substrate surface, preventing them from sputtering off the surface.

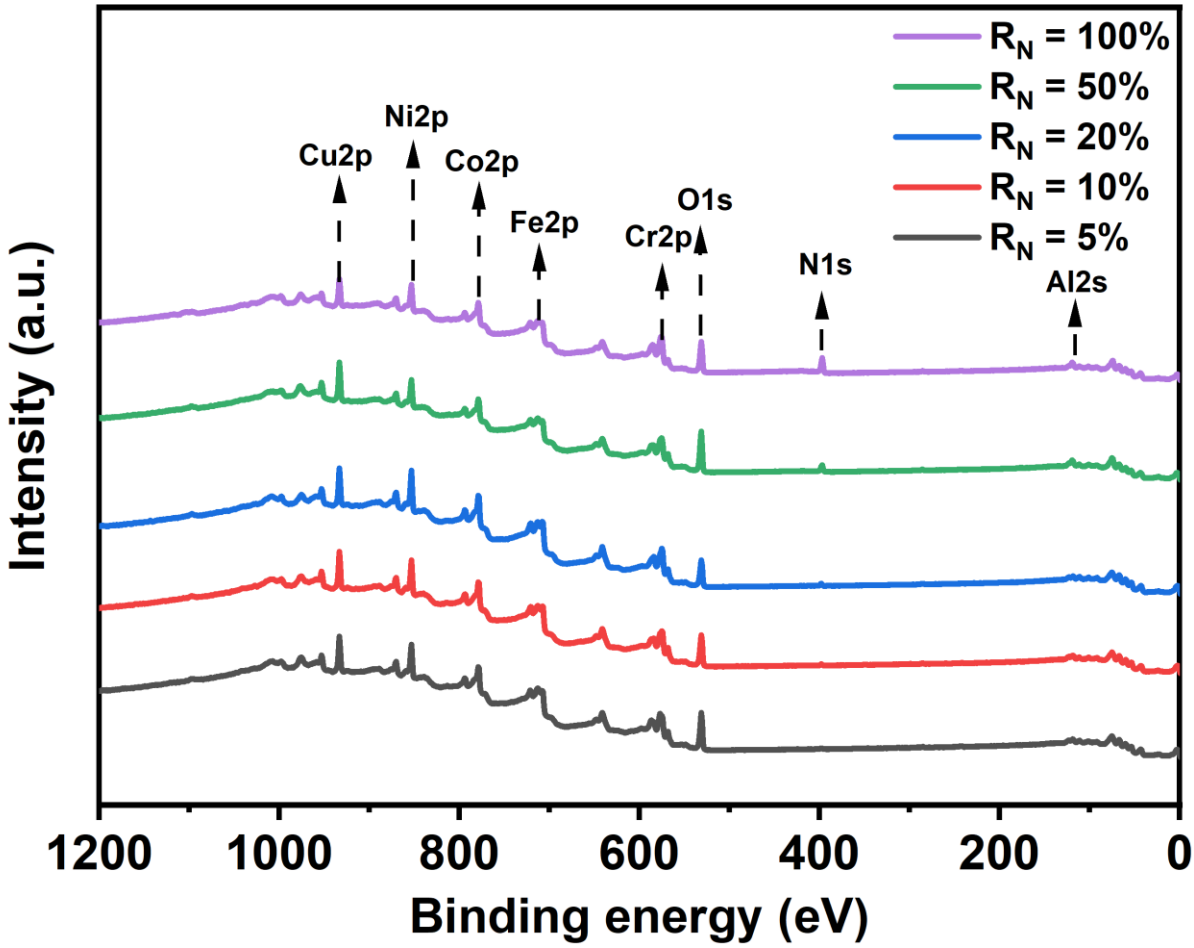

Figure 26 XPS survey spectra for $AlCrFeCoNiCu_{0.5}$ HEN thin films deposited at various R_N.

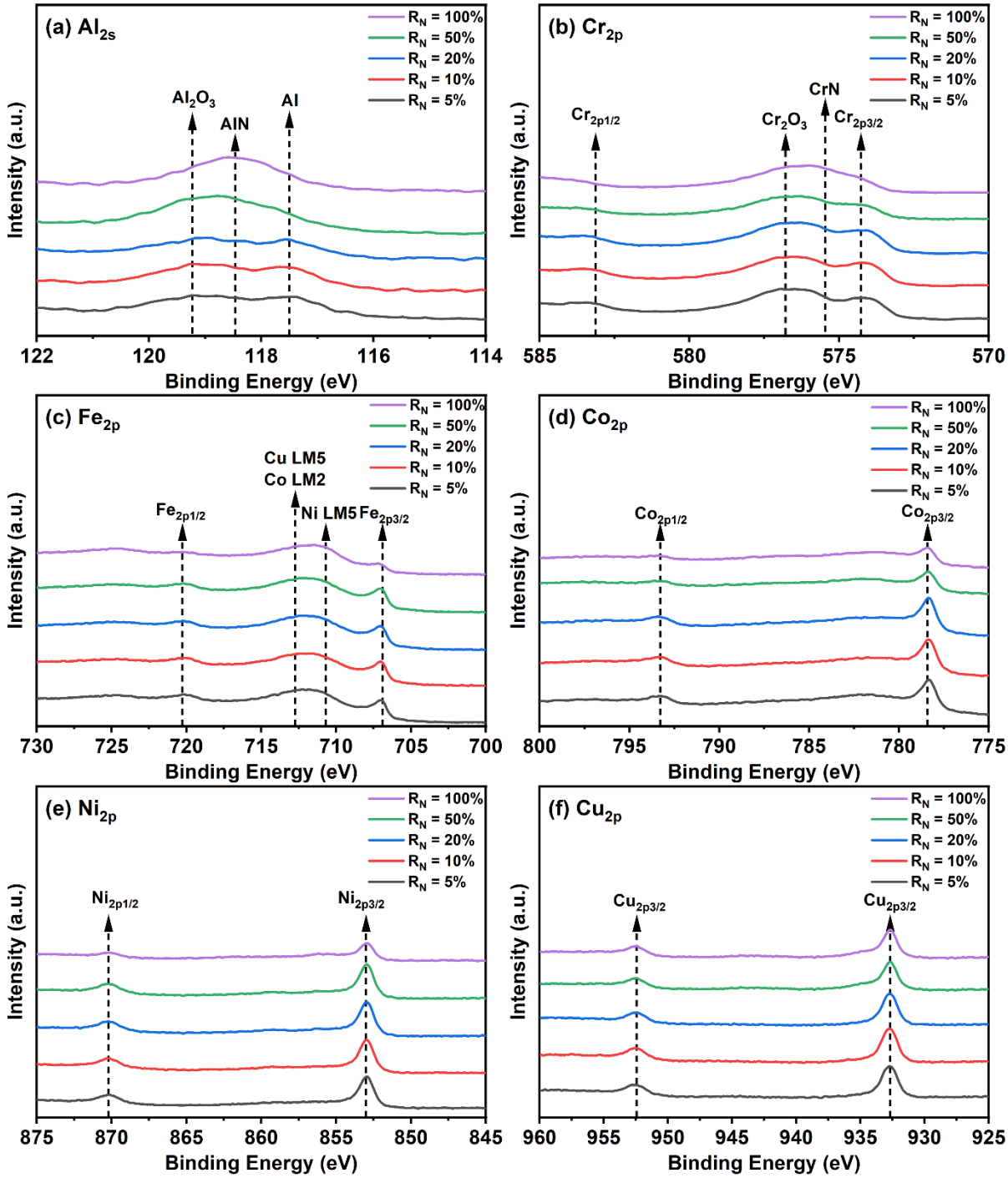

Figure 27 XPS surface spectra of (a) Al_{2s}, (b) Cr_{2p}, (c) Fe_{2p}, (d) Co_{2p}, (e) Ni_{2p}, and (f) Cu_{2p} of $AlCrFeCoNiCu_{0.5}$ HEN thin film deposited at various R_N.

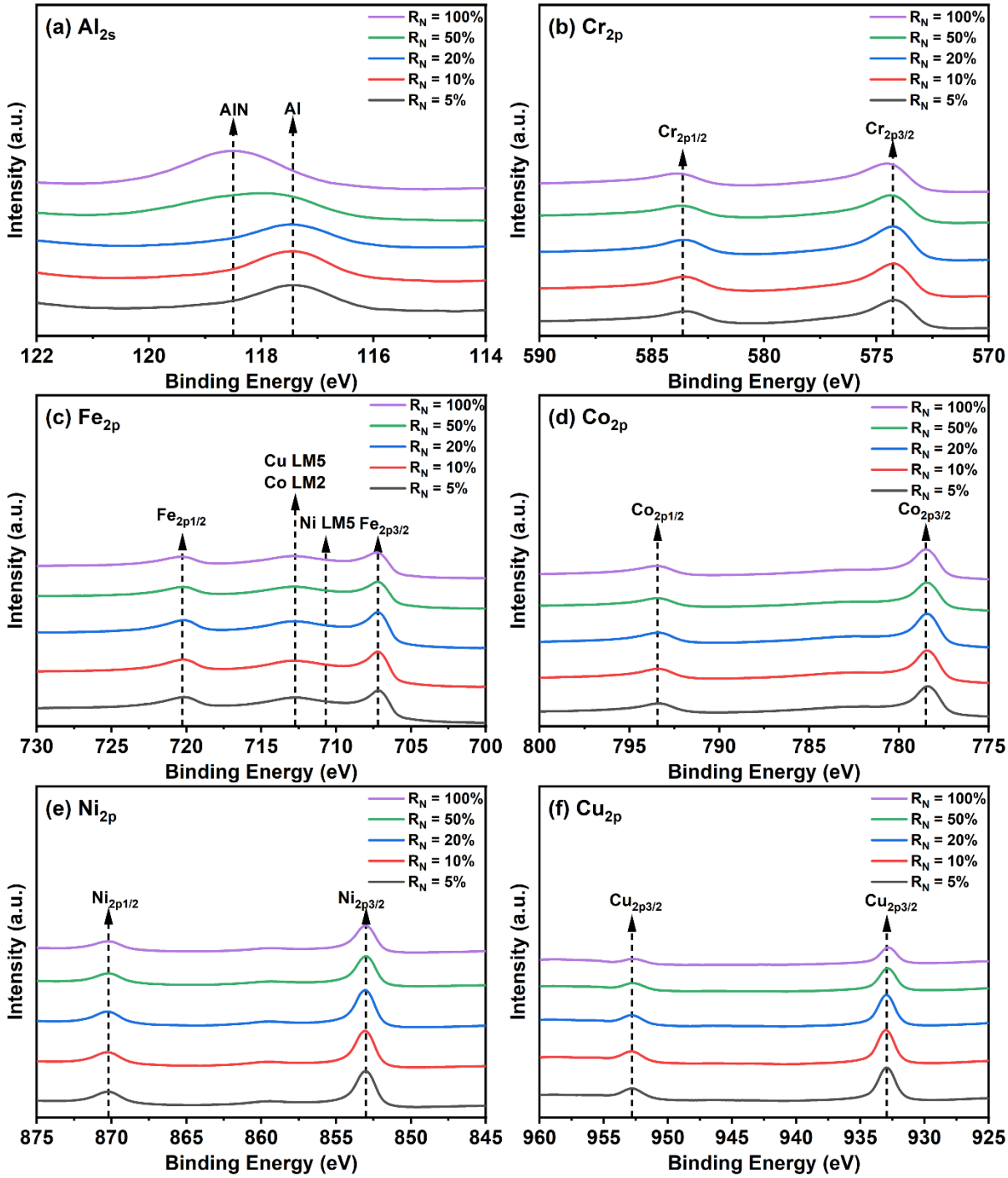

Figure 28 High-resolution XPS spectra after 240 s etching for (a) Al_{2s}, (b) Cr_{2p}, (c) Fe_{2p}, (d) Co_{2p}, (e) Ni_{2p}, and (f) Cu_{2p} of HEN thin films deposited at various R_N.

Only the metallic peaks were detected in Cr_{2p}, Fe_{2p}, Co_{2p}, Cu_{2p}, and Ni_{2p} by XPS, which suggests that they are unlikely to form metal-nitrogen bindings and remain in the metallic phase underneath the surface [16]. The preference for nitride formation is referred to as the standard enthalpy of formation for each metal, as listed in Table 6. The low reactivity of Fe, Co, Cu, and Ni was most likely due to the higher standard enthalpy of formation. Thermodynamically, Al and Cr are favourable for the formation of nitrides due to the negative standard enthalpy of formation. At the same time, Fe, Co, Ni, and Cu tend to remain in a metallic phase in our thin films, as shown in previous works [16, 54]. However, no CrN or Cr2N signal was detected in the film after 240 s etching at any nitrogen partial pressure, implying that there were not many chromium nitrides underneath the surface of the thin films. AlN formation was favoured beneath the surface, which could be explained by the larger tendency of valence electron donation of Al atoms than Cr atoms to achieve the noble gas electron configuration [100]. The observation that the CrN formation was less favourable agrees with the HEN thin films deposited by Jiang *et al.* at various working pressures [94]. The difference is that the working pressure was kept constant in our work, leading to a relatively smaller variation in ion kinetic energy for ion bombardment of the substrate. Therefore, the variation in adatom mobility on the thin film tends to be smaller, resulting in less nitrogen diffusion and CrN detection underneath the surface.

Table 6 Standard enthalpy of formation, ΔH_f (kJ/mol) for selected binary nitrides of constituent metals at 298 K [7, 44, 101, 102].

Compound	ΔH_f (kJ/mol)
AlN	-317.98
CrN	-117.15
Cr_2N	-125.52
Fe_4N	-10.46
Fe_2N	+12.60
Co_2N	+8.40
Cu_3N	+74.50
Ni_3N	N/A

4.1.2. Microstructure

The crystallographic structure of HEN thin films was investigated by XRD. *Figure 29* illustrates the XRD patterns of thin films and the substrate for 2θ from 20° to 90°. The minor peaks indexed as SiO_2 and Si are due to XRD penetration onto the substrate [103]. The peak of an $AlCrCoFeNiCu_{0.5}$ system located at 43.4° demonstrates the FCC phase [104, 105]. A single FCC phase formed due to a relatively lower Al composition (approximately 12% on average). It was reported that an FCC structure was favoured in an AlCrCoFeNiCu0.5 thin film if the Al composition was lower than 10 at% [65, 90, 106].

The intensity of FCC (111) peaks reduced, and the full width at half maximum (FWHM) increased as R_N increased, suggesting a reduction in grain size and amorphization. This effect became significant at R_N of 50%, and no FCC peak was exhibited at R_N of 100%. This observation was likely due to the transformation of the crystal from a nanocrystalline structure to an amorphous structure. The HEN thin films deposited by Jiang *et al.* showed a similar nitrogen concentration ranging from 4.3 at% to 21.2 at%, and their HRTEM revealed a transformation from a single FCC structure to a fully amorphized structure, with a dual-phase at a moderate nitrogen concentration [53]. The mechanism of the crystal transformation is suspected to be a decrease in Gibbs free energy of the HEA solid solution system. When the nitrogen atoms are incorporated into HEA, they are suspected to act as a seventh element of the solid solution by occupying interstitial sites [107, 108]. The smaller atomic size introduces more disturbance to the crystal, enhances the lattice distortion, and eventually ends up with an amorphization.

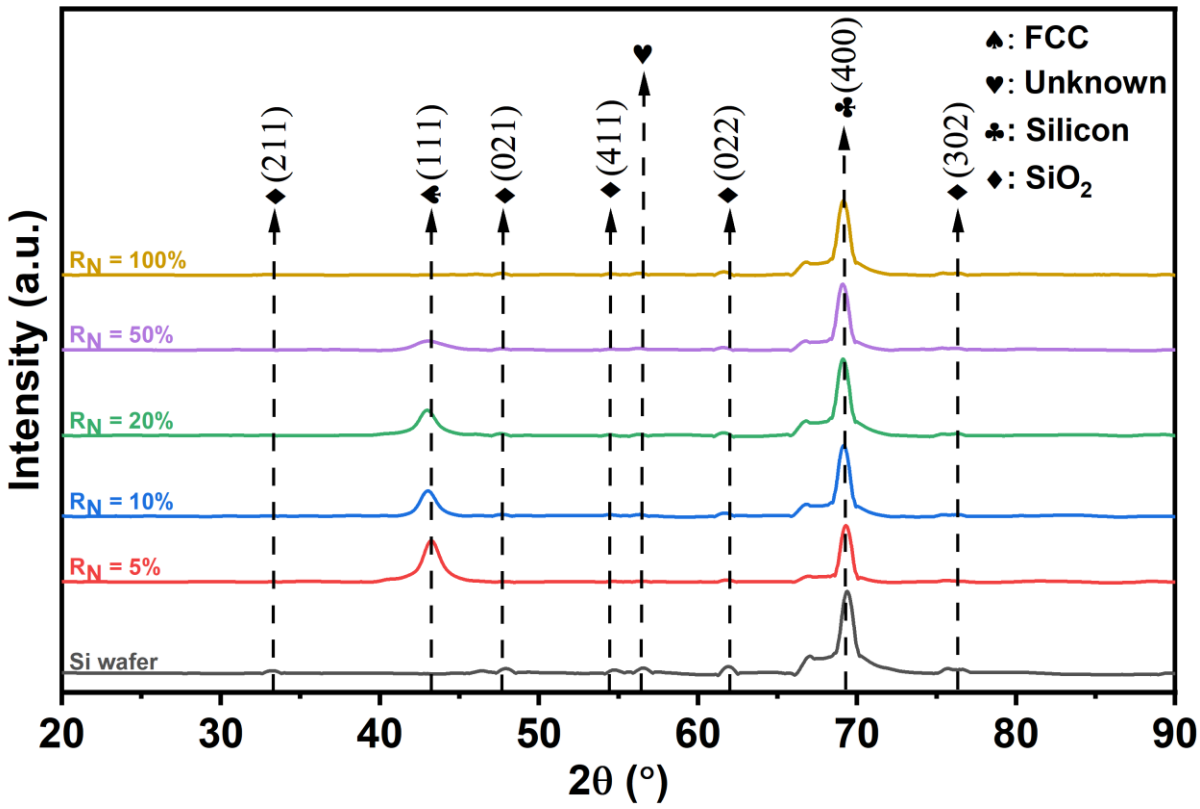

Figure 29 XRD patterns of $AlCrFeCoCu_{0.5}$ HEN thin films deposited at various R_N.

The lattice parameters based on XRD patterns are listed in Table 7. The left shift of the FCC (111) peak is due to a lattice parameter change. It first increased slightly from 3.623 Å to 3.643 Å for HEN thin films deposited at R_N from 5% to 20%, respectively. The interstitial nitrogen expanded the unit cell of the lattice, further demonstrating the severe lattice distortion effect [109]. The lattice parameter then dropped to 3.635 Å at R_N of 50%, the point at which AlN bonds were detected beneath the film. The strong covalent binding of AlN causes the lattice to shrink, which reduces the lattice parameter.

Table 7 Lattice parameters of FCC phase in HEN thin films deposited at various R_N.

R_N (%)	2θ (°)	Lattice parameter (Å)
5	43.217	3.623
10	43.006	3.640
20	42.964	3.643
50	43.057	3.635
100	N/A	N/A

4.1.3. Hardness

The correlation between the microstructure and mechanical properties of the HEN thin films was investigated by performing nanoindentation. *Figure 30* shows the hardness of HEN thin films deposited at different R_N. It is observed that the hardness increased rapidly as R_N increased. The hardness increment from 7.8 ± 0.1 GPa to 8.8 ± 0.1 GPa between R_N of 5% and 20% could be explained by the solid solution strengthening. SEM-EDS and XPS show that nitrogen atoms were stored in the HEN thin film without forming nitrides. XRD shows that the nitrogen atoms occupy interstitial sites in the crystal lattice and cause a lattice expansion at R_N from 5% to 20% (Table 7). A severe lattice distortion was exhibited due to the significantly smaller atomic size of nitrogen atoms than the metallic atoms in the $AlCrFeCoNiCu_{0.5}$ system, resulting in a higher internal strain, restricting the dislocation [110]. Moreover, the XRD pattern transformed from a simple FCC phase to an amorphous structure, which provides further evidence for solid solution strengthening [111].

The hardness increment at R_N from 20% to 50% contributed to both the nitride formation and the transition of the crystal structure. The introduction of AlN is revealed by XPS patterns for R_N above 20%. The stronger covalent bonding provides extra interatomic force, which further restricts the atomic rearrangement and deformation, and leads to the increase in hardness [112]. There was only a slight increase in hardness from R_N of 50% to 100% (0.1GPa), even though the AlN signal is at its maximum at R_N of 100%. This observation could be explained by the transition to the amorphous phase, so the strengthening due to the lattice distortion was weakened, balancing out the effect of AlN precipitation. The maximum hardness of 9.6 ± 0.1 GPa at R_N of 100% is consistent with the $AlCrFeCoNiCu_{0.5}$ HEN thin film deposited by Khan *et al.*, in which they achieved a maximum hardness of 9.8 GPa with a nitrogen concentration of 10.6 at.% using RF magnetron sputtering [7].

For comparison, Zhao *et al.* deposited the HEA thin films of $AlCrFeCoNiCu_{0.5}$ by FCAD and achieved a maximum hardness of 7 GPa, which is below the hardness of 7.8 GPa at R_N of 5% [19]. The HEN thin films achieve a higher hardness than HEA at R_N above 50%, can be due to the larger interatomic force caused by the stronger covalent bonding of AlN precipitates in compare to the metallic bonding, impedes the atomic deformation. Another factor that

enhances the hardness of HEN can be the interstitial solid solution structure. The nitrogen atoms that occupy the specific interstitial sites, enlarge the effect of lattice distortion due to their significantly smaller size, which further restrict the formation of dislocations and lattice movement. Moreover, at maximum R_N, the hardness improvement of HEN can also be due to the full transition to an amorphous phase. The result generally suggests that increasing the nitrogen partial pressure in FCAD could generate HEN thin films with superior hardness than the corresponding HEA thin films.

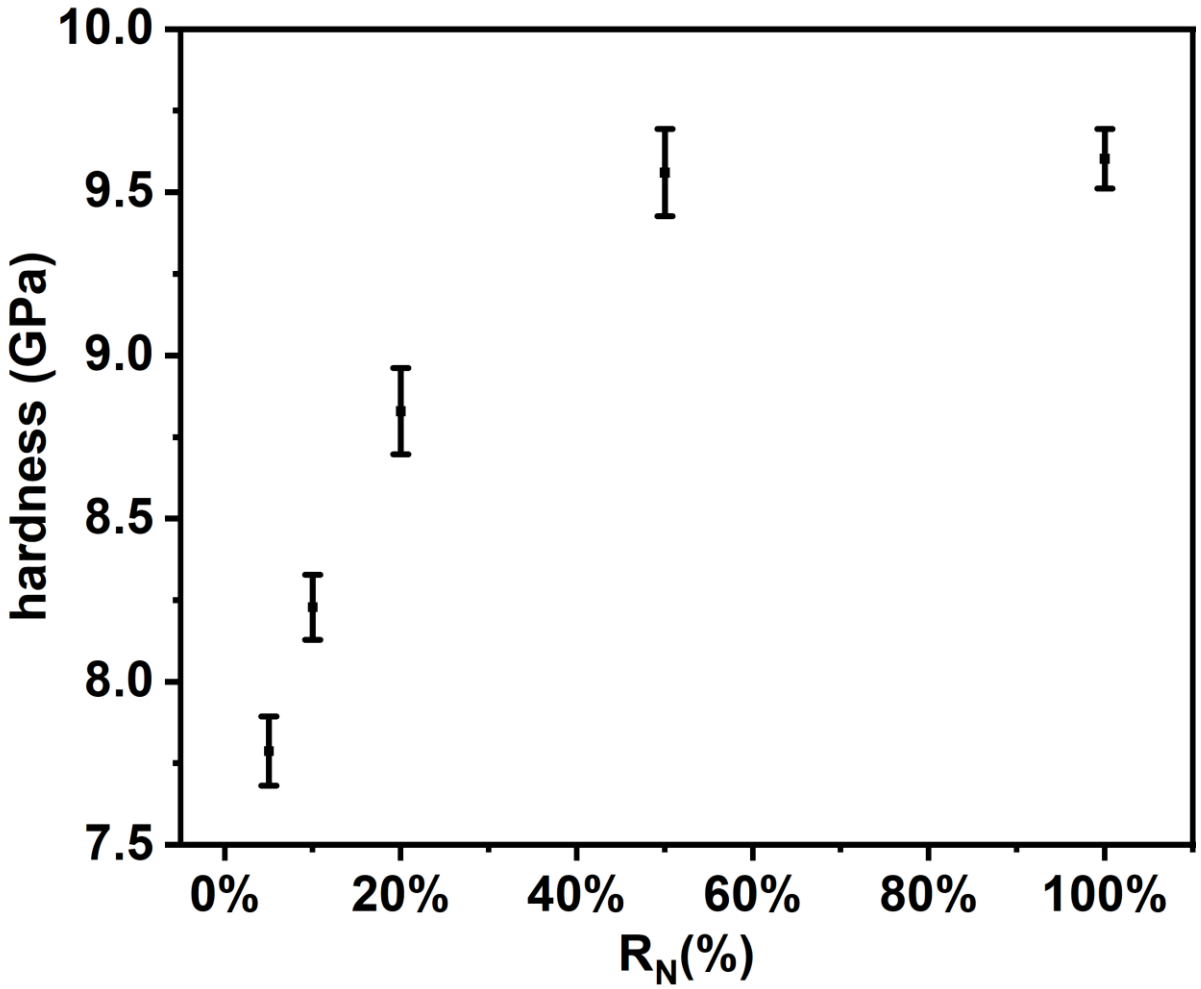

Figure 30 Hardness of $AlCoCrCu_{0.5}FeNi$ HEN thin films deposited at various R_N.

4.1.4. Surface morphology

The surface morphology and roughness of HEN thin films at various R_N measured by AFM are given in *Figure 31*. The surface RMS roughness decreased from 0.51 to 0.37 nm at R_N from 5% to 100%. The roughness reduction at R_N from 5% to 50% was likely due to the reduction

in grain size illustrated by the FWHM increment of FCC peak in XRD. The smaller grain size of HEA thin films tends to reduce the surface deformation and the voids between them [34, 113]. The reduction of roughness from 0.37 to 0.29 nm at R_N from 50% to 100% could be further explained by the crystal transition from the single FCC structure to the amorphous structure revealed by XRD, the phase transition would lead to isotropy [114].

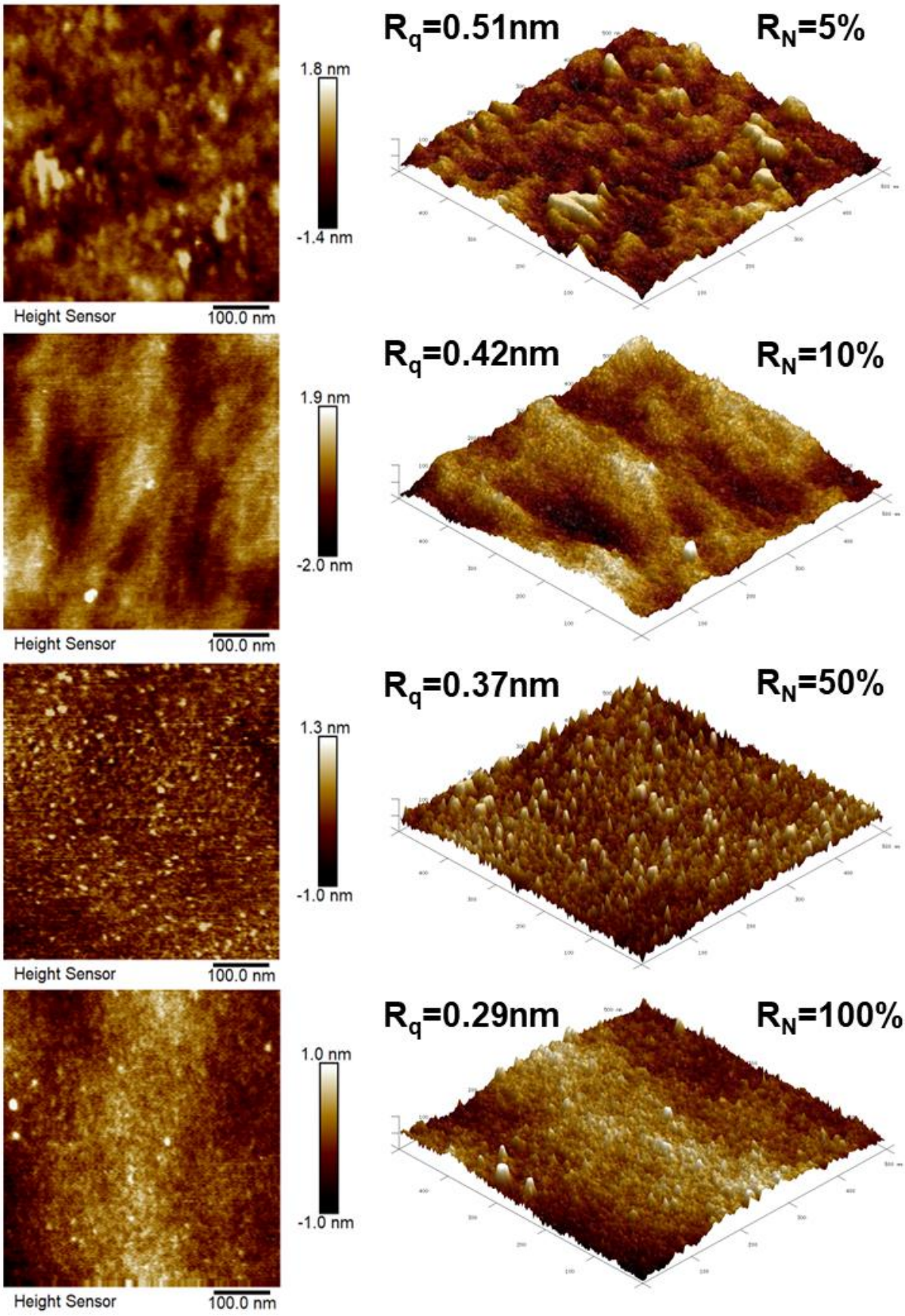

Figure 31 AFM images for film surface roughness of $AlCrFeCoNiCu_{0.5}$ nitride thin films at various R_N; surface roughness R_q was provided in the centre of the image.

4.2.Conclusion

In conclusion, a new method to fabricate $AlCrFeCoNiCu_{0.5}$ nitride thin films by FCAD on silicon substrates was developed where the chemistry and microstructure of the film were controlled by changing the nitrogen partial pressure ratio in a nitrogen and argon gas filling gas maintained at constant pressure. The composition, surface chemistry, microstructure, hardness, and surface morphology of HEN thin films were investigated, and the major outcomes are listed below.

i. The elements of HEN thin films were uniformly distributed at the surface, as illustrated by the EDS maps, exhibiting good homogeneity. The absence of phase segregation at the surface could be explained by the good adatom mobility of FCAD and the rapid quenching effect.

ii. EDS composition analysis indicated a rapid increment of nitrogen concentration as R_N increased. The Al concentration is below the atomic ratio of that of the cathode material due to the interaction between ion loss, re-sputtering, and backscattering effects. The Al increases above R_N of 50% could be explained by the AlN precipitation, which enhances the interatomic force of Al and restricts the re-sputtering.

iii. XPS revealed the existence of CrN and AlN at the surface of the thin films deposited at high R_N, while the Fe, Co, Ni, and Cu remained in the metallic phase because of their higher enthalpy of formation. XPS after 240 s etching suggested that the CrN only exists at the surface due to the CVD effect, and the AlN is the only nitride beneath the surface due to its extraordinarily lower enthalpy of formation.

iv. The microstructure of thin films was revealed by XRD, which demonstrated a transformation in the crystal structure from a single FCC phase to an amorphous phase at high nitrogen composition. A reduction in grain size and an expansion of lattice parameters have been observed due to the nitrogen occupying the interstitial sites, causing a lattice distortion.

v. The hardness has increased to a maximum of 9.6 ± 0.1 GPa at R_N of 50%, and no significant variation was observed above R_N of 50%. The performance improvement is due to the solid solution strengthening of interstitial nitrogen and the strong

interatomic force brought by binary nitrides. The average hardness is about 23% greater than the HEA thin films with the same constitutional metals.

vi. The surface roughness was reduced to a minimum of 0.29 nm as the R_N increased to 100%, which could be explained by both the grain size reduction and the transition from the FCC phase to the amorphous phase.

4.3.Recommendations

The deposition condition, chemistry, microstructure, and hardness of $AlCrFeCoNiCu_{0.5}$ HEN thin films were crucially investigated in this thesis, providing insights into the HEN thin film fabrication by FCAD at different nitrogen partial pressures. However, the multicomponent alloy nitride is a highly complex system, with variable compositions and crystal phases. For these materials to be ready for industrial applications, it is essential to further study the HEN thin films at various R_N in terms of the composition and phases transition by various techniques, as well as the change in performance related properties. Moreover, the effect of other fabrication-related parameters, such as substrate temperature, substrate bias and substrate material, is worth investigating. Future works could be built on the findings in this thesis to promote deeper insight into the HEN thin film fabrication, characteristics and potential uses. Some possible research in the future is listed below:

4.3.1. Transmission electron microscopy (TEM)

TEM could be performed to investigate the composition and microstructure of the $AlCrFeCoNiCu_{0.5}$ HEN thin films further in two different ways. High resolution transmission electron microscopy (HRTEM) could be used to analyse the crystallinity of the sample, and scanning transmission electron microscopy - energy dispersive x-ray spectroscopy (STEM-EDS) installed in TEM could be used to map the cross-sectional chemical composition of the thin films. TEM is a powerful analytical instrument that could provide microstructure information, such as phase transformation and defect formation, with very high resolution (below 1 nm). *Figure 32* shows the microscope components and arrangement. It is set up in a columnar structure under a high vacuum, in which an electron gun emits an electron beam

(~100 – 300 KV) down the column onto the specimen focused by an electromagnetic condenser lens. The electron beam is scattered from a small volume within the sample surface to create an electron diffraction pattern (EDP) on a phosphor screen. The technique requires the specimens to be extremely thin (< 100 nm) so a significant fraction of the electrons can pass through. This requires the thin films to be polished to reduce their thickness before examination.

The EDP provides microstructure information by representing the atoms as bright dots on the screen after constructive interference. The regularly spaced atoms act as diffraction gratings. The interaction satisfies Bragg's law (Equation 5), and by combining it with the geometric relationship of TEM, the spacing of the crystal layers could be determined, contributing to the lattice parameters [115]. The diffraction pattern shows sharp diffraction rings for a polycrystalline sample, whereas an amorphous specimen forms diffuse rings, which could help show the FCC to amorphous phase transition in HENs. Moreover, by choosing the appropriate aperture settings, bright field images showing a visual image of the crystallographic orientation could also be created. Therefore, the microstructure information such as the grain boundary and grain size could be determined by processing the bright field images, further confirming the result of XRD.

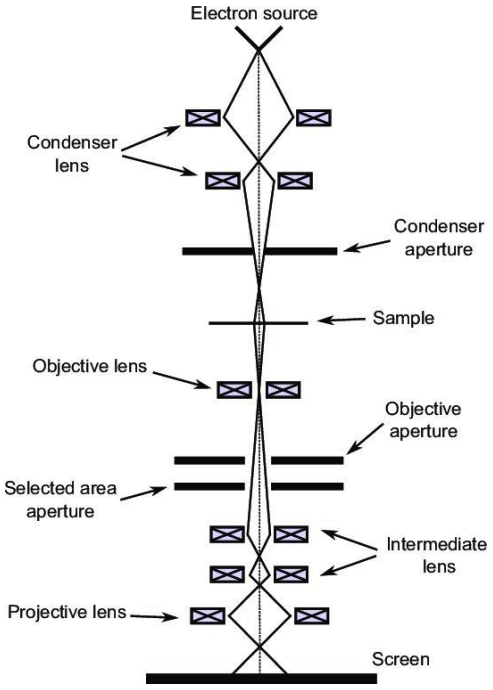

Figure 32 Schematic representation of TEM showing the orientation of various components and lenses, outlining the imaging system [116].

4.3.2. Contact angle measurement

The wetting performance of a surface material is critical for protective coatings. The contact angle (CA) of a water droplet on the surface could give a quantitative investigation of the wetting behaviour. CA is defined as the internal angle between the surface and the water droplet at the contact line. The size of CA defines the wettability where CA > 90˚ is referred to as hydrophobic, and CA < 90˚ is considered hydrophilic [117]. Surfaces with CA > 150˚ are considered superhydrophobic, which is extremely small wettability. The CA measurements is performed based on Young's equation as follows:

$$\gamma_{SV} = \gamma_{SL} + \gamma_{LV} cos\theta \quad (12)$$

Where γ represents the tension at the surface-water-vapour interface; θ is the CA between the water droplet and the solid surface. The schematic representation is illustrated in *Figure 33*.

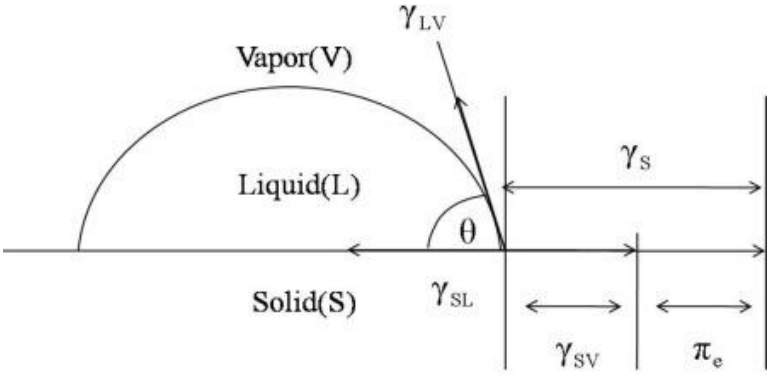

Figure 33 Schematic representation of the contact angle (CA) of a liquid droplet on a solid surface [118].

4.3.3. Electrical resistivity

Since the $AlCrFeCoNiCu_{0.5}$ HEN thin films are recommended as protective coatings, electrical resistance is critical for applications requiring electrical insulation. A four-point probe method is frequently used to measure the electrical resistance of samples with small dimensions, particularly in the form of thin films. *Figure 34* illustrates the schematic representation of a four-point probe on a sample with dimensions of A (length), D (width) and W (thickness). The probe consists of four equally spaced metal pins contacting the surface. A high impedance power source is applied to supply current to the two outer pins measured by an ammeter (I), and a voltmeter (V) is connected to the inner pins to measure the voltage in between. The

resistivity could be calculated by the following equation:

$$\rho = RA/L \tag{13}$$

Where ρ is the electrical resistivity of the thin film; R is the measured resistance; A is the width × thickness of the thin film, and L is the measured distance between the two probes.

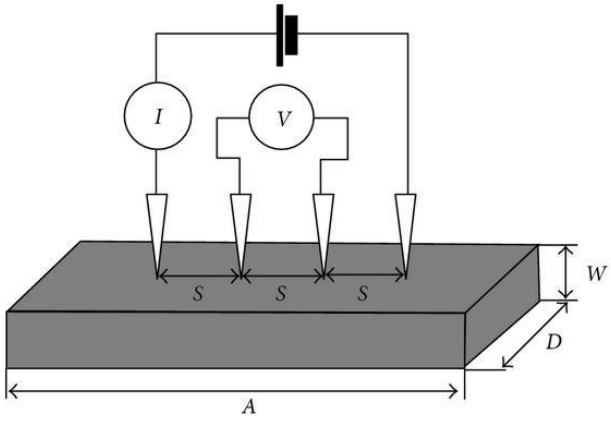

Figure 34 Schematic representation of a four-point probe method to measure electrical resistance on a surface [119].

4.3.4. Fabrication variables

The fabrication process by FCAD will substantially influence the characteristics and improve the physical properties of the HEN thin films. The synthesis procedure could be further explored by varying the deposition parameters to optimise the performance of these materials for potential applications. The effect of various fabrication-related aspects, which could be investigated in the future, is listed below:

Substrate bias

Substrate bias is a critical parameter to adjust the kinetic energy of ions travelling toward the substrate. By creating a negative bias onto the substrate holder, ions can experience differential acceleration based on their charge state [20]. The increased kinetic energy of ions enhances the heat accumulation effect on the substrate surface, which improves the adatom mobility that is highly related to the phase transformation and homogeneity of the thin films. For example, larger grain size could be obtained as the number of nucleation sites is decreased by the higher mobility of adatoms [120]. It has been reported that the negative substrate bias

could cause a sufficient impact on the thin film microstructure and the adhesion force at the interface between the substrate and the thin film deposited by FCAD [65, 121]. The preferential sputtering of light elements such as Al in the $AlCrFeCoNiCu_{0.5}$ system could be enhanced by the larger kinetic energy, which alters the composition of the thin film. The variation of light element concentration could possibly change the crystal structure and lattice distortion due to large atomic size differences, which might provide enhanced properties. The deposition rate could also be varied by applying a substrate bias, since the backscattering and re-sputtering effect are depending on the ion energy. Therefore, it is worth to study the effect of tuning the substrate bias on the fabrication of HEN thin films.

Substrate temperature

The temperature of the substrate is another critical factor that could impact the homogeneity, microstructure and properties of the HEA thin films during the deposition. Research shows that the change in substrate temperature can cause variation in aspects such as film growth rate, grain formation, phase formation, surface diffusion and interface adhesion force, which are highly relevant to the physical performance [76]. Increasing the substrate temperature could enhance adatom mobility so that atomic diffusion occurs more frequently, resulting in a more homogenous composition, better crystallization degree and rapid phase transition [122]. Increased adatom mobility might also favour a higher nucleation rate, giving larger grains and improved structure integrity [123]. Therefore, changing the substrate temperature during the deposition could be a potential option to improve the quality of $AlCrFeCoNiCu_{0.5}$ HEN thin films by FCAD.

Different substrates

The substrate material used for deposition can have a crucial impact on the quality of the HEN thin films. The choice of substrate material influences a series of thin film-related aspects, such as adhesion force, interfacial diffusion, internal tension and crystal orientation, which are highly linked to the thin film performance and durability. Most research at the current stage focuses on HEN thin film deposition on the surface of Si or Al_2O_3 wafer [112]. These surfaces are usually not the case in the real-world application. Substrates can cause numerous effects on thin films based on their distinct properties. The detects and roughness of the substrate surface can affect the nucleation mechanism and hence influence grain formation. The substrate's

density and chemical reactivity impact the atomic diffusion at the interface and the adhesion strength. A change in the thermal expansion coefficient of the substrate could also result in a variation in film stress, which directly affects the mechanical properties of the thin film. Therefore, studying the $AlCrFeCoNiCu_{0.5}$ HEN thin film deposition on the surface of commercially used materials such as 304 stainless steel would be a potential opposition.

Reference

[1] J. W. Yeh *et al.*, "Nanostructured high-entropy alloys with multiple principal elements: Novel alloy design concepts and outcomes," *Advanced Engineering Materials,* vol. 6, no. 5, pp. 299-303, May 2004, doi: 10.1002/adem.200300567.

[2] O. N. Senkov, J. M. Scott, S. V. Senkova, F. Meisenkothen, D. B. Miracle, and C. F. Woodward, "Microstructure and elevated temperature properties of a refractory TaNbHfZrTi alloy," *Journal of Materials Science,* vol. 47, no. 9, pp. 4062-4074, May 2012, doi: 10.1007/s10853-012-6260-2.

[3] O. N. Senkov, G. B. Wilks, D. B. Miracle, C. P. Chuang, and P. K. Liaw, "Refractory high-entropy alloys," *Intermetallics,* vol. 18, no. 9, pp. 1758-1765, Sep 2010, doi: 10.1016/j.intermet.2010.05.014.

[4] C. L. Liu *et al.*, "Comparison of 16S rRNA gene PCR and blood culture for diagnosis of neonatal sepsis," *Archives De Pediatrie,* vol. 21, no. 2, pp. 162-169, Feb 2014, doi: 10.1016/j.arcped.2013.11.015.

[5] S. Y. Yen, Y. C. Liu, S. H. Chu, C. W. Chang, S. K. Lin, and M. H. Tsai, "B2-strengthened Al-Co-Cr-Fe-Ni high entropy alloy with high ductility," *Materials Letters,* vol. 325, Oct 2022, Art no. 132828, doi: 10.1016/j.matlet.2022.132828.

[6] Y. Y. Chen, T. Duval, U. D. Hung, J. W. Yeh, and H. C. Shih, "Microstructure and electrochemical properties of high entropy alloys - a comparison with type-304 stainless steel," *Corrosion Science,* vol. 47, no. 9, pp. 2257-2279, Sep 2005, doi: 10.1016/j.corsci.2004.11.008.

[7] N. A. Khan *et al.*, "High entropy nitride (HEN) thin films of AlCoCrCu0.5FeNi deposited by reactive magnetron sputtering," *Surface & Coatings Technology,* vol. 402, Nov 2020, Art no. 126327, doi: 10.1016/j.surfcoat.2020.126327.

[8] C. J. Tong *et al.*, "Microstructure characterization of AlxCoCrCuFeNi high-entropy alloy system with multiprincipal elements," *Metallurgical and Materials Transactions a-Physical Metallurgy and Materials Science,* vol. 36A, no. 4, pp. 881-893, Apr 2005, doi: 10.1007/s11661-005-0283-0.

[9] S. Varalakshmi, M. Kamaraj, and B. S. Murty, "Formation and Stability of Equiatomic and Nonequiatomic Nanocrystalline CuNiCoZnAlTi High-Entropy Alloys by Mechanical Alloying," *Metallurgical and Materials Transactions a-Physical Metallurgy and Materials Science,* vol. 41A, no. 10, pp. 2703-2709, Oct 2010, doi: 10.1007/s11661-010-0344-x.

[10] J.-W. Y. B.S. Murty, S. Ranganathan, P. P. Bhattacharjee, *High-Entropy Alloys*, 2 ed. Elsevier, 2019.

[11] D. B. Miracle and O. N. Senkov, "A critical review of high entropy alloys and related concepts," *Acta Materialia,* vol. 122, pp. 448-511, 2017/01/01/ 2017, doi: https://doi.org/10.1016/j.actamat.2016.08.081.

[12] W. Li, P. Liu, and P. K. Liaw, "Microstructures and properties of high-entropy alloy films and coatings: a review," *Materials Research Letters,* vol. 6, no. 4, pp. 199-229, 2018, doi: 10.1080/21663831.2018.1434248.

[13] R. Razuan, N. A. Jani, M. K. Harun, and M. K. Talari, "Microstructure and Hardness Properties Investigation of Ti and Nb Added FeNiAlCuCrTi _x Nb _y High Entropy Alloys," *Transactions of the Indian Institute of Metals,* vol. 66, no. 4, pp. 309-312, Aug 2013, doi: 10.1007/s12666-013-0265-7.

[14] X. Zhang, N. N. Zhang, B. W. Xing, and S. Yin, "An Assessment of the High-Temperature Oxidation Resistance of Selected Thermal Sprayed High Entropy Alloy Coatings," *Journal of Thermal Spray Technology,* vol. 31, no. 4, pp. 1386-1403, Apr 2022, doi: 10.1007/s11666-022-01352-w.

[15] Q. Y. Li, T. F. Ma, Y. L. Jin, X. H. Wang, D. Dong, and D. D. Zhu, "Effect of Sn and Mo on Microstructure and Electrochemical Property of TiZrTaNb High Entropy Alloys," *Crystals,* vol. 11, no. 12, Dec 2021, Art no. 1527, doi: 10.3390/cryst11121527.

[16] E. Lewin, "Multi-component and high-entropy nitride coatings-A promising field in need of a novel approach," *Journal of Applied Physics,* vol. 127, no. 16, Apr 2020, doi: 10.1063/1.5144154.

[17] X. Fu, C. A. Schuh, and E. A. Olivetti, "Materials selection considerations for high entropy alloys," *Scripta Materialia,* vol. 138, pp. 145-150, 2017/09/01/ 2017, doi: https://doi.org/10.1016/j.scriptamat.2017.03.014.

[18] A. Erdogan, S. E. Sunbul, K. Icin, and K. M. Doleker, "Microstructure, wear and oxidation behavior of AlCrFeNiX (X = Cu, Si, Co) high entropy alloys produced by powder metallurgy," *Vacuum,* vol. 187, p. 110143, 2021/05/01/ 2021, doi: https://doi.org/10.1016/j.vacuum.2021.110143.

[19] H. Zhao *et al.*, "Cathodic arc deposition of high entropy alloy thin films with controllable microstructure," *Surfaces and Interfaces,* vol. 37, Apr 2023, Art no. 102692, doi: 10.1016/j.surfin.2023.102692.

[20] A. Anders, "Cathodic Arcs: From Fractal Spots To Energetic Condensation," in *Cathodic Arcs: From Fractal Spots to Energetic Condensation*, vol. 50, (Springer Series on Atomic Optical and Plasma Physics, 2008, pp. 1-540.

[21] Y. F. Ye, Q. Wang, J. Lu, C. T. Liu, and Y. Yang, "High-entropy alloy: challenges and prospects," *Materials Today,* vol. 19, no. 6, pp. 349-362, Jul-Aug 2016, doi: 10.1016/j.mattod.2015.11.026.

[22] K. Yalamanchili *et al.*, "Exploring the high entropy alloy concept in (AlTiVNbCr)N," *Thin Solid Films,* vol. 636, pp. 346-352, Aug 2017, doi: 10.1016/j.tsf.2017.06.029.

[23] A. D. Pogrebnjak, A. A. Bagdasaryan, I. V. Yakushchenko, and V. M. Beresnev, "The structure and properties of high-entropy alloys and nitride coatings based on them," *Russian Chemical Reviews,* vol. 83, no. 11, pp. 1027-1061, 2014, doi: 10.1070/rcr4407.

[24] Y. Zhang *et al.*, "Microstructures and properties of high-entropy alloys," *Progress in Materials Science,* vol. 61, pp. 1-93, 2014/04/01/ 2014, doi: https://doi.org/10.1016/j.pmatsci.2013.10.001.

[25] J. Dabrowa, W. Kucza, G. Cieslak, T. Kulik, M. Danielewski, and J. W. Yeh, "Interdiffusion in the FCC-structured Al-Co-Cr-Fe-Ni high entropy alloys: Experimental studies and numerical simulations," *Journal of Alloys and Compounds,* vol. 674, pp. 455-462, Jul 2016, doi: 10.1016/j.jallcom.2016.03.046.

[26] Y. F. Kao, T. J. Chen, S. K. Chen, and J. W. Yeh, "Microstructure and mechanical property of as-cast, -homogenized, and -deformed AlxCoCrFeNi (0 <= x <= 2) high-entropy alloys," *Journal of Alloys and Compounds,* vol. 488, no. 1, pp. 57-64, Nov 2009, doi: 10.1016/j.jallcom.2009.08.090.

[27] Q. F. He and Y. Yang, "On Lattice Distortion in High Entropy Alloys," *Frontiers in Materials,* vol. 5, Jul 2018, Art no. 42, doi: 10.3389/fmats.2018.00042.

[28] N. A. Khan *et al.*, "High entropy alloy thin films of AlCoCrCu0.5FeNi with controlled microstructure," *Applied Surface Science,* vol. 495, Nov 2019, Art no. 143560, doi: 10.1016/j.apsusc.2019.143560.

[29] H. Zhao *et al.*, "High entropy alloy thin films on SS304 substrates: Evolution of microstructure and interface modulated by energetic condensation in nanoscale," *Materials & Design,* vol. 230, p. 111981, 2023/06/01/ 2023, doi: https://doi.org/10.1016/j.matdes.2023.111981.

[30] Z. F. Wu *et al.*, "Microstructure characterization of AlxCo1Cr1Cu1Fe1Ni1 (x=0 and 2.5) high-entropy alloy films," *Journal of Alloys and Compounds,* vol. 609, pp. 137-142, 2014/10/05/ 2014, doi: https://doi.org/10.1016/j.jallcom.2014.04.094.

[31] V. Dolique, A. L. Thomann, P. Brault, Y. Tessier, and P. Gillon, "Thermal stability of AlCoCrCuFeNi high entropy alloy thin films studied by in-situ XRD analysis," *Surface and Coatings Technology,* vol. 204, no. 12, pp. 1989-1992, 2010/03/15/ 2010, doi: https://doi.org/10.1016/j.surfcoat.2009.12.006.

[32] X. Sun, X. Cheng, H. Cai, S. Ma, Z. Xu, and T. Ali, "Microstructure, mechanical and physical properties of FeCoNiAlMnW high-entropy films deposited by magnetron sputtering," *Applied Surface Science,* vol. 507, p. 145131, 12/01 2019, doi: 10.1016/j.apsusc.2019.145131.

[33] H.-W. Chang, P.-K. Huang, A. Davison, J.-W. Yeh, C.-H. Tsau, and C.-C. Yang, "Nitride films deposited

from an equimolar Al–Cr–Mo–Si–Ti alloy target by reactive direct current magnetron sputtering," *Thin Solid Films,* vol. 516, pp. 6402-6408, 07/01 2008, doi: 10.1016/j.tsf.2008.01.019.

[34] N. A. Khan *et al.*, "High entropy alloy thin films of AlCoCrCu0.5FeNi with controlled microstructure," *Applied Surface Science,* vol. 495, p. 143560, 2019/11/30/ 2019, doi: https://doi.org/10.1016/j.apsusc.2019.143560.

[35] G. Jin *et al.*, "High temperature wear performance of laser-cladded FeNiCoAlCu high-entropy alloy coating," *Applied Surface Science,* vol. 445, pp. 113-122, Jul 2018, doi: 10.1016/j.apsusc.2018.03.135.

[36] H. Zhang, Y. Pan, and Y. Z. He, "LASER CLADDING FeCoNiCrAl₂Si HIGH-ENTROPY ALLOY COATING," *Acta Metallurgica Sinica,* vol. 47, no. 8, pp. 1075-1079, Aug 2011, doi: 10.3724/sp.J.1037.2011.00043.

[37] B. Han *et al.*, "Hardness enhancement mechanism of AlxCoCrFeNiSi high-entropy alloy coatings prepared by laser cladding," *Intermetallics,* vol. 158, Jul 2023, Art no. 107909, doi: 10.1016/j.intermet.2023.107909.

[38] Z. Zheng *et al.*, "Enhanced strength of AlCoCrCu0.5FeNi high entropy alloy thin films reinforced by multi-phase hardening and nanotwins," *Materials Science and Engineering: A,* vol. 879, p. 145252, 2023/07/10/ 2023, doi: https://doi.org/10.1016/j.msea.2023.145252.

[39] R. Chen *et al.*, "Effects of nitriding on the microstructure and properties of VAlTiCrMo high-entropy alloy coatings by sputtering technique," *Journal of Alloys and Compounds,* vol. 827, Jun 2020, Art no. 153836, doi: 10.1016/j.jallcom.2020.153836.

[40] A. D. Pogrebnjak *et al.*, "Microstructure, physical and chemical properties of nanostructured (Ti-Hf-Zr-V-Nb)N coatings under different deposition conditions," *Materials Chemistry and Physics,* vol. 147, no. 3, pp. 1079-1091, Oct 2014, doi: 10.1016/j.matchemphys.2014.06.062.

[41] M. Enomoto, "The N-Ti-V system (nitrogen-titanium-vanadium)," *Journal of Phase Equilibria,* vol. 17, no. 3, pp. 248-252, 1996/06/01 1996, doi: 10.1007/BF02648494.

[42] J. Häglund, A. Fernández Guillermet, G. Grimvall, and M. Körling, "Theory of bonding in transition-metal carbides and nitrides," *Physical Review B,* vol. 48, no. 16, pp. 11685-11691, 10/15/ 1993, doi: 10.1103/PhysRevB.48.11685.

[43] F. Tessier *et al.*, "Energetics of binary iron nitrides," *Solid State Sciences,* vol. 2, no. 4, pp. 457-462, 2000/06/04/ 2000, doi: https://doi.org/10.1016/S1293-2558(00)00151-5.

[44] E. A. Shenyavskaya and V. S. Yungman, "NIST-JANAF thermochemical tables. III. Diatomic hydrogen halide gases," *Journal of Physical and Chemical Reference Data,* vol. 33, no. 3, pp. 923-957, Sep 2004, doi: 10.1063/1.1638781.

[45] J. Patscheider, "Nanocomposite Hard Coatings for Wear Protection," *MRS Bulletin,* vol. 28, no. 3, pp. 180-183, 2003/03/01 2003, doi: 10.1557/mrs2003.59.

[46] I. A. Abrikosov *et al.*, "Phase Stability and Elasticity of TiAlN," *Materials*, vol. 4, no. 9, pp. 1599-1618doi: 10.3390/ma4091599.

[47] U. Jansson and E. Lewin, "Sputter deposition of transition-metal carbide films — A critical review from a chemical perspective," *Thin Solid Films,* vol. 536, pp. 1-24, 2013/06/01/ 2013, doi: https://doi.org/10.1016/j.tsf.2013.02.019.

[48] T. K. Chen, T. T. Shun, J. W. Yeh, and M. S. Wong, "Nanostructured nitride films of multi-element high-entropy alloys by reactive DC sputtering," *Surface and Coatings Technology,* vol. 188-189, pp. 193-200, 2004/11/01/ 2004, doi: https://doi.org/10.1016/j.surfcoat.2004.08.023.

[49] B. Ren, S. J. Lv, R. F. Zhao, Z. X. Liu, and S. K. Guan, "Effect of sputtering parameters on (AlCrMnMoNiZr)N films," *Surface Engineering,* vol. 30, no. 2, pp. 152-158, 2014/02/01 2014, doi: 10.1179/1743294413Y.0000000226.

[50] B. Ren, Z. Shen, and Z. Liu, "Structure and mechanical properties of multi-element (AlCrMnMoNiZr)Nx coatings by reactive magnetron sputtering," *Journal of Alloys and Compounds,* vol. 560, pp. 171-176, 05/01 2013, doi: 10.1016/j.jallcom.2013.01.148.

[51] L. Liu, J. B. Zhu, C. Hou, J. C. Li, and Q. Jiang, "Dense and smooth amorphous films of multicomponent FeCoNiCuVZrAl high-entropy alloy deposited by direct current magnetron sputtering," *Materials & Design (1980-2015),* vol. 46, pp. 675-679, 2013/04/01/ 2013, doi: https://doi.org/10.1016/j.matdes.2012.11.001.

[52] Y. Zhao *et al.*, "Super-hard and anti-corrosion (AlCrMoSiTi)Nx high entropy nitride coatings by multi-arc cathodic vacuum magnetic filtration deposition," *Vacuum,* vol. 195, p. 110685, 2022/01/01/ 2022, doi: https://doi.org/10.1016/j.vacuum.2021.110685.

[53] Y. M. Zhao *et al.*, "Influence of N concentration on structure and properties of (AlCrMoTiV)Nx films by co-filter cathodic vacuum arc deposition," *Surface & Coatings Technology,* vol. 459, Apr 2023, Art no. 129366, doi: 10.1016/j.surfcoat.2023.129366.

[54] Q. Wan *et al.*, "Microstructure and mechanical properties of FeCoCrNiAl0.1N high entropy alloy nitride coatings synthesized by cathodic arc ion plating using alloy target," *Surface & Coatings Technology,* vol. 457, Mar 2023, Art no. 129305, doi: 10.1016/j.surfcoat.2023.129305.

[55] A. D. Pogrebnjak, V. M. Beresnev, K. V. Smyrnova, Y. O. Kravchenko, P. V. Zukowski, and G. G. Bondarenko, "The influence of nitrogen pressure on the fabrication of the two-phase superhard nanocomposite (TiZrNbAlYCr)N coatings," *Materials Letters,* vol. 211, pp. 316-318, 2018/01/15/ 2018, doi: https://doi.org/10.1016/j.matlet.2017.09.121.

[56] C. Cushman, S. Chatterjee, G. Major, N. Smith, A. Roberts, and M. Linford, "Trends in Advanced XPS Instrumentation. 1. Overview of the Technique, Automation, High Sensitivity, Imaging, Snapshot Spectroscopy, Gas Cluster Ion Beams, and Multiple Analytical Techniques on the Instrument," *Vacuum Technology & Coating,* 11/01 2016.

[57] C.-C. Tung, J.-W. Yeh, T.-t. Shun, P.-H. Lee, Y.-S. Huang, and H.-C. Chen, "On the elemental effect of AlCoCrCuFeNi high-entropy alloy system," *Materials Letters,* vol. 61, pp. 1-5, 01/31 2007, doi: 10.1016/j.matlet.2006.03.140.

[58] F. B. Dietrich Lepski, "Laser Cladding," in *The Theory of Laser Materials Processing*, 1 ed. SpringerLink: Springer Dordrecht, 2009, ch. 8, pp. 235-279.

[59] Z. Liu, "Laser Applied Coatings," *Shreir's Corrosion,* vol. 4, pp. 2622-2635, 12/31 2010, doi: 10.1016/B978-044452787-5.00141-4.

[60] J. Chen, Y. Zhou, C. Shi, and D. Mao, "Microscopic Analysis and Electrochemical Behavior of Fe-Based Coating Produced by Laser Cladding," *Metals*, vol. 7, no. 10*,* doi: 10.3390/met7100435.

[61] T. M. Yue, H. Xie, X. Lin, H. O. Yang, and G. H. Meng, "Solidification behaviour in laser cladding of AlCoCrCuFeNi high-entropy alloy on magnesium substrates," *Journal of Alloys and Compounds,* vol. 587, pp. 588-593, 2014/02/25/ 2014, doi: https://doi.org/10.1016/j.jallcom.2013.10.254.

[62] H. Zhang, Y.-Z. He, Y. Pan, and S. Guo, "Thermally stable laser cladded CoCrCuFeNi high-entropy alloy coating with low stacking fault energy," *Journal of Alloys and Compounds,* vol. 600, pp. 210–214, 07/01 2014, doi: 10.1016/j.jallcom.2014.02.121.

[63] X. H. Yan, J. S. Li, W. R. Zhang, and Y. Zhang, "A brief review of high-entropy films," *Materials Chemistry and Physics,* vol. 210, pp. 12-19, 2018/05/01/ 2018, doi: https://doi.org/10.1016/j.matchemphys.2017.07.078.

[64] K.-H. Cheng, C.-H. Lai, S.-J. Lin, and J.-W. Yeh, "Structural and mechanical properties of multi-element (AlCrMoTaTiZr)Nx coatings by reactive magnetron sputtering," *Thin Solid Films,* vol. 519, no. 10, pp. 3185-3190, 2011/03/01/ 2011, doi: https://doi.org/10.1016/j.tsf.2010.11.034.

[65] H. Zhao *et al.*, "The fabrication and growth mechanism of AlCrFeCoNiCu0.5 HEA thin films by substrate-

biased cathodic arc deposition," *Scientific Reports,* vol. 13, no. 1, Jan 2023, Art no. 198, doi: 10.1038/s41598-022-26232-9.

[66] J. Mittra *et al.*, "Role of Substrate Temperature in the Pulsed Laser Deposition of Zirconium Oxide Thin Film," *Materials Science Forum,* vol. 710, pp. 757-761, 01/01 2012, doi: 10.4028/www.scientific.net/MSF.710.757.

[67] T.-W. Lu *et al.*, "Microstructures and mechanical properties of CoCrFeNiAl0.3 high-entropy alloy thin films by pulsed laser deposition," *Applied Surface Science,* vol. 494, pp. 72-79, 2019/11/15/ 2019, doi: https://doi.org/10.1016/j.apsusc.2019.07.186.

[68] *Handbook of Deposition Technologies for Films and Coatings: Science, Applications and Technology, 3rd Edition* (Handbook of Deposition Technologies for Films and Coatings: Science, Applications and Technology, 3rd Edition). 2010, pp. 1-912.

[69] Y. S. Choong, B. K. Tay, S. P. Lau, X. Shi, and Y. H. Cheng, "High deposition rate of aluminum oxide film by off-plane double bend filtered cathodic vacuum arc technique," *Thin Solid Films,* vol. 386, no. 1, pp. 1-5, May 2001, doi: 10.1016/s0040-6090(00)01878-2.

[70] I. G. Brown, "Cathodic arc deposition of films," *Annual Review of Materials Science,* vol. 28, pp. 243-269, 1998, doi: 10.1146/annurev.matsci.28.1.243.

[71] A. D. Pogrebnjak *et al.*, "Microstructure, physical and chemical properties of nanostructured (Ti–Hf–Zr–V–Nb)N coatings under different deposition conditions," *Materials Chemistry and Physics,* vol. 147, no. 3, pp. 1079-1091, 2014/10/15/ 2014, doi: https://doi.org/10.1016/j.matchemphys.2014.06.062.

[72] S. N. Chen *et al.*, "Preparation and regulation of AlCrNiTiSi high entropy alloy coating by a multi-arc magnetic filter cathode vacuum arc system," *Surfaces and Interfaces,* vol. 26, p. 101400, 2021/10/01/ 2021, doi: https://doi.org/10.1016/j.surfin.2021.101400.

[73] Y. Y. Chang and J. W. Huang, "Nanostructured AlTiSiN/CrVN/ZrN coatings synthesized by cathodic arc deposition- mechanical properties and cutting performance," *Surface & Coatings Technology,* vol. 442, Jul 2022, Art no. 128424, doi: 10.1016/j.surfcoat.2022.128424.

[74] D. M. Sanders and A. Anders, "Review of cathodic arc deposition technology at the start of the new millennium," *Surface & Coatings Technology,* vol. 133, pp. 78-90, Nov 2000, doi: 10.1016/s0257-8972(00)00879-3.

[75] I. G. Brown, "CATHODIC ARC DEPOSITION OF FILMS," *Annual Review of Materials Science,* vol. 28, no. 1, pp. 243-269, 1998, doi: 10.1146/annurev.matsci.28.1.243.

[76] D. M. Mattox and D. M. Mattox, *Atomistic Film Growth and Some Growth-Related Film Properties* (Handbook of Physical Vapor Deposition). 2010, pp. 333-398.

[77] M. M. B. Marcela and A. André, "Designing advanced filters for macroparticle removal from cathodic arc plasmas," *Plasma Sources Science and Technology,* vol. 8, no. 3, p. 488, 1999/08/01 1999, doi: 10.1088/0963-0252/8/3/319.

[78] A. Ul-Hamid, *A Beginners' Guide to Scanning Electron Microscopy*. SpringerLink, 2018.

[79] D. E. N. Joseph I. Goldstein , Patrick Echlin , David C. Joy , Charles E. Lyman , Eric Lifshin , Linda Sawyer , Joseph R. Michael, *Scanning Electron Microscopy and X-Ray Microanalysis*, Third ed. SpringerLink: Springer New York, NY, 2003.

[80] U. o. Cambridge. "Engineering AtomsAtoms, The Scanning Electron Microscope (SEM)." https://www.eng-atoms.msm.cam.ac.uk/RoyalSocDemos/SEM (accessed 2023).

[81] N. Instruments. "Scanning Electron Microscopy." https://www.nanoscience.com/techniques/scanning-electron-microscopy/ (accessed 2023).

[82] L. D. Whittig and W. R. Allardice, "X-Ray Diffraction Techniques," in *Methods of Soil Analysis*, 1986, pp.

331-362.
[83] J. B. Brady, R. M. Newton, and S. J. Boardman, "New Uses for Powder X-Ray Diffraction Experiments in the Undergraduate Curriculum," *Journal of Geological Education,* vol. 43, no. 5, pp. 466-470, 1995/11/01 1995, doi: 10.5408/0022-1368-43.5.466.
[84] J. B. Brady and S. J. Boardman, "Introducing Mineralogy Students to X-Ray Diffraction through Optical Diffraction Experiments using Lasers," *Journal of Geological Education,* vol. 43, no. 5, pp. 471-476, 1995/11/01 1995, doi: 10.5408/0022-1368-43.5.471.
[85] G. Zeng, Y. Duan, F. Besenbacher, and M. Dong, "Nanomechanics of Amyloid Materials Studied by Atomic Force Microscopy," 2012.
[86] D. A. Lucca, K. Herrmann, and M. J. Klopfstein, "Nanoindentation: Measuring methods and applications," *Cirp Annals-Manufacturing Technology,* vol. 59, no. 2, pp. 803-819, 2010, doi: 10.1016/j.cirp.2010.05.009.
[87] D. A. Lucca, K. Herrmann, and M. J. Klopfstein, "Nanoindentation: Measuring methods and applications," *CIRP Annals,* vol. 59, no. 2, pp. 803-819, 2010/01/01/ 2010, doi: https://doi.org/10.1016/j.cirp.2010.05.009.
[88] I. Utke, J. Michler, R. Winkler, and H. Plank, "Mechanical Properties of 3D Nanostructures Obtained by Focused Electron/Ion Beam-Induced Deposition: A Review," *Micromachines*, vol. 11, no. 4, doi: 10.3390/mi11040397.
[89] K. W. Lee *et al.*, "An international round-robin experiment to evaluate the consistency of nanoindentation hardness measurements of thin films," *Surface & Coatings Technology,* vol. 168, no. 1, pp. 57-61, May 2003, doi: 10.1016/s0257-8972(02)00889-7.
[90] Y. M. Zhao *et al.*, "Super-hard and anti-corrosion (AlCrMoSiTi)N-x high entropy nitride coatings by multi-arc cathodic vacuum magnetic filtration deposition," *Vacuum,* vol. 195, Jan 2022, Art no. 110685, doi: 10.1016/j.vacuum.2021.110685.
[91] M. Ali, E. Hamzah, T. Abbas, M. Toff, and I. A. Qazi, "MACRODROPLET REDUCTION AND GROWTH MECHANISMS IN CATHODIC ARC PHYSICAL VAPOR DEPOSITION OF TiN FILMS," *Surface Review and Letters,* vol. 15, no. 5, pp. 653-659, Oct 2008, doi: 10.1142/s0218625x08011810.
[92] M. Golizadeh, F. M. Martin, S. Kolozsvári, A. Anders, and R. Franz, "Cathode spot behavior in nitrogen and oxygen gaseous atmospheres and concomitant cathode surface modifications," *Surface & Coatings Technology,* vol. 421, Sep 2021, Art no. 127441, doi: 10.1016/j.surfcoat.2021.127441.
[93] F. Richter, G. Krannich, M. Kuhn, S. Peter, and C. Spaeth, "Cathodic arc evaporation - A versatile tool for thin film deposition," in *Trends and New Applications of Thin Films*, vol. 287-2, H. Hoffmann Ed., (Materials Science Forum, 1998, pp. 193-197.
[94] H. Zhao, "Effect of nitrogen pressure on the fabrication of AlCrFeCoNiCu0.5 high entropy nitride thin films via cathodic arc deposition," *Journal of Vacuum Science & Technology A,* vol. 41, 10/31 2023, doi: 10.1116/6.0003064.
[95] M. M. M. Bilek, P. J. Martin, and D. R. McKenzie, "Influence of gas pressure and cathode composition on ion energy distributions in filtered cathodic vacuum arcs," *Journal of Applied Physics,* vol. 83, no. 6, pp. 2965-2970, 1998, doi: 10.1063/1.367052.
[96] Y. S. Li *et al.*, "CVD deposition of nanocrystalline diamond coatings on implant alloy materials with CrN/Al interlayer," *Surface and Coatings Technology,* vol. 353, pp. 364-369, 2018/11/15/ 2018, doi: https://doi.org/10.1016/j.surfcoat.2018.07.108.
[97] J. P. Manaud, A. Poulon, S. Gomez, and Y. L. Petitcorps, "A comparative study of CrN, ZrN, NbN and TaN layers as cobalt diffusion barriers for CVD diamond deposition on WC–Co tools," *Surface and Coatings Technology,* vol. 202, no. 2, pp. 222-231, 2007/11/25/ 2007, doi: https://doi.org/10.1016/j.surfcoat.2007.05.024.
[98] F. Sirotti, M. De Santis, and G. Rossi, "Synchrotron-radiation photoemission and x-ray absorption of Fe

silicides," *Physical Review B,* vol. 48, no. 11, pp. 8299-8306, 09/15/ 1993, doi: 10.1103/PhysRevB.48.8299.

[99] I. Olefjord, H. J. Mathieu, and P. Marcus, "INTERCOMPARISON OF SURFACE-ANALYSIS OF THIN ALUMINUM-OXIDE FILMS," *Surface and Interface Analysis,* vol. 15, no. 11, pp. 681-692, Nov 1990, doi: 10.1002/sia.740151108.

[100] J. Malcolm W. Chase, *NIST-JANAF thermochemical tables*, 4 ed. The American Chemical Society, and The American Institute of Physics for the National Institute of Standards and Technology, 1998.

[101] S. H. Elder, F. J. Disalvo, L. Topor, and A. Navrotsky, "THERMODYNAMICS OF TERNARY NITRIDE FORMATION BY AMMONOLYSIS - APPLICATION TO LIMON2, NA3WN3, AND NA3WO3N," *Chemistry of Materials,* vol. 5, no. 10, pp. 1545-1553, Oct 1993, doi: 10.1021/cm00034a027.

[102] R. Learner, *HANDBOOK OF CHEMISTRY AND PHYSICS* (Proceedings of the Physical Society of London, no. 551P). 1965, pp. 668-&.

[103] H. E. Swanson, *Standard X-ray diffraction powder patterns*. US Department of Commerce, National Bureau of Standards, 1955.

[104] S. Holgersson, "Röntgenorgraphische Strukturuntersuchungen von einigen Metallegierungen (Die Reihen AuAg und NiCu)," *Annalen der Physik,* vol. 384, no. 1, pp. 35-54, 1926, doi: 10.1002/andp.19263840103.

[105] I. K. Suh, H. Ohta, and Y. Waseda, "HIGH-TEMPERATURE THERMAL-EXPANSION OF 6 METALLIC ELEMENTS MEASURED BY DILATATION METHOD AND X-RAY-DIFFRACTION," *Journal of Materials Science,* vol. 23, no. 2, pp. 757-760, Feb 1988, doi: 10.1007/bf01174717.

[106] L. Marick, "Variation of resistance and structure of colbalt with temperature and a discussion of its photoelectric emission," *Physical Review,* vol. 49, no. 11, pp. 0831-0837, Jun 1936, doi: 10.1103/PhysRev.49.831.

[107] H. W. Chang, P. K. Huang, A. Davison, J. W. Yeh, C. H. Tsau, and C. C. Yang, "Nitride films deposited from an equimolar Al-Cr-Mo-Si-Ti alloy target by reactive direct current magnetron sputtering," *Thin Solid Films,* vol. 516, no. 18, pp. 6402-6408, Jul 2008, doi: 10.1016/j.tsf.2008.01.019.

[108] H. T. Hsueh, W. J. Shen, M. H. Tsai, and J. W. Yeh, "Effect of nitrogen content and substrate bias on mechanical and corrosion properties of high-entropy films (AlCrSiTiZr)(100-x)N-x," *Surface & Coatings Technology,* vol. 206, no. 19-20, pp. 4106-4112, May 2012, doi: 10.1016/j.surfcoat.2012.03.096.

[109] T. K. Chen, T. T. Shun, J. W. Yeh, and M. S. Wong, "Nanostructured nitride films of multi-element high-entropy alloys by reactive DC sputtering," *Surface & Coatings Technology,* vol. 188, pp. 193-200, Nov-Dec 2004, doi: 10.1016/j.surfcoat.2004.08.023.

[110] J. William D. Callister, *Fundamentals of Materials Science and Engineering: An Integrated Approach*, 5 ed. Enhanced eText, (Wiley, Hoboken, NJ, 2018.

[111]Q. Wan *et al.*, "Microstructure and mechanical properties of FeCoCrNiAl0.1N high entropy alloy nitride coatings synthesized by cathodic arc ion plating using alloy target," *Surface and Coatings Technology,* vol. 457, p. 129305, 2023/03/25/ 2023, doi: https://doi.org/10.1016/j.surfcoat.2023.129305.

[112] K. von Fieandt, L. Riekehr, B. Osinger, S. Fritze, and E. Lewin, "Influence of N content on structure and mechanical properties of multi-component Al-Cr-Nb-Y-Zr based thin films by reactive magnetron sputtering," *Surface and Coatings Technology,* vol. 389, p. 125614, 2020/05/15/ 2020, doi: https://doi.org/10.1016/j.surfcoat.2020.125614.

[113] K. Bordo and H.-G. Rubahn, "Effect of Deposition Rate on Structure and Surface Morphology of Thin Evaporated Al Films on Dielectrics and Semiconductors," *Materials Science,* vol. 18, 12/17 2012, doi: 10.5755/j01.ms.18.4.3088.

[114] B. Astinchap, "Fractal and statistical characterization of Ti thin films deposited by RF-magnetron sputtering: The effects of deposition time," *Optik,* vol. 178, pp. 231-242, 2019, doi: 10.1016/j.ijleo.2018.10.050.

[115] D. Williams and C. Carter, *Transmission Electron Microscopy: A Textbook for Materials Science*. 2009.

[116] N. Marturi, "Vision and visual servoing for nanomanipulation and nanocharacterization in scanning electron microscope," 11/19 2013.

[117] X.-M. Li, D. Reinhoudt, and M. Crego-Calama, "What Do We Need for Superhydrophobic Surface? A Review on the Recent Progress in the Preparation of Superhydrophobic Surfaces," *Chemical Society reviews,* vol. 36, pp. 1350-68, 09/01 2007, doi: 10.1039/b602486f.

[118] S.-J. Park and M.-K. Seo, "Chapter 3 - Solid-Liquid Interface," in *Interface Science and Technology*, vol. 18, S.-J. Park and M.-K. Seo Eds.: Elsevier, 2011, pp. 147-252.

[119] S. Ummartyotin, J. Juntaro, C. Wu, M. Sain, and H. Manuspiya, "Deposition of PEDOT: PSS Nanoparticles as a Conductive Microlayer Anode in OLEDs Device by Desktop Inkjet Printer," *Journal of Nanomaterials,* vol. 2011, p. 606714, 2011/05/26 2011, doi: 10.1155/2011/606714.

[120] J.-J. Wang, S.-Y. Chang, and F.-Y. Ouyang, "Effect of substrate bias on the microstructure and properties of (AlCrSiNbZr)Nx high entropy nitride thin film," *Surface and Coatings Technology,* vol. 393, p. 125796, 2020/07/15/ 2020, doi: https://doi.org/10.1016/j.surfcoat.2020.125796.

[121] M. Kuczyk *et al.*, "Microstructure and mechanical properties of high entropy alloy nitride coatings deposited via direct current cathodic vacuum arc deposition," *Surface & Coatings Technology,* vol. 448, Oct 2022, Art no. 128916, doi: 10.1016/j.surfcoat.2022.128916.

[122] J. Khakzadian, S. H. Hosseini, and K. Z. Madar, "The effect of the substrate temperature on the microstructure properties of the NiCrAI coating in cathodic arc deposition," *Surface & Coatings Technology,* vol. 337, pp. 342-348, Mar 2018, doi: 10.1016/j.surfcoat.2018.01.001.

[123] Y.-C. Lin *et al.*, "Improving the hardness of high entropy nitride (Cr0.35Al0.25Nb0.12Si0.08V0.20)N coatings via tuning substrate temperature and bias for anti-wear applications," *Surface and Coatings Technology,* vol. 403, p. 126417, 2020/12/15/ 2020, doi: https://doi.org/10.1016/j.surfcoat.2020.126417.